

THE DISTRIBUTION OF GLOBULAR CLUSTERS IN M87

by Carl Johann Grillmair
B.Sc., University of Calgary, 1983

A THESIS SUBMITTED IN PARTIAL FULFILLMENT

OF THE REQUIREMENTS FOR THE DEGREE OF

MASTER OF SCIENCE


in the Department


of

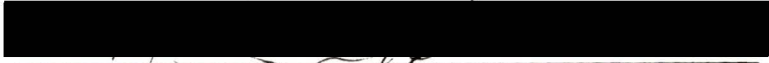
Physics

We accept this thesis as conforming
to the required standard


Dr. C. J. Pritchett


Dr. F. D. A. Hartwick


Dr. C. D. Scarfe


Dr. V. J. Tunnicliffe


Dr. D. Crampton

© Carl Johann Grillmair, 1985

University of Victoria

August 1985

*All rights reserved. This thesis may not be reproduced
in whole or in part, by mimeograph or other means,
without the permission of the author.*

ACCEPTED

ACADEMY OF GRADUATE STUDIES



DATE Feb 28, 86 DEAN

QB853
G75

RECEIVED
LIBRARY OF THE
UNIVERSITY OF MICHIGAN
ANN ARBOR MI 48106-1000

Supervisor: Dr. Christopher J. Pritchett

ABSTRACT

Deep CCD observations of a field one arcminute east of the core of M87 are analyzed to determine the luminosity and spatial distribution of M87's globular cluster system. Using the crowded-field photometry package DAOPHOT, cluster positions and magnitudes are determined to a limiting magnitude of $B_{lim} \sim 25.5$. Completeness of the sample as a function of magnitude is determined by analyzing, in an identical manner, images containing the original data as well as a specified number of artificial stellar profiles of known magnitudes. Contamination of the sample by background galaxies and foreground stars is estimated by similarly analyzing CCD observations of a field somewhat removed from M87.

Correcting the observations for completeness and background-foreground contamination, we have determined a luminosity function for globular clusters in the region 50 to 160 arcseconds from the apparent center of M87. This luminosity function does not follow the functional form used to represent the luminosity distribution of globular clusters in the Local Group. On the other hand, a direct

comparison of M87 globular clusters with those in M31 and the Galaxy does not rule out a "universal" form for the luminosity function.

In an effort to detect a radial trend in the luminosity function, completeness of the sample is also determined as a function of projected galactocentric radius. Over the radial region 20 to 160 arcseconds, we find no conclusive evidence for such a trend. In addition, a comparison of the present sample with observations of previous investigators indicates that there is no strong trend in the luminosity function within the region 0.3 to 9 arcminutes.

On the other hand, we find the radial surface density profile of globular clusters to be significantly shallower than that determined by previous investigators for larger radii. Assuming an M87 mass profile as suggested by recent X-ray observations, we demonstrate that the overall shape of the surface density profile can be well-fitted by simple models invoking highly radial anisotropies in the globular cluster velocity dispersion. Combining this with the lack of a significant trend in the luminosity function, we conclude that evolutionary processes such as dynamical friction and globular cluster stripping have probably not been very effective in the region under consideration. We suggest that the observed distribution, along with the anomalously large number (~ 20000) of globular clusters associated with M87, is likely to be the product of conditions prevailing at the time of M87's initial collapse.

Examiners:

[Redacted]

Dr. C. J. Pritchett

[Redacted]

Dr. F. D. A. Hartwick

[Redacted]

Dr. C. D. Scarfe

[Redacted]

Dr. V. J. Tunnicliffe

[Redacted]

Dr. D. Crampton

TABLE OF CONTENTS

	page
ABSTRACT	ii
TABLE OF CONTENTS	v
LIST OF TABLES	vii
LIST OF FIGURES	viii
ACKNOWLEDGEMENTS	x
DEDICATION	xi
CHAPTER 1 INTRODUCTION	1
CHAPTER 2 OBSERVATIONS AND DATA REDUCTION	6
2.1 Preliminary Reductions	9
2.2 Background Subtraction	12
2.3 The Photometry Software Package	14
2.4 Object Detection	17
2.5 Aperture Photometry	20
2.6 Determination of the Point-Spread Function	21
2.7 Recovery of Hidden Objects	22
2.8 Multiple Profile Fitting	24
2.9 Photometric Calibration	28
CHAPTER 3 THE GLOBULAR CLUSTER LUMINOSITY FUNCTION	62
3.1 Completeness Corrections	62
3.2 Background Corrections	67
3.3 The Luminosity Function	72
CHAPTER 4 THE RADIAL DISTRIBUTION OF GLOBULAR CLUSTERS	79
4.1 Radial Completeness Corrections	79
4.2 Spurious Images	85
4.3 Radial Variations in the Luminosity Function	89
4.4 The Radial Surface Density Profile	96
4.5 The Total Number of Globular Clusters in M87	106
4.6 Non-radial Distribution of Surface Density	108

TABLE OF CONTENTS - continued

CHAPTER 5	DISCUSSION	113
5.1	A Simple Analytic Density Profile	113
5.2	The Distribution of Mass in M87	115
5.3	Isotropic, Single-Component Model	122
5.4	Isotropic, Two-Component Model	126
5.5	The Effect of A Velocity Anisotropy	128
5.6	Depletion Through Dynamical Friction	137
5.7	Depletion Through Tidal Stripping	143
5.8	Tidal Accretion and Removal of Globular Clusters	146
5.9	Initial Conditions	150
CHAPTER 6	SUMMARY AND CONCLUSION	153
REFERENCES	160

LIST OF TABLES

Table	page
1. CFHT CCD Observations of M87	7
2. Objects Used to Calculate the Point-Spread Function	23
3. Distribution of Natural Groups For Objects in Table 4	26
4. DAOPHOT Object List	30
5. Objects Common to Present Sample and That of Strom et al. (1981)	58
6. Counts of Objects in M87 and Background Fields	73
7. Completeness as a Function of Radius and Magnitude	81
8. Differential Luminosity Functions for Five Radial Zones	90
9. Integrated Surface Densities for Various Limiting Magnitudes	97

LIST OF FIGURES

Figure	page
1. Reproduction of background-subtracted CCD image	15
2. Mean computed magnitude errors as a function of magnitude and projected galactocentric radius	57
3. Comparison of transformed B magnitudes computed using DAOPHOT with those determined by Strom et al. (1981).	61
4. Calculated completenesses as a function of magnitude.	66
5. Apparent luminosity function of objects found in the background field.	69
6. The globular cluster luminosity function for the region $50'' < r < 159''$	74
7. Completeness calculated as a function of magnitude and radius.	84
8. The luminosity function of noise-generated intensity enhancements.	87
9. Differential luminosity functions in five radial zones.	91
10. Normalized differential luminosity functions in five radial zones	92
11. The differential luminosity function of the present sample as a whole compared with those of Strom et al. (1981) for larger radii.	95
12. Integrated surface density profiles for various limiting magnitudes.	98
13. Surface density of M87 globular clusters to $r \sim 22$ arcminutes.	101
14. Surface density profile determined from the present sample compared with that of Strom et al. (1981)	105
15. A scaled representation of the M87 field under study.	109

LIST OF FIGURES - continued

Figure	page
16. The variation of surface density with position angle.	112
17. The mass profile of M87	118
18. Surface densities predicted by models assuming isotropic velocity dispersions.	123
19. Surface densities predicted by models assuming a radially-variable anisotropy in the velocity dispersion.	134
20. Lindblad diagram for the orbital evolution of a $10^6 M_{\odot}$ globular cluster for various initial orbital eccentricities.	140
21. The evolution of apocentric distance R_a for a globular cluster of $10^6 M_{\odot}$	142

ACKNOWLEDGEMENTS

I am grateful to Dr. Chris Pritchett for having suggested the topic of this study, and for having allocated a portion of his operating grant in support of its completion. Dr. Pritchett has provided invaluable guidance throughout this project, and his personal enthusiasm has been a constant source of inspiration and encouragement.

I would also like to thank the Director of the Dominion Astrophysical Observatory, Dr. Sidney van den Bergh, for his consent to my use of the data discussed herein, and for allowing me to use the computing facilities available at the DAO.

I am indebted to the members of my supervisory committee for all the time and efforts expended on my behalf. In addition, I would like to thank Tad Pryor and Polo Infante for many useful and stimulating discussions.

My parents I would like to thank for having always been supportive of my ideals and ambitions, and I am thankful to my little sister for her continual reassurances.

Most of all, I am grateful to my wife. Without her patience, understanding, and love, this work should never have progressed at all.

In Memory of Walter.

CHAPTER 1

INTRODUCTION

Any sufficiently long exposure of the giant elliptical galaxy M87 (NGC 4486) reveals that at magnitudes fainter than about $B = 20$, the nucleus of the galaxy is surrounded by an apparent concentration of starlike objects. Baum (1955) was the first to suggest that this large concentration of images represented the brightest members of a very extensive globular cluster population, and estimated that there were in fact "more than a thousand of them". Since the typical core radii of globulars in our own galaxy are of order 1 pc (Harris and Racine 1979), their apparent diameters if they were observed from a distance of 15 Mpc would be of order 0.05 arcseconds. This would make them completely unresolvable with ground-based telescopes and consequently stellar in appearance. The estimated total number of globular clusters belonging to M87 has been an ever-increasing quantity over the past 30 years (Sandage 1961; Racine 1968; Harris and Smith 1976), and currently stands at something of the order of 20000 (van den Bergh, Pritchet, and Grillmair 1985, henceforth Paper I).

This is by far the largest number of such objects to be found in any single galaxy, and it has been argued that this is due largely to

M87's apparent placement near the bottom of the Virgo cluster potential well (van den Bergh 1977). Though tidal stripping or outright cannibalism of smaller passing galaxies has been suggested as being responsible for the overabundance, van den Bergh (1983) has argued that the sheer magnitude of the overabundance makes this possibility unlikely. Furthermore, Muzzio (1985a) has calculated that encounters with passing galaxies would in fact lead to an overall depletion in the number of globular clusters over time, so that M87's cluster population should have been even larger at the time of formation. Harris and Petrie (1978), on the other hand, have suggested that if the number of globular clusters is assumed to be correlated with the mass of the parent galaxy, then the apparent abundance may not be anomalous at all if the mass-to-light ratio of M87 is as rather higher than normal (Arp and Bertola 1971). X-ray observations by Fabricant et al. (1980) and Stewart et al. (1984) suggest that, at least in the outer regions of M87, this may indeed be the case, though similar observations of other galaxies by Forman et al. (1985) seem to indicate that massive, dark halos might be rather common. Thus, it seems that one is left to speculate that the conditions at the time of protogalactic collapse were somehow favourable to the production of larger numbers of globular clusters in M87 than in other galaxies.

The luminosity distribution of M87 globulars has been studied by Racine (1968), Sandage (1968), Hanes (1977a), and Strom et al. (1981). Baum (1955) had already attempted to determine the distance

to M87 by comparing luminosities of the brightest clusters in M87 with those in M31, though Hanes (1977b) was able to secure a more reliable determination by using a much larger sample and comparing them with Galactic globular clusters. Harris and Racine (1979) have suggested that the luminosity functions of globular clusters in the local group follow a normal distribution with a mean absolute magnitude and dispersion which are fairly similar from galaxy to galaxy. If one assumes that this form of the luminosity function is appropriate to globular clusters in galaxies outside the local group as well, then by fitting the appropriate Gaussian to a large enough sample of clusters in a given galaxy, one should in principle be able to determine a reasonable value for the galaxy's distance modulus. This approach was used in Paper I to determine a distance to M87 which gave good agreement with similar values determined using other methods (Aaronson and Mould 1983). It has been pointed out by Sandage and Tammann (1985), however, that this method of determining distances is probably not very accurate in view of the uncertainty surrounding the universality of globular cluster luminosity functions. Indeed, it was found in Paper I that the overall form of the luminosity function of M87 globulars appears not to follow that determined by Harris and Racine (1979) for the local group.

Studies of the number and distribution of globular clusters in galaxies outside the local group have become more and more numerous in the recent literature as a result of both improvements in detection and imaging technology as well as a recognition of the importance of

globular clusters as representing possible tracers of the early stages of galaxy evolution. The space distribution of globular clusters in M87 has been examined by Racine (1968), Harris and Smith (1976), Hanes (1977), Harris and Racine (1979), Strom et al. (1981), Forte et al. (1981), Harris (1985), and briefly in Paper I. The claim has been made (Racine 1968; Harris and Smith 1976; Forte et al. 1981; Paper I) that the surface density distribution of globular clusters is significantly flatter than the stellar luminosity profile. One possible suggestion is that M87 formed in a manner similar to that described by Gunn (1980), wherein the globular clusters formed some few times 10^8 years before the general halo population when the protogalaxy was considerably less centrally concentrated. On the other hand, Forte et al. (1982), Muzzio et al. (1984), and Muzzio (1985a, b) have suggested that M87 acquired its relatively extended distribution through numerous encounters with other members of the Virgo cluster over the age of the universe. Both of these suggestions, however, fail to account in a simple way for the radial gradient in the colour (metallicity) of M87 globulars observed by Strom et al. (1981).

The present study seeks to address some of the issues which have been mentioned above using recently acquired CCD images of M87. The images are sufficiently deep that star-like objects can be detected to $B \approx 26$, so that the luminosity function of globulars can be extended considerably past the $B \approx 22$ limit of Hanes (1977) and the $B \approx 23.5$ limit of Strom et al. (1981). The observations and their automated

reduction to a list of possible globular cluster candidates are discussed in Chapter 2. Appropriate corrections for completeness and contamination of the observed sample by foreground stars and background galaxies are considered in Chapter 3. The corrected sample is used to construct a luminosity function of M87 globular clusters, and the distance to M87 is determined in the manner described in Paper I. In Chapter 4, the luminosity distribution is considered as a function of projected radius in order to look for possible trends in the data. The spatial distribution of clusters is also determined, and the results are compared with those of previous investigators. Simple dynamical models which could explain the observed distribution of M87 globulars are investigated in Chapter 5, where the effects of such depletion mechanisms as dynamical friction and globular cluster stripping are also examined. The results of the present study are briefly summarized in Chapter 6.

CHAPTER 2

OBSERVATIONS AND DATA REDUCTION

The present study is based primarily on observational data acquired in February 1984 by S. van den Bergh and C. Pritchett using the 3.6 meter Canada-France-Hawaii Telescope atop Mauna Kea, Hawaii. The observations were made using an RCA CCD detector mounted at prime focus and were spread over a period of five nights as it was the intent of the investigators to search for rapidly varying sources indicative of novae in the halo of M87 (van den Bergh 1981, Pritchett and van den Bergh 1984). The region of interest, a 2.2'x 3.3' field centered about one arcminute east of the core of M87, was observed in the B bandpass in three 20 minute exposures on each of the five nights for a total integration time of about five hours. Though similar observations were made of a region centered one arcminute west of M87, the overall integration time invested on this field was somewhat less than for the east field and the west field was subsequently dropped from analysis. Further information has been taken from the observing log and is contained in Table 1.

Table 1

CFHT CCD Observations of M87

Date UT	Filter	Object	UT Start	Int Time	Δx (") ^a	Δy (") ^a	Δx (") ^b	Δy (") ^b
24/02/84	B	M87 E	09:56	00:21:41	0.07	-0.02		
24/02/84	B	M87 E	10:20	00:20:00	0.00	0.00	-2.45	5.45
24/02/84	B	M87 E	10:41	00:20:00	-0.05	0.03		
25/02/84	B	M87 E	10:03	00:20:00	0.12	0.00		
25/02/84	B	M87 E	10:24	00:20:00	0.00	0.00	0.00	0.00
25/02/84	B	M87 E	10:45	00:20:00	-0.16	0.02		
26/02/84	B	Virgo Field	10:23	01:00:00	0.00	0.00		
26/02/84	B	M87 E	11:44	00:20:00	0.08	0.02		
26/02/84	B	M87 E	12:05	00:20:00	0.00	0.00	3.86	6.78
26/02/84	B	M87 E	12:26	00:20:00	-0.06	-0.05		
27/02/84	B	Virgo Field	11:26	00:45:01	0.18	0.05		
27/02/84	B	Virgo Field	12:12	00:45:00	0.00	0.00		

Table 1 - continued

Date UT	Filter	Object	UT Start	Int Time	Δx (") ^a	Δy (") ^a	Δx (") ^b	Δy (") ^b
27/02/84	B	M87 E	13:17	00:20:00	0.01	0.04		
27/02/84	B	M87 E	13:38	00:20:00	0.00	0.00	9.51	-1.82
27/02/84	B	M87 E	13:59	00:20:00	-0.04	-0.04		
28/02/84	B	M87 E	09:56	00:21:38	0.15	-0.03		
28/02/84	B	M87 E	10:20	00:20:00	0.00	0.00	1.21	-0.23
28/02/84	B	M87 E	10:40	00:20:00	-0.10	0.08		
28/02/84	B	Virgo Field	12:46	00:30:00	0.40	-0.04		
28/02/84	B	Virgo Field	13:17	00:30:00	0.00	0.00		
28/02/84	B	Virgo Field	13:47	00:30:00	-0.05	-0.19		

^aRelative coordinates for observations taken on the same night.

^bCoordinates relative to the coadded observations of 25/02/84.

2.1 Preliminary Reductions

Initial reduction of the raw data was performed using the University of Victoria Physics Department's VAX 11/750 minicomputer and International Imaging Systems (I²S) Model 70 image processing system. Computational and interactive operations were carried out using the high-level, image-processing command language R2D2 developed by C. Pritchett. The interested reader is referred to the manual describing R2D2 command options for instructions on its use, capabilities, and limitations.

Preliminary reductions were performed as follows. a) The floating bias level of each raw image frame was determined from the overclocked pixels. These pixels were subsequently removed, and the determined bias level was subtracted from each pixel in the remaining frame. b) A dedicated bias frame obtained during the observing run was subtracted pixel-by-pixel from each raw image. c) A median "dark" frame was determined from a series of "darks" taken during the observing run, and the result was again subtracted pixel-by-pixel from each image. d) Each image frame was divided pixel-wise by a median dome flat, itself corrected for large scale non-flatness through division by a median of sky flats taken during twilight skies.

The separation of the observations of M87 into nightly instalments, necessary for the detection of time-dependent light variations, required the mutual alignment and coaddition of the fifteen separate frames into one deep image to which photometry

algorithms could be applied. Since the telescope could not be pointed in exactly the same direction from night to night, and indeed, from one twenty minute exposure to the next, it became necessary to align each image with some reference before coadding the set. This alignment was subject to errors typically around 0.07 pixels (standard deviation) between images made on the same night, and about 0.12 pixels from one night to the next. At the prime focus of the Canada-France-Hawaii telescope, one pixel ($30 \mu\text{m}$ square) corresponds to about 0.41 arcseconds on the sky and hence, shifting individual frames with respect to one another did not compromise the seeing significantly. On the other hand, flaws and "hot spots" inherent to the detector, while being diminished in relative intensity, were unavoidably multiplied through coaddition.

Though single pixel flaws were too numerous to find and correct individually, two obviously bad columns were adjusted in each image using the R2D2 command FIXCOL, which replaced each pixel intensity value in the column with a mean value determined from pixels in the same row in a specified number of neighboring columns. This was done primarily to avoid runaway detections along these columns by the R2D2 object finding algorithm, though the photometry package eventually used turned out to be largely immune to such tendencies.

Each twenty minute observation was aligned individually with a single image chosen to lie approximately central to the other two taken on the same night in an effort to minimize the border areas which had to be discarded due to background discontinuities. Relative

coordinates of the images were determined by comparing calculated centroids of a set of thirteen bright, reasonably isolated, starlike images. These images were examined visually to ensure proper identification in each frame, and an iterative-outlier rejection method was used to minimize the standard deviation in the mean x and y shifts necessary to bring the frames into alignment. Through the R2D2 command SCROSH, relative position angles were also calculated, but were consistently found to be smaller than their associated errors. Consequently, it was assumed that the detector had not been inadvertently rotated during the observing run, and this extra degree of freedom in the alignment was disallowed.

The images were appropriately translated and coadded in sets of three corresponding to each night's observations. The five resulting frames were multiplied by an intensity-reducing coefficient of 0.2 to prevent integer overflows in the core region of M87 upon subsequent coaddition. Using the same set of thirteen reference objects, relative coordinates were calculated for each frame with respect to the coadded observations acquired on the night of 25/02/84, again with the intent to minimize areas of background discontinuity near the edges, and to retain the image of the core of M87 within the final field. The frames were then appropriately translated and "stacked" onto the observations of February 25. Table 1 contains the sequence of frame mergers and the actual shift values used.

The resulting frame was trimmed to an area of 275 by 465 pixels to remove the intensity discontinuities introduced around the

perimeter by frame mergers in order to avoid erroneous sky-background and object magnitude determinations. Using the R2D2 command PHOTPROF, a final mean coadded full-width-at-half-maximum (FWHM) for the thirteen reference objects was determined to be 3.4 ± 0.2 pixels, corresponding to 1.4 ± 0.1 arcseconds.

2.2 Background Subtraction

The image at this point possessed a very high signal-to-noise ratio so that many hundreds of starlike images could be visually picked out on the monitor against the M87 halo background. Due to the very sharp rise in the background intensity towards the core, however, it seemed evident that no automatic photometry routine would be able to determine local background intensities sufficiently reliably to permit the extraction of reasonably accurate object magnitudes. Consequently, it was decided to remove the smooth halo and sky background as much as possible. To this end, the halo of M87 was represented by the de Vaucouleurs law (de Vaucouleurs and Nieto 1978):

$$\mu = 14.615 + 2.658r^{1/4} \quad (1)$$

where r is in arcseconds and μ has units of B magnitudes per arcsecond squared. The radial intensity variation is consequently described

by:

$$I \propto 10^{(\alpha - 0.851r^{1/4})} \quad (2)$$

where α is some constant and the units are now pixels and ADU (analog-to-digital unit) per pixel squared.

An artificial galaxy was generated in a separate image file which obeyed exactly such an intensity profile, where α was arbitrarily chosen to have a value of 6. This image was subsequently fitted in a least-squares sense to the original data frame using the R2D2 command FITARR, so that on a pixel by pixel basis:

$$I_o(x,y) = A + BI_g(x,y) \quad (3)$$

where $I_o(x,y)$ corresponded to the intensity values of pixels in the observed data frame and $I_g(x,y)$ were the calculated values in the generated image. The fit was performed for pixels lying at radii roughly greater than ten arcseconds, since the $r^{1/4}$ law given in equation (1) was found by de Vaucouleurs and Nieto (1979) to be inadequate to fit the intensity profile at smaller radii. This resulted in an adopted sky-halo background intensity profile:

$$I_b = 882 + (0.872)10^{(6 - 0.851r^{1/4})} \quad (4)$$

which, less a level of 200 ADU across the frame, was subtracted

pixel-wise from the real data. A positive floor level of 200 ADU was retained simply to keep the interference between the slightly elliptical isophotes of the real data and the assumed-circular generated galaxy from producing regions of negative intensity, which would affect both photometry algorithms and visual examination of the data on the monitor. A reproduction of the resulting background-subtracted image is shown in Figure 1.

2.3 The Photometry Software Package

As can be seen from Figure 1, crowding of images, though not severe, is significant from the standpoint of aperture photometry. Consequently, though R2D2 aperture photometry would have been much quicker, it was decided to utilize a crowded-field, profile-fitting photometry package instead. DAOPHOT, a photometry software code developed by P. Stetson (1985) of the Dominion Astrophysical Observatory for use with digitized images of Galactic globular clusters, was both easily available and reputed to be reasonably fast. Most of its subroutines could be run in batch mode, and for interactive operations which required visual reference to a monitor, simple format-conversion routines were used to permit the transformation of image files from the format required by DAOPHOT to that used in R2D2. Although an abbreviated sequence of operations

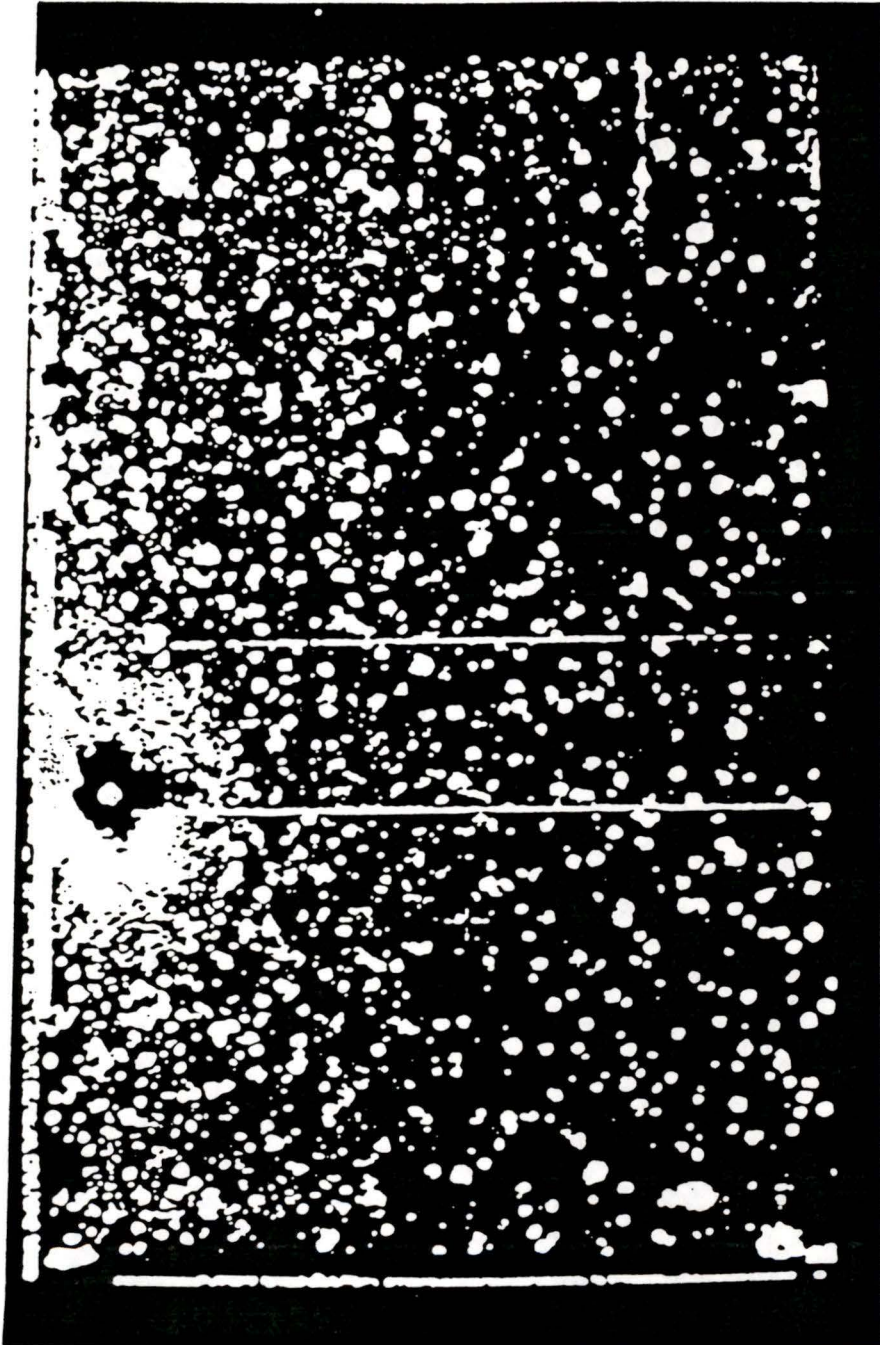


Figure 1. Reproduction of background-subtracted CCD image.

using DAOPHOT is given presently, the reader is referred to the DAOPHOT user's manual for a complete description of available subroutines and their proper use.

Unfortunately, DAOPHOT could not be run for the data in hand without certain minor modifications. Since the intensities contained in the image file were no longer proportional to the number of photons received by the detector (being variously diminished by background subtraction), the noise distribution (assumed to reflect Poisson statistics) could not be determined without first providing DAOPHOT with the original intensity as well as the appropriate proportionality constant. This expected noise level was important from the standpoint of providing DAOPHOT with pixel weighting and rejection criteria in routines designed to find local intensity maxima, determine the best possible point-spread function (PSF), and perform accurate photometry. In iterative calculations, pixels were weighted as the inverse square of the number of noise sigma away from the previous best-fit model, and rejected entirely if they fell beyond twenty sigma from the model. Consequently, provision was made in each appropriate DAOPHOT subprocess to add back the subtracted background, as well as divide the result by the previously discussed intensity reducing coefficient of 0.2, to reproduce the original ratio of approximately 25 photons per ADU. In addition, a value of 2.5 ADU was assigned to the CCD readout noise contribution, corresponding to 75 equivalent photons per frame for the RCA CCD and propagating as the square root of the number of added frames.

2.4 Object Detection

In the FIND routine, the expected value of sigma determined the dividing line between possible faint objects and the noise. With the modifications made to the program, the threshold intensity for detection became variable over the image and was user-defined as a fixed number of sigma above the local background. Several different values for this threshold were tested, ranging from 1 to 5 sigma, and it was found that the number of detected images increased with decreasing threshold until a plateau was reached at around 1 sigma. If the objects detected at this magnitude level were primarily fluctuations in the noise, then the number of detections would normally be expected to increase even more steeply at still smaller thresholds. The fact that this was not the case inspired a certain degree of confidence in the discretionary criteria of the routine. A visual examination of the faintest objects detected at various input threshold values led to the eventual adoption of a 2.5 sigma threshold for all further reductions.

The operation of the object-detection routine involved an initial convolution of the entire image file with a lowered, truncated Gaussian whose FWHM was specified by the user as that determined for the stellar images. The convolved data were then searched for local brightness enhancements which exceeded the value determined by the user-supplied threshold. Object candidates were tested for permissible shape parameters through the statistics

"SHARP" and "ROUND". The former was used to reject either "hot" or "cold" pixels, and was computed as the ratio of the heights of the best-fitting δ -function and the best-fit Gaussian. The ROUND statistic was calculated as the fractional difference in height between best-fit, one-dimensional Gaussians determined in the x and y directions, respectively. Its usefulness lay more in recognizing possibly bad columns and rows and less in identifying possible background galaxies since elongation was sought only in the x and y directions.

Although the DAOPHOT user's manual strongly recommended the use of the default values provided for the limiting values of these statistics, experiments were carried out to ensure that the results could not be improved by altering them somewhat. In particular, the limits of SHARP and ROUND were widened to $0.01 < \text{SHARP} < 2$ and $-2 < \text{ROUND} < 2$ from the default values of $0.1 < \text{SHARP} < 1$ and $-1 < \text{ROUND} < 1$. The resulting number of detected objects promptly rose by a rather dramatic 30%. Plotting SHARP versus magnitude, however, showed that only a tiny fraction of the newly detected images had SHARP values outside the previous default limits. Presumably the newcomers were not to be associated with, for example, cosmic rays or hot pixels. To be sure, a visual examination of single-pixel intensity enhancements most likely due to cosmic ray strikes was carried out and gratifyingly, none of the examined objects was found to be contained in the FIND output list. SHARP values for these pixels were generally much higher than the limits set above.

A similar plot of ROUND versus magnitude was also found to be revealing. Approximately one third of the excess number of detected images had ROUND values greater than 1, and the other two thirds had ROUND values less than -1. All of the extra objects were confined to low intensities. The likely conclusion to be drawn was that many of the extra objects were being found along bad rows, and that the majority of them were to be associated with bad columns. An examination of the positions of these objects on the monitor showed that this was indeed the case, with as many as 60 or 70 objects observed to be concentrated along an obviously bad row.

In view of these results, the limiting values for SHARP and ROUND were returned to their original default values. Visual examination revealed that, using these values, there was no obvious concentration of detected images along bad rows or columns, and neither were apparent cosmic ray events being allowed to infiltrate the list of detections. Further narrowing of these limits would presumably have been counterproductive in the sense that many of the fainter and therefore more ragged images would have been discarded. Subsequent fitting routines would have their own object-rejection criteria and consequently, all further use of FIND was made using the default parameters.

2.5 Aperture Photometry

The next stage in the use of DAOPHOT required the running of the PHOT concentric-aperture photometry routine. Though a dozen user-specified, concentric apertures were available for this step, only a single aperture three pixels in radius was actually used in order to speed up the reductions. Note that the magnitudes so determined were used simply as starting values for the more sophisticated profile-fitting operations yet to come.

Perhaps a more important outcome of PHOT was the determination of the local "sky" or background intensities specific to each object in the FIND candidate list, since this was the only point in the reductions where these values were extracted. An object's background level was taken to be the modal intensity in an annulus centered on the object and extending from 15 to 25 pixels (6.2 to 10.3 arcseconds) away from it. Though the values determined in this manner may have been somewhat problematic in cases of extreme crowding, it was decided that the data in hand did not exhibit a sufficient surface density of images at radii greater than about twenty arcseconds from the core of M87 to warrant concern. For selected, more highly crowded regions of the field, calculated sky values were checked interactively on the I²S monitor and found to be generally convincing. Since the minimum background intensity was found to be about 50 ADU, a "bad pixel" threshold (below which a given pixel would not be considered in magnitude calculations) was assigned a value of zero ADU.

2.6 Determination of the Point-Spread Function

Before profile fitting of individual images could begin, an appropriate point-spread function had to be computed. Since the determination of accurate magnitudes depended on the use of a PSF which was truly representative of objects in the frame, a considerable amount of time was spent selecting and iteratively rejecting possible PSF candidates.

The PSF was calculated by first fitting a Gaussian function to the central portion of the brightest and most isolated candidate PSF image. This Gaussian was subsequently integrated over the area of each pixel, and the integral was fitted to individual pixel intensities. When an analytic expression for the PSF had been determined, a table was generated in which were contained the pixel-wise differences between the analytic intensity profile and the observed pixel intensities. The analytic PSF determined for the primary PSF candidate could then be scaled to other candidates, subtracted off, and the differences added to the table.

Since the PSF candidates were chosen to be reasonably isolated in the first place, the Gaussian was fitted over a region out to a comparatively large radius of 4 pixels from the calculated centroids, while the difference table was generated for a region out to 11 pixels (4.5 arcseconds). If the PSF candidate had neighbors within about two fitting radii, then the PSF determination was iterative in the sense that the neighboring images would have to be subtracted out repeatedly

using the previous PSF until the solution converged. When a suitable list of PSF images had been determined (the faintest one being no more than a magnitude fainter than the primary PSF candidate since for still fainter objects, the values entered into the difference table would effectively introduce only noise) the whole process was repeated to improve convergence. Background galaxies were removed as much as possible from the candidate list by subtracting an appropriately scaled PSF from each candidate and looking for evidence of systematic over-subtraction in the core. A total of six iterations were performed until the output difference tables for successive trials were found to be identical. The final list of objects used to calculate the PSF is contained in Table 2, where the identification numbers refer to the final output object list given in Table 4.

2.7 Recovery of Hidden Objects

In order to find faint images hidden from the detection routine FIND by nearby bright objects, the newly-calculated PSF was used to subtract out all images listed in the output file of the aperture photometry routine. Since accurate magnitudes were not important at this stage, the PSF was scaled to individual images using the single-profile fitting routine PEAK, which did not attempt to fit images in a crowded field simultaneously. After scaling, the known

Table 2

Objects Used to Calculate the Point-Spread Function

ID# ^a	x (pix)	y (pix)	B (mag)
766	146.33	300.12	20.569
1124	225.77	439.78	20.929
220	164.18	81.89	21.281
844	242.90	328.41	21.346
1019	221.67	388.54	21.677
1081	196.96	418.47	21.685

^aRefer to Table 4.

images were subtracted out and a new frame was generated containing the residuals. FIND was used to detect any intensity enhancements in this image which would have been hidden in the original data frame.

Of course, it was unavoidable that images imperfectly subtracted due to noisy or ragged intensity profiles would be picked up by the detection routine, and in fact, this second image list was nearly as large (~1000 images) as the original. In the multiple-profile fitting routine NSTAR, however, provision was made to reject the fainter member of a pair if the separation was less than 0.4 pixels. Before running this latter routine, however, the first and second FIND image lists were merged, and the aperture photometry routine was used to determine starting magnitudes for the resulting ~2300 possible objects.

2.8 Multiple Profile Fitting

In order to keep cpu time requirements within reason when using the multiple-profile fitting routine NSTAR, objects in the PHOT output list were separated into natural groups representing different areas of the field in which all objects were within a specified maximum distance from one another. The largest number of individual profiles which NSTAR could fit simultaneously was sixty. Using the subprocess GROUP, the image list was divided into several hundred natural groups

by successively lowering the maximum separation until all groups were smaller than this limit. Of course, the smaller the specified maximum separation within a particular group, the less accurate would be the profile fitting for the fainter objects near the edge of the group, where the extended profiles of objects in neighboring groups could influence the scaling of the PSF.

A PSF fitting radius of three pixels was used for all NSTAR runs, and the pixel weighting scheme employed in the fit was such that a pixel lying right at the edge of the fitting region would have a weight of zero. The lowest value for the minimum separation of objects in two different groups was six pixels, which fortunately meant that at least the fitting regions of two neighboring groups could not overlap. The group sizes and maximum separations required to keep the number of objects within a particular group to less than sixty are shown in Table 3. Note that this table was developed from the final object list in Table 4, after more than half the original number of object candidates had been deleted and crowding (as far as profile fitting was concerned) was substantially reduced. NSTAR was run separately for each original natural group, and about twelve cpu hours later, the first list of fitted instrumental magnitudes was in hand.

A large number of detected objects were deleted for various reasons, including a) rejection of one member of a duplicate entry in the object list, b) rejection any time an object was found to be more than 12.5 magnitudes fainter than the primary PSF object, and c)

Table 3

Distribution of Natural Groups for Objects in Table 4

group size	maximum object separation (pix)		
	10	9	8
1	88	7	3
2	31	4	3
3	18	2	1
4	11	3	0
5	5	1	0
6	7	1	1
7	1	0	0
8	4	2	1
9	1	1	0
10	2	1	0
12	1	1	0
14	0	2	1
15	3	0	0
16	2	1	2
17	1	0	0
18	1	0	0
19	2	0	0
20	1	0	0
21	1	1	0
22	0	2	0
25	1	0	0
32	1	0	0
36	1	0	0
37	1	0	0
38	1	0	0
41	0	1	0
60	0	0	1
total # of objects	754	241	132

rejection of the faintest objects in a given group if their brightnesses were less than 1, 1.5, or 2 sigma (where sigma is the expected noise level discussed in section 2.3) above zero in the 4th, 8th and 12th iterations, respectively. With the inclusion of a time-saving, 25 iteration limit on the profile fits, accuracy could sometimes be compromised if objects were deleted near this limit, even though the iteration counter was backed up by one every time this occurred. Consequently, the newly-acquired, reduced list of objects was separated into natural groups and multiple profile fitting was performed all over again.

Though this operation could have been carried out three or more times, the total number of objects rejected during the second run of NSTAR was only ~100, as opposed to the ~1000 or so deleted during the first run. In addition, these objects were generally rejected at fairly low iteration numbers, allowing sufficient time for the overall profile fit to the group to converge. Consequently, it was deemed unnecessary to perform any further runs. Note that the NSTAR criterion for convergence for a given group was fairly conservative in requiring that no object's magnitude be allowed to change by more than 0.01 magnitudes from one iteration to the next.

2.9 Photometric Calibration

Photometric calibration was performed by C. Pritchett (Pritchett and van den Bergh 1984) using UBV standards of Landolt (1973, 1983) and UBVRI standards of Schild (1983) in M67. This involved an examination of the intensity profiles of several isolated objects to determine the extent of their profiles and hence their total area-integrated magnitudes. The resulting aperture corrections were then applied to the profile-fitted magnitudes determined by NSTAR. Finally, photometry of the standard stars given above was compared with the standard values to give a final mean zero-point correction to the DAOPHOT magnitudes of -0.18 mags.

The final list of objects, along with calculated centroids, corrected magnitudes, and mean errors is contained in Table 4. The errors calculated by DAOPHOT have been averaged over one magnitude intervals and over concentric regions of equal area, and the results are plotted in Figure 2. As expected, the mean magnitude errors increase with both increasing magnitude and decreasing projected radius, in accordance with increased crowding and background noise.

Strom et al. (1981) have performed UBR photometry of some 1700 globular clusters in the region 1.5 to 9 arcminutes from the center of M87 down to a limiting magnitude of $B \approx 23.5$. The 400 or so clusters which lie within three arcminutes of the center of M87 were mapped onto the coordinate frame of the present data by rotating the coordinate frame of Strom et al. 83° in the anti-clockwise (N \rightarrow W)

direction. The apparent center of M87 was found to occur at pixel coordinates $x = 7$, $y = 185$ by calculating centroids of isophotes in the radial region 10 to 110 arcseconds using the R2D2 command CONTOUR. This corresponds to coordinates $x = 423.5$, $y = 426.1$ arcseconds in the coordinate frame of Strom et al. A simple FORTRAN code was then used to compare positions and magnitudes of the 93 objects remaining in the common field of view, where tolerances of 2 arcseconds and 1.5 magnitudes were specified, respectively. A list of all objects found to be common to both samples is contained in Table 5, and the resulting relation between DAOPHOT-derived magnitudes and those of Strom et al. is shown in Figure 3. It is apparent from this figure that agreement is remarkably good, and no significant tendency to depart from a linear relation is evident. The mean difference in magnitude from the two sources is 0.03, with an rms scatter of 0.25 magnitudes.

Table 4

Objects Detected in M87 East Field

ID#	x (pix)	y (pix)	B	σ_B
1	151.4	2.4	23.14	0.04
2	220.6	2.5	23.59	0.03
3	40.3	3.0	24.99	0.14
4	138.2	3.1	25.72	0.34
5	83.5	3.4	26.71	0.52
6	95.2	3.7	21.82	0.04
7	237.6	4.3	25.30	0.10
9	172.4	5.3	22.65	0.01
10	117.0	7.0	24.18	0.06
11	21.2	7.1	24.62	0.17
12	245.9	8.8	26.40	0.29
13	61.5	8.9	25.16	0.14
14	35.8	9.3	25.53	0.21
15	207.1	9.9	24.62	0.06
16	56.8	11.0	25.52	0.18
17	99.7	11.4	24.54	0.12
18	67.6	11.4	25.37	0.15
19	9.6	11.7	24.27	0.10
20	94.1	12.2	24.59	0.12
21	52.2	13.1	26.26	0.32
22	114.1	14.1	25.14	0.08
23	164.6	14.2	26.05	0.25
24	168.8	14.6	23.83	0.03
25	48.5	14.8	22.97	0.05
26	66.7	15.5	25.19	0.11
27	85.4	15.6	24.23	0.10
28	94.3	16.2	24.71	0.09
29	179.1	16.3	23.90	0.03
30	98.9	16.9	24.02	0.10
31	222.2	17.4	24.73	0.17
32	102.8	17.6	24.65	0.11
33	245.9	18.0	25.05	0.09
35	73.7	18.6	24.97	0.14
36	42.1	18.8	26.01	0.29
37	67.0	18.9	24.03	0.04
38	252.5	19.4	25.42	0.19
39	23.6	19.7	25.65	0.24
40	224.4	19.8	23.70	0.08
41	49.5	20.4	22.55	0.02
42	111.5	20.5	21.29	0.01

Table 4 - continued

ID#	x (pix)	y (pix)	B	σ_B
43	185.9	20.7	25.84	0.16
44	93.9	20.7	24.42	0.11
45	69.3	20.9	25.27	0.13
46	83.3	21.0	24.62	0.10
48	35.7	21.9	24.40	0.06
49	39.9	22.8	26.23	0.34
50	133.9	23.1	24.94	0.13
51	256.0	23.1	25.55	0.14
52	207.8	23.4	23.58	0.03
53	168.3	24.1	23.72	0.05
54	74.2	24.8	25.25	0.14
55	93.3	25.3	24.41	0.10
56	43.3	25.9	23.77	0.04
57	110.4	26.2	24.14	0.06
58	217.4	26.9	25.52	0.21
59	129.7	27.4	24.79	0.14
60	87.5	27.5	24.55	0.11
61	69.8	28.3	25.62	0.21
62	94.5	28.4	24.54	0.13
63	82.6	29.1	24.82	0.13
64	144.9	29.6	21.41	0.04
65	173.2	29.6	25.64	0.14
66	74.9	29.7	25.04	0.13
67	108.8	29.8	25.13	0.12
68	18.0	29.9	24.90	0.24
69	196.4	30.6	20.78	0.04
70	134.1	31.3	22.69	0.02
71	38.5	31.3	22.97	0.04
72	106.3	31.6	25.74	0.19
73	83.2	32.5	24.11	0.06
74	86.5	32.9	24.53	0.10
75	182.0	33.5	26.02	0.17
76	108.7	33.5	25.35	0.12
77	55.9	33.8	25.78	0.18
78	228.2	33.8	25.86	0.20
79	153.3	34.1	23.40	0.03
80	75.6	34.8	25.09	0.13
81	69.4	35.2	25.36	0.12
82	106.0	35.9	25.05	0.09
83	242.9	36.3	25.80	0.18
84	13.4	36.4	25.10	0.15
85	234.6	36.6	23.67	0.04
86	111.7	36.6	25.31	0.11

Table 4 - continued

ID#	x (pix)	y (pix)	B	σ_B
87	172.3	36.7	26.00	0.17
88	137.4	37.6	25.00	0.13
89	89.6	38.1	24.60	0.12
90	239.9	38.7	26.89	0.40
91	149.1	39.1	25.30	0.14
92	229.3	39.8	24.16	0.06
93	217.1	39.9	26.20	0.25
94	99.7	40.0	25.50	0.13
95	172.1	40.6	26.05	0.25
96	83.8	41.1	25.26	0.15
97	142.0	41.4	25.38	0.13
98	115.0	41.6	23.73	0.04
99	159.1	42.0	25.35	0.22
100	74.2	42.8	22.79	0.02
101	174.3	43.0	26.06	0.28
102	256.3	43.0	23.01	0.01
103	189.6	43.1	23.10	0.02
104	236.0	43.4	25.11	0.09
105	167.5	43.4	25.16	0.15
106	79.5	43.8	25.56	0.20
107	186.0	45.0	25.21	0.10
108	227.2	45.3	25.76	0.17
109	272.1	45.5	23.98	0.03
110	171.4	45.6	25.48	0.16
111	10.2	45.8	25.46	0.23
112	116.9	45.9	25.62	0.16
113	148.5	45.9	26.28	0.28
114	121.9	46.1	26.25	0.28
115	248.6	46.7	25.19	0.12
116	232.4	47.2	25.28	0.09
117	184.5	47.6	25.88	0.20
118	82.8	47.8	25.19	0.13
119	136.0	48.0	25.13	0.09
120	71.8	49.0	24.28	0.09
121	163.4	49.2	23.18	0.04
122	176.8	49.6	26.43	0.29
123	42.0	49.6	24.84	0.12
124	244.2	50.2	26.25	0.44
125	120.8	50.5	26.63	0.33
126	28.6	50.5	25.54	0.19
127	171.4	50.9	26.02	0.40
128	49.6	51.0	26.04	0.43
129	95.8	51.6	23.44	0.08

Table 4 - continued

ID#	x (pix)	y (pix)	B	σ_B
130	150.8	52.0	25.43	0.24
131	131.4	52.1	24.22	0.08
132	162.6	52.3	21.80	0.01
133	178.3	52.5	25.03	0.09
134	93.4	53.3	24.44	0.10
135	171.5	53.5	24.17	0.06
136	167.8	53.5	24.94	0.10
137	17.2	53.6	22.54	0.02
138	218.9	54.3	24.93	0.10
139	90.2	54.8	24.62	0.14
140	152.1	54.8	24.35	0.21
141	128.2	55.6	23.50	0.04
142	110.6	56.0	24.37	0.12
143	95.8	56.5	22.51	0.02
144	250.7	56.6	22.22	0.01
145	58.2	57.0	24.93	0.11
146	180.9	57.1	25.84	0.42
147	213.9	57.5	24.26	0.23
148	212.1	57.6	23.68	0.15
149	6.6	58.2	24.95	0.29
150	99.2	58.8	23.97	0.09
151	117.0	58.8	24.69	0.11
152	135.1	59.2	26.87	0.45
153	235.1	59.2	24.75	0.10
154	22.3	59.5	24.53	0.12
155	106.1	61.3	24.34	0.12
156	181.5	61.4	24.94	0.20
157	38.8	61.8	24.78	0.14
158	179.6	62.3	24.28	0.12
159	102.3	62.7	23.13	0.05
160	43.3	63.0	23.71	0.05
161	113.6	63.1	24.55	0.09
162	193.8	63.3	24.90	0.13
163	120.9	64.1	24.90	0.12
164	219.3	64.4	25.17	0.10
165	50.7	64.5	22.61	0.02
166	93.6	65.0	23.88	0.11
167	196.7	65.1	23.82	0.04
168	271.1	65.1	23.77	0.03
169	208.6	66.0	22.08	0.02
170	55.6	66.3	24.01	0.04
171	107.3	66.7	24.06	0.09
172	124.9	66.8	24.51	0.10

Table 4 - continued

ID#	x (pix)	y (pix)	B	σ_B
173	84.9	67.3	24.32	0.12
174	138.7	67.8	26.58	0.30
175	118.3	67.8	24.66	0.12
176	93.6	68.1	24.21	0.11
177	224.9	68.3	24.34	0.08
178	192.3	68.4	24.71	0.12
179	199.8	69.0	24.44	0.07
180	79.4	69.2	24.24	0.08
181	69.5	69.4	24.47	0.12
182	213.1	70.1	24.67	0.08
183	67.1	71.7	23.67	0.06
184	143.0	71.8	24.28	0.06
185	92.0	72.0	24.29	0.11
186	135.6	72.2	25.06	0.12
187	97.5	72.2	23.55	0.07
188	205.3	72.3	25.91	0.17
189	5.7	72.3	24.01	0.13
190	73.3	72.5	24.59	0.14
191	108.3	72.6	24.59	0.14
192	250.4	72.8	24.45	0.05
193	114.1	72.8	24.43	0.11
194	268.2	72.8	23.33	0.06
195	38.2	73.7	24.37	0.14
196	211.1	73.8	24.80	0.07
197	82.7	74.1	22.11	0.01
198	87.5	76.2	24.23	0.11
199	8.6	76.2	23.41	0.08
200	125.4	76.2	26.18	0.33
201	96.7	76.4	23.73	0.08
202	24.7	77.1	22.38	0.02
203	232.2	77.2	25.74	0.18
204	142.5	77.3	23.70	0.07
205	217.3	77.4	25.98	0.28
206	61.2	78.6	25.41	0.24
207	83.6	78.9	23.33	0.03
208	262.0	78.9	24.62	0.08
209	121.4	79.0	26.22	0.34
210	14.3	79.3	23.92	0.09
211	253.1	79.5	22.56	0.01
212	208.7	79.8	22.97	0.02
213	6.4	80.2	24.33	0.28
214	177.1	80.7	23.33	0.02
215	189.6	80.8	23.44	0.03

Table 4 - continued

ID#	x (pix)	y (pix)	B	σ_B
216	67.7	81.2	23.07	0.03
217	124.5	81.2	25.92	0.21
218	113.6	81.3	22.99	0.03
219	38.1	81.4	25.20	0.27
220	164.2	81.9	21.28	0.01
221	5.1	82.0	23.97	0.26
222	110.9	84.4	25.47	0.15
223	53.6	84.8	24.45	0.18
224	84.0	84.8	22.03	0.01
225	205.6	85.6	25.40	0.11
226	106.9	85.9	25.17	0.11
227	65.1	85.9	23.02	0.03
228	227.9	86.3	23.79	0.03
229	20.0	87.1	23.65	0.04
230	29.9	87.1	26.10	0.47
231	102.5	87.4	25.46	0.17
232	264.7	88.8	24.58	0.07
233	160.8	89.1	25.36	0.11
234	53.2	89.3	21.22	0.02
235	97.8	89.5	24.84	0.13
236	34.0	90.0	25.10	0.11
237	192.7	90.5	23.13	0.02
238	137.4	91.0	23.83	0.08
239	57.8	91.0	22.93	0.04
240	243.5	91.0	24.29	0.04
241	115.8	91.2	25.24	0.13
242	119.8	92.1	24.84	0.15
243	145.9	92.5	25.66	0.36
244	91.6	92.6	25.55	0.18
245	97.2	92.7	24.59	0.12
246	20.2	93.4	22.61	0.03
247	69.5	93.6	24.48	0.17
248	24.2	93.6	20.94	0.03
249	163.0	93.9	26.10	0.27
250	39.0	95.1	24.42	0.06
251	218.6	96.1	26.38	0.25
252	48.8	96.6	24.98	0.15
253	126.4	97.1	24.05	0.15
254	45.7	97.4	24.89	0.14
255	85.8	97.5	24.59	0.13
256	30.3	97.5	21.29	0.01
257	179.7	98.6	22.27	0.01
258	272.3	98.9	25.44	0.16

Table 4 - continued

ID#	x (pix)	y (pix)	B	σ_B
259	207.9	99.1	23.96	0.05
260	156.7	99.6	25.19	0.13
261	211.7	99.8	25.63	0.16
262	114.9	99.8	24.29	0.14
263	219.6	100.5	25.61	0.14
264	254.7	100.7	22.83	0.03
265	70.1	100.9	24.15	0.17
266	17.1	100.9	23.98	0.09
267	203.3	101.7	23.39	0.07
268	31.4	102.1	23.92	0.06
269	187.5	102.5	23.83	0.03
270	245.4	102.8	25.23	0.31
271	154.0	103.4	25.78	0.16
272	122.6	104.0	24.37	0.14
273	133.4	104.8	24.75	0.15
274	239.9	104.9	26.10	0.38
275	116.0	104.9	24.39	0.12
276	81.3	105.5	22.90	0.04
277	24.0	105.8	23.81	0.09
278	21.1	106.1	22.19	0.04
279	150.1	106.5	25.41	0.13
280	220.7	106.6	24.91	0.12
281	44.3	106.7	24.67	0.09
282	100.6	107.0	24.37	0.05
283	77.5	107.1	22.40	0.02
284	111.3	107.9	22.92	0.08
285	196.9	107.9	25.13	0.15
286	210.2	108.2	25.56	0.12
287	129.4	108.4	24.89	0.14
288	272.8	108.5	24.94	0.09
289	234.0	108.8	24.89	0.12
290	154.1	108.8	26.08	0.25
291	171.8	109.0	24.49	0.14
292	202.0	109.5	25.17	0.12
293	31.8	109.6	24.12	0.08
294	173.4	110.2	25.89	0.42
295	94.1	111.8	23.96	0.04
296	193.5	112.1	25.03	0.14
297	124.4	112.3	24.89	0.14
298	158.1	112.6	25.90	0.31
299	171.6	113.0	25.59	0.20
300	155.5	113.0	26.47	0.42
301	215.0	113.7	25.40	0.11

Table 4 - continued

ID#	x (pix)	y (pix)	B	σ_B
302	186.9	114.0	24.47	0.14
303	150.4	114.2	25.45	0.16
304	198.0	114.3	24.33	0.08
305	120.4	114.8	23.21	0.04
306	174.2	115.0	22.56	0.02
307	112.9	115.1	23.36	0.05
308	74.3	115.3	24.77	0.10
309	136.8	115.7	25.50	0.16
310	211.6	116.1	23.81	0.08
311	155.2	116.3	24.36	0.05
312	122.6	116.4	24.94	0.17
313	25.7	116.5	22.28	0.02
314	84.4	116.6	24.49	0.09
315	192.9	116.9	25.12	0.14
316	55.0	117.1	23.27	0.05
317	189.8	117.5	22.68	0.02
318	107.5	118.1	23.81	0.06
319	127.9	118.2	25.93	0.32
320	116.2	118.3	25.13	0.16
321	247.1	118.6	25.24	0.12
322	142.6	119.2	26.39	0.48
323	75.9	119.2	24.73	0.18
324	82.8	119.3	25.03	0.11
325	173.0	119.8	26.48	0.39
326	78.1	120.2	24.70	0.17
327	273.0	120.3	23.11	0.01
328	26.5	120.3	24.12	0.09
329	215.7	120.4	25.18	0.30
330	157.0	120.4	25.16	0.16
331	217.7	121.2	22.98	0.04
332	127.2	121.8	24.17	0.06
333	131.5	122.3	23.63	0.03
334	35.6	123.2	24.66	0.15
335	76.6	123.6	25.85	0.39
336	42.3	123.6	22.70	0.03
337	213.2	125.7	24.01	0.03
338	25.8	125.8	22.37	0.02
339	268.1	125.9	23.35	0.02
340	265.0	126.1	24.77	0.06
341	170.3	126.2	24.00	0.04
342	260.9	126.3	24.03	0.03
343	107.2	127.8	24.78	0.15
344	90.0	128.5	24.10	0.11

Table 4 - continued

ID#	x (pix)	y (pix)	B	σ_B
345	100.8	128.9	23.41	0.03
346	41.2	129.6	23.53	0.05
347	72.3	130.1	23.11	0.03
348	63.7	130.2	21.93	0.02
349	29.1	130.8	24.48	0.15
350	255.0	130.9	23.47	0.02
351	45.7	131.3	24.63	0.14
352	110.7	131.9	24.87	0.10
353	206.3	133.1	21.18	0.02
354	138.3	133.2	25.10	0.10
355	104.6	133.3	25.74	0.24
356	38.4	133.4	22.36	0.03
357	53.3	133.8	24.49	0.26
358	144.4	133.8	24.39	0.05
359	178.0	133.9	24.00	0.06
360	28.6	135.8	23.53	0.07
361	249.5	136.1	23.21	0.01
362	93.4	136.3	23.93	0.06
363	167.6	136.7	24.30	0.09
364	236.9	137.4	23.57	0.05
365	207.0	137.6	22.71	0.06
366	231.0	137.9	22.19	0.02
367	16.0	138.0	25.22	0.30
369	67.8	138.6	25.16	0.20
370	27.7	140.2	21.73	0.01
371	260.5	140.9	23.20	0.03
372	17.2	141.6	23.56	0.06
373	262.6	142.2	24.85	0.15
374	150.5	142.5	24.70	0.06
375	93.2	143.8	25.36	0.19
377	70.0	144.2	21.90	0.02
378	220.4	144.6	25.04	0.13
379	156.9	144.6	23.84	0.04
382	162.0	146.7	23.69	0.05
383	229.7	146.9	23.50	0.03
384	154.7	147.6	22.85	0.02
385	28.7	148.0	22.82	0.05
386	56.0	148.4	23.23	0.10
387	210.4	148.6	25.18	0.12
388	33.5	149.4	23.08	0.09
390	58.1	150.6	22.99	0.06
391	271.5	150.8	25.04	0.08
392	73.6	150.9	23.89	0.17

Table 4 - continued

ID#	x (pix)	y (pix)	B	σ_B
393	225.9	150.9	26.04	0.23
394	80.4	150.9	22.70	0.08
395	171.9	151.0	24.02	0.07
396	95.2	151.1	25.91	0.48
397	137.2	151.6	24.87	0.09
399	92.0	151.9	22.37	0.02
400	260.5	152.1	24.92	0.10
401	218.8	152.2	25.17	0.11
402	239.6	152.6	24.73	0.11
403	2.6	152.8	23.37	0.51
404	212.8	153.1	25.32	0.10
405	140.0	153.2	25.61	0.19
406	188.3	153.4	26.12	0.43
407	269.8	153.5	22.88	0.01
408	59.1	153.7	22.87	0.06
409	234.4	155.4	23.09	0.03
410	187.8	156.2	23.08	0.04
411	58.7	156.3	24.42	0.44
412	196.4	157.2	22.36	0.03
413	246.4	162.0	22.10	0.03
414	243.1	162.3	24.89	0.19
415	59.9	162.7	21.31	0.04
416	215.7	163.1	23.61	0.07
417	27.8	163.4	22.58	0.19
418	213.0	163.7	24.48	0.12
419	129.1	164.4	24.70	0.13
420	96.9	164.6	24.16	0.06
421	169.9	164.7	24.31	0.13
422	108.6	164.8	24.19	0.14
423	135.6	165.0	24.40	0.08
424	153.5	165.1	24.45	0.14
426	79.0	166.0	24.74	0.30
427	67.7	167.2	23.68	0.21
428	206.6	167.3	25.39	0.15
429	203.4	167.8	22.90	0.02
430	53.3	167.9	22.72	0.05
431	139.3	168.0	24.72	0.09
432	159.3	168.0	24.61	0.13
433	147.1	168.4	24.31	0.09
434	163.4	168.6	24.12	0.09
435	31.0	168.6	23.11	0.08
436	237.6	168.6	25.57	0.16
437	185.7	169.0	24.91	0.14

Table 4 - continued

ID#	x (pix)	y (pix)	B	σ_B
438	228.3	169.1	24.88	0.09
439	143.7	169.2	24.35	0.07
440	102.8	169.6	23.64	0.05
441	149.5	169.9	24.64	0.12
442	194.8	170.7	25.32	0.16
443	156.2	171.3	23.66	0.06
444	216.0	172.8	23.12	0.07
445	243.4	173.1	23.92	0.05
446	178.4	174.0	24.51	0.22
447	152.0	174.1	23.67	0.10
448	87.3	174.6	22.57	0.09
449	31.4	174.6	22.25	0.16
450	210.3	174.7	24.95	0.25
451	213.1	175.1	22.33	0.03
452	239.9	177.6	24.70	0.09
453	102.7	177.9	24.87	0.27
454	162.1	178.0	23.64	0.07
455	66.2	178.1	24.82	0.38
456	217.3	178.1	23.55	0.04
458	273.9	178.3	23.25	0.02
460	243.9	178.5	26.15	0.32
461	181.6	178.6	24.67	0.13
462	189.5	179.0	25.02	0.15
463	195.1	179.4	24.25	0.10
464	233.6	180.1	22.20	0.03
465	199.1	180.6	25.51	0.25
466	138.0	181.5	23.79	0.04
467	244.0	181.8	26.75	0.41
469	192.8	182.5	23.72	0.08
470	187.1	182.8	24.47	0.15
473	190.0	182.9	23.61	0.09
474	151.8	183.0	24.67	0.11
475	202.5	183.0	25.07	0.09
476	268.8	184.1	24.52	0.05
477	67.2	184.2	24.39	0.16
479	51.5	185.0	23.52	0.06
480	180.9	185.0	23.94	0.33
481	182.5	185.1	22.19	0.07
483	63.0	186.3	21.83	0.02
484	121.6	186.4	26.00	0.54
485	156.5	186.9	23.93	0.04
486	146.3	187.7	24.26	0.07
487	142.0	187.7	23.83	0.20

Table 4 - continued

ID#	x (pix)	y (pix)	B	σ_B
488	198.0	187.7	25.68	0.23
489	234.6	188.3	26.18	0.28
490	206.1	188.7	23.32	0.03
491	61.0	188.8	24.57	0.16
492	246.3	188.8	23.47	0.03
493	131.3	188.9	25.91	0.34
494	50.4	188.9	22.41	0.04
495	143.3	189.0	22.16	0.05
497	255.6	189.3	24.74	0.10
498	45.8	190.7	22.64	0.05
499	230.7	190.8	25.64	0.14
500	227.9	190.8	22.47	0.01
501	137.1	191.6	25.43	0.27
505	63.3	194.2	22.81	0.05
506	172.6	194.4	25.10	0.11
507	202.8	194.6	25.72	0.19
508	195.3	195.6	23.90	0.04
510	97.8	196.3	25.37	0.46
511	55.9	196.4	23.85	0.18
513	165.0	197.1	23.42	0.03
515	220.8	197.4	25.55	0.15
516	170.5	197.7	24.57	0.06
517	37.3	198.2	22.60	0.12
518	48.6	198.4	24.43	0.17
519	149.3	199.8	23.28	0.01
520	242.2	200.0	26.24	0.19
521	256.3	200.7	25.60	0.13
523	135.7	202.5	25.35	0.17
524	59.3	202.6	23.44	0.06
525	47.0	203.0	21.62	0.02
526	127.2	203.1	25.44	0.26
527	251.9	203.4	26.09	0.25
528	75.6	205.2	22.13	0.02
531	227.5	206.3	24.64	0.09
532	250.7	207.7	21.27	0.01
533	57.8	208.0	23.24	0.06
535	185.7	208.9	25.77	0.12
536	175.4	208.9	23.91	0.03
539	74.6	210.6	25.38	0.43
540	249.6	210.7	23.99	0.03
541	43.4	211.1	23.05	0.05
542	152.4	211.4	26.12	0.28
543	184.1	212.1	25.76	0.15

Table 4 - continued

ID#	x (pix)	y (pix)	B	σ_B
545	64.6	212.7	23.83	0.06
546	79.7	213.1	22.42	0.03
547	170.1	214.2	24.57	0.05
548	133.0	215.0	24.10	0.07
549	254.4	215.8	24.09	0.03
550	166.7	215.8	26.08	0.42
551	142.4	215.9	22.26	0.01
552	45.6	216.0	22.87	0.05
553	203.8	216.0	22.47	0.01
555	234.1	216.3	25.82	0.18
556	161.3	217.4	24.02	0.03
557	94.8	217.7	22.43	0.02
558	65.2	217.9	23.51	0.03
559	184.4	218.2	22.87	0.02
560	167.0	218.3	22.52	0.02
561	186.9	218.7	26.10	0.33
562	40.5	219.0	24.05	0.08
564	190.6	219.6	25.96	0.26
565	29.6	220.1	21.80	0.04
566	222.6	220.1	24.22	0.05
568	113.0	220.7	23.52	0.04
569	27.8	222.0	23.86	0.17
570	179.9	222.1	23.52	0.04
571	191.5	222.3	24.50	0.07
573	196.4	222.6	24.69	0.13
574	138.5	222.6	26.36	0.54
575	36.3	222.9	23.33	0.07
576	224.9	222.9	25.36	0.16
577	198.7	223.0	25.00	0.16
579	94.5	223.7	23.46	0.05
580	42.2	223.8	24.69	0.18
581	219.3	224.0	24.39	0.08
582	251.4	224.3	23.65	0.03
583	178.7	224.4	24.79	0.14
586	164.8	226.5	23.15	0.04
588	35.0	227.0	24.03	0.43
590	33.1	227.4	23.71	0.26
591	68.6	227.8	22.15	0.03
593	43.4	229.9	22.64	0.04
594	3.5	230.1	22.81	0.06
595	219.8	230.2	24.51	0.13
597	139.2	231.4	24.77	0.15
598	31.7	231.8	24.31	0.12

Table 4 - continued

ID#	x (pix)	y (pix)	B	σ_B
599	216.5	232.6	23.77	0.04
600	93.8	233.7	22.89	0.02
601	205.4	233.7	26.02	0.14
602	128.9	233.8	24.35	0.50
603	246.1	234.3	25.98	0.15
604	149.5	234.4	24.85	0.12
605	130.5	234.5	21.20	0.03
606	43.6	234.5	22.87	0.05
607	155.0	235.0	24.66	0.08
608	78.2	235.7	23.26	0.07
609	200.5	236.9	23.54	0.02
610	147.8	237.6	26.25	0.36
611	30.1	238.6	21.95	0.02
612	167.6	238.8	23.32	0.03
613	66.9	239.1	23.68	0.08
614	254.1	239.7	24.51	0.05
615	222.0	239.8	23.58	0.04
616	181.0	240.3	24.63	0.13
617	114.6	240.3	22.52	0.03
618	220.3	241.8	22.52	0.02
619	159.6	241.8	24.07	0.06
620	234.5	242.8	26.46	0.38
621	17.8	243.5	24.73	0.15
622	109.3	244.4	23.28	0.06
623	115.2	244.7	25.73	0.39
624	226.6	244.8	25.53	0.20
625	27.2	245.7	20.65	0.01
626	181.5	245.7	23.33	0.08
627	132.1	246.9	26.01	0.37
628	240.0	247.9	25.52	0.16
629	228.2	248.3	25.42	0.12
630	154.3	248.4	26.22	0.37
631	109.6	248.6	24.24	0.10
632	122.9	248.9	25.45	0.24
633	194.4	249.2	25.27	0.16
634	185.3	249.4	24.93	0.12
635	29.0	249.7	22.64	0.04
636	69.4	249.8	23.44	0.09
637	143.8	249.8	24.12	0.03
638	203.0	250.3	24.25	0.04
639	179.8	250.6	24.00	0.11
640	135.3	250.7	24.70	0.09
641	24.8	250.9	24.00	0.10

Table 4 - continued

ID#	x (pix)	y (pix)	B	σ_B
642	151.0	250.9	25.03	0.11
643	249.0	251.5	25.80	0.33
644	98.1	252.4	24.34	0.12
645	146.6	252.8	25.49	0.15
646	101.1	252.8	22.43	0.11
647	210.7	253.9	24.95	0.10
648	204.2	254.0	25.05	0.12
649	122.3	254.2	24.30	0.08
650	187.5	254.7	23.42	0.02
651	153.1	255.2	24.39	0.05
652	159.0	255.5	22.43	0.01
653	190.6	255.8	24.07	0.05
654	12.0	256.5	23.55	0.06
655	137.9	256.7	24.99	0.08
656	98.0	256.9	24.00	0.07
657	67.8	257.2	23.52	0.03
658	117.4	257.7	22.88	0.02
659	188.2	258.5	24.59	0.07
660	181.4	259.7	24.80	0.12
661	228.5	259.8	26.37	0.44
662	16.2	259.8	25.78	0.35
663	40.8	260.0	23.27	0.13
664	211.9	260.7	25.23	0.21
665	104.3	260.9	23.16	0.03
666	184.8	261.0	25.15	0.12
667	55.4	261.0	22.18	0.03
668	245.8	262.2	24.03	0.03
669	225.0	262.2	26.19	0.48
670	17.0	262.7	22.65	0.02
671	158.9	263.2	24.73	0.06
672	152.0	263.7	26.07	0.30
673	3.5	263.7	23.76	0.05
674	164.5	263.8	22.73	0.01
675	214.7	264.5	21.16	0.02
676	243.4	264.7	25.20	0.09
677	170.1	265.0	22.52	0.01
678	173.4	266.2	23.67	0.02
679	157.1	267.3	25.22	0.09
680	250.4	268.3	24.92	0.06
681	97.3	268.8	24.27	0.31
682	135.7	269.9	24.00	0.05
683	44.6	270.0	24.45	0.09
684	83.3	270.4	22.98	0.04

Table 4 - continued

ID#	x (pix)	y (pix)	B	σ_B
685	178.6	270.5	26.22	0.28
686	256.0	270.7	23.91	0.04
687	65.9	270.8	22.94	0.04
688	101.0	270.9	22.67	0.05
689	56.9	271.0	24.90	0.27
690	98.7	271.1	24.07	0.18
691	232.3	271.3	25.86	0.18
692	208.9	271.8	26.87	0.52
693	236.6	271.8	22.25	0.01
694	49.6	271.9	25.73	0.40
695	117.2	271.9	23.32	0.03
696	169.7	272.0	25.98	0.17
697	197.3	272.1	25.70	0.18
698	75.4	272.4	25.74	0.46
699	173.9	272.7	22.47	0.01
700	41.8	272.8	23.19	0.03
701	68.0	273.5	24.58	0.10
702	14.1	274.0	24.58	0.11
703	245.8	274.3	24.78	0.07
704	140.1	274.3	24.79	0.11
705	267.2	274.3	25.47	0.15
706	119.6	275.5	21.07	0.01
707	261.7	275.5	23.68	0.03
708	105.2	276.5	25.27	0.12
709	143.7	276.9	25.41	0.15
710	127.9	277.0	23.55	0.05
711	10.9	277.2	22.68	0.03
712	28.8	278.0	23.49	0.04
713	234.8	278.4	25.63	0.13
714	94.3	278.5	22.57	0.03
715	50.2	279.0	23.48	0.05
716	261.5	279.4	24.48	0.05
717	75.9	279.8	23.81	0.04
718	179.1	279.9	22.64	0.05
719	58.9	280.0	24.07	0.07
720	46.0	280.0	20.63	0.01
721	177.7	280.7	23.74	0.14
722	151.2	281.0	22.35	0.01
723	39.4	281.3	23.80	0.05
724	18.1	281.7	21.62	0.02
725	231.0	282.3	23.46	0.02
726	119.7	283.1	25.72	0.21
727	129.3	283.2	25.44	0.33

Table 4 - continued

ID#	x (pix)	y (pix)	B	σ_B
728	90.4	284.0	24.88	0.12
729	258.1	284.3	24.89	0.08
730	99.8	284.7	25.42	0.17
731	153.1	285.2	22.21	0.03
732	249.8	285.5	23.43	0.02
733	96.4	285.6	23.93	0.05
734	48.5	286.2	24.82	0.15
735	74.7	286.2	24.29	0.06
736	121.9	286.8	25.22	0.18
737	115.4	287.5	25.43	0.13
738	220.6	288.0	22.36	0.01
739	273.4	288.1	22.61	0.01
740	216.7	288.5	24.99	0.10
741	121.0	290.0	25.54	0.24
742	149.5	290.1	24.02	0.05
743	247.1	290.3	24.41	0.04
744	2.4	290.4	24.82	0.12
745	166.8	290.4	22.35	0.01
746	153.8	290.5	23.97	0.03
747	181.5	290.6	24.90	0.07
748	6.8	290.8	23.04	0.03
749	213.0	291.9	24.12	0.05
750	75.9	292.1	23.84	0.05
751	24.1	293.5	23.11	0.05
752	61.9	294.7	23.43	0.04
753	160.1	295.0	23.51	0.02
754	68.6	295.1	23.51	0.04
755	21.1	295.7	23.78	0.06
756	219.0	295.7	23.55	0.03
757	112.9	296.3	26.24	0.43
758	103.0	296.5	22.53	0.02
759	170.2	296.6	26.44	0.34
760	98.4	296.8	22.46	0.02
761	82.9	298.1	23.74	0.05
762	7.7	298.3	25.31	0.20
763	204.7	298.5	24.97	0.08
764	136.1	299.4	24.08	0.10
765	162.9	299.9	23.88	0.03
766	146.3	300.1	20.57	0.00
767	3.0	300.2	22.33	0.01
768	154.8	300.6	23.77	0.04
769	220.9	301.5	23.95	0.03
770	200.6	302.2	22.00	0.01

Table 4 - continued

ID#	x (pix)	y (pix)	B	σ_B
771	167.7	302.7	26.72	0.36
772	256.8	302.7	24.54	0.08
773	105.7	302.8	26.14	0.34
774	231.6	302.9	24.40	0.06
775	20.5	302.9	22.40	0.03
776	262.5	304.3	21.66	0.01
777	57.8	304.3	23.81	0.05
778	244.6	304.4	23.09	0.04
779	158.7	304.8	24.73	0.18
780	41.5	305.0	24.04	0.07
781	248.2	305.7	25.56	0.16
782	231.8	305.9	25.50	0.13
783	160.3	306.3	22.68	0.02
784	245.2	306.5	23.32	0.06
785	152.4	306.7	25.07	0.13
786	106.8	307.1	22.07	0.01
787	112.8	307.2	25.45	0.16
788	220.4	307.6	25.18	0.08
789	205.2	308.3	25.07	0.08
790	179.3	309.0	24.26	0.08
791	85.4	310.1	22.64	0.02
792	147.8	310.1	25.02	0.14
793	20.3	310.2	22.71	0.03
794	27.8	310.9	23.63	0.05
795	115.1	310.9	22.54	0.01
796	159.3	311.2	25.84	0.17
797	18.6	312.3	21.52	0.01
798	189.2	312.5	24.39	0.05
799	138.3	312.6	26.33	0.25
800	108.0	313.0	25.05	0.12
801	97.5	313.2	23.90	0.05
802	240.3	313.3	24.91	0.10
803	232.0	313.3	25.95	0.16
804	227.1	313.7	23.10	0.02
805	73.7	314.1	23.56	0.08
806	54.3	314.5	24.15	0.06
807	163.9	315.0	23.70	0.04
808	187.0	315.4	25.51	0.14
809	218.3	315.8	22.00	0.03
810	91.5	316.0	24.40	0.08
811	100.9	316.4	24.83	0.11
812	105.1	316.4	22.98	0.02
813	9.1	316.5	22.18	0.30

Table 4 - continued

ID#	x (pix)	y (pix)	B	σ_B
814	27.2	316.8	24.02	0.06
815	166.6	316.9	24.03	0.08
816	132.0	317.3	24.05	0.04
817	79.6	317.4	23.04	0.04
818	84.3	318.3	24.82	0.10
819	159.9	318.4	26.44	0.28
820	216.6	319.6	25.30	0.14
821	34.2	320.1	23.64	0.03
822	62.3	321.0	24.05	0.06
823	122.9	321.1	23.44	0.03
824	266.3	321.4	24.23	0.03
825	261.0	321.4	25.02	0.07
826	168.6	322.4	25.37	0.14
827	106.9	322.8	24.51	0.11
828	16.6	322.8	24.48	0.08
829	118.0	323.8	20.36	0.01
830	131.9	323.9	25.03	0.17
831	62.2	325.0	25.80	0.19
832	23.4	325.2	25.70	0.20
833	91.6	325.3	24.87	0.13
834	9.3	325.6	25.04	0.15
835	268.2	326.0	23.28	0.02
836	29.6	326.2	24.51	0.08
837	200.7	326.6	25.72	0.14
838	229.4	326.7	24.97	0.07
839	97.7	327.0	24.19	0.07
840	136.1	327.5	24.44	0.05
841	232.3	327.6	25.78	0.16
842	53.1	327.7	23.00	0.02
843	38.1	328.3	22.06	0.02
844	242.9	328.4	21.35	0.01
845	107.0	328.6	24.75	0.12
846	165.5	329.6	26.78	0.49
847	28.0	330.2	22.37	0.01
848	98.2	330.8	23.59	0.05
849	143.7	331.0	26.03	0.24
850	43.9	331.4	23.75	0.04
851	152.1	331.7	24.07	0.03
852	15.9	332.0	24.02	0.06
853	103.9	333.0	23.27	0.03
854	107.5	333.3	24.69	0.10
855	244.5	333.3	25.87	0.20
856	25.8	333.5	24.59	0.08

Table 4 - continued

ID#	x (pix)	y (pix)	B	σ_B
857	64.2	333.7	26.14	0.35
858	32.2	334.4	25.14	0.12
859	142.9	334.5	24.43	0.05
860	224.9	335.3	24.37	0.05
861	79.3	335.7	26.31	0.30
862	207.0	335.9	24.07	0.20
863	204.9	336.0	21.74	0.04
864	109.7	336.1	23.74	0.05
865	260.9	336.1	26.17	0.16
866	128.9	336.2	26.76	0.43
867	73.4	336.9	22.51	0.02
868	151.0	337.1	25.71	0.18
869	37.6	337.3	24.98	0.11
870	51.5	337.8	25.67	0.20
871	31.2	338.6	24.44	0.08
872	243.5	339.1	23.83	0.03
873	149.0	339.2	26.12	0.24
874	110.9	339.8	24.80	0.13
875	18.1	340.6	24.58	0.08
876	102.5	340.7	23.81	0.06
877	187.8	341.2	26.32	0.26
878	74.5	341.3	24.87	0.32
879	14.3	342.0	25.96	0.26
880	84.5	342.3	25.14	0.09
881	88.9	342.5	23.82	0.11
882	178.6	342.5	25.88	0.15
883	37.2	342.6	25.15	0.14
884	130.5	342.6	26.36	0.36
885	73.3	343.0	22.30	0.03
886	105.5	343.2	24.58	0.10
887	90.7	343.3	24.55	0.22
888	66.7	343.4	24.66	0.06
889	154.0	343.5	23.80	0.03
890	189.8	344.4	23.82	0.02
891	108.8	344.4	24.52	0.11
892	17.8	344.8	23.93	0.04
893	99.1	344.9	24.47	0.10
894	250.6	345.2	25.44	0.11
895	86.2	345.7	24.56	0.05
896	46.2	345.8	26.31	0.21
897	13.6	346.2	24.17	0.05
898	64.0	346.3	24.79	0.08
899	127.1	346.5	24.41	0.05

Table 4 - continued

ID#	x (pix)	y (pix)	B	σ_B
900	123.3	347.0	25.40	0.15
901	89.3	347.4	25.63	0.19
902	7.7	347.7	24.63	0.08
903	110.6	348.1	24.88	0.11
904	86.4	349.0	23.62	0.03
905	196.3	349.7	24.31	0.04
906	98.4	349.9	24.55	0.13
907	209.4	350.1	25.42	0.20
908	187.7	350.7	23.65	0.03
909	35.2	350.8	25.00	0.12
910	106.5	351.2	23.99	0.10
911	18.0	351.7	22.02	0.03
912	4.7	351.9	24.74	0.16
913	53.5	352.6	23.21	0.02
914	151.1	352.9	24.75	0.06
915	156.8	352.9	21.82	0.01
916	48.2	353.1	26.05	0.25
917	187.9	353.9	22.90	0.01
918	106.1	354.0	24.09	0.11
919	211.4	354.5	25.62	0.15
920	33.8	354.9	24.42	0.08
921	90.2	354.9	24.88	0.09
922	205.6	355.1	23.91	0.03
923	208.6	355.1	26.33	0.29
924	266.0	355.5	23.12	0.02
925	219.6	356.5	25.12	0.29
926	15.0	356.6	24.74	0.15
927	217.5	357.1	25.91	0.31
928	89.4	357.6	23.70	0.08
929	91.5	357.7	24.80	0.21
930	220.8	358.1	25.27	0.33
931	100.6	358.1	24.51	0.14
932	67.9	358.6	26.73	0.43
933	119.7	359.3	24.13	0.07
934	254.1	359.5	26.83	0.38
935	95.3	361.1	25.78	0.12
936	75.8	361.3	25.18	0.09
937	89.9	361.4	25.65	0.13
938	98.5	363.8	25.72	0.17
939	225.4	363.9	23.92	0.03
940	214.4	364.2	26.64	0.36
941	83.4	364.3	26.07	0.21
942	74.4	364.6	26.65	0.41

Table 4 - continued

ID#	x (pix)	y (pix)	B	σ_B
943	20.5	364.9	23.06	0.02
944	95.3	365.5	25.67	0.15
945	28.3	366.0	25.76	0.17
946	47.4	366.1	23.66	0.03
947	102.3	366.3	24.44	0.04
948	127.4	366.6	24.42	0.06
949	206.8	366.7	26.43	0.26
950	180.4	366.8	25.86	0.15
951	212.1	367.8	24.90	0.11
952	12.1	368.1	24.14	0.08
953	108.6	368.2	22.82	0.02
954	166.9	368.9	22.88	0.05
955	18.5	368.9	23.33	0.02
956	210.1	369.2	24.61	0.10
957	1.1	369.4	23.59	0.07
958	186.3	369.6	25.84	0.13
959	132.5	369.7	25.25	0.13
960	203.3	369.8	26.13	0.21
961	129.3	370.3	21.61	0.01
962	200.2	370.3	23.24	0.02
963	13.2	371.2	24.34	0.07
964	85.7	371.8	23.96	0.03
965	97.2	372.0	25.00	0.30
966	139.2	372.1	22.62	0.01
967	166.3	372.5	24.32	0.04
968	37.2	373.0	25.68	0.13
969	27.0	373.1	24.46	0.06
970	210.8	373.3	26.56	0.49
971	4.8	373.4	24.98	0.11
972	15.1	373.5	24.99	0.11
973	20.8	373.6	25.61	0.13
974	97.0	373.8	25.35	0.43
975	184.7	374.2	26.56	0.36
976	84.7	374.8	26.44	0.31
977	91.1	375.1	25.54	0.26
978	93.3	375.5	25.25	0.21
979	150.4	375.6	26.17	0.31
980	11.1	375.6	24.98	0.07
981	121.6	376.0	25.91	0.14
982	52.4	376.2	25.66	0.16
983	116.7	376.5	22.79	0.03
984	173.0	376.6	24.60	0.06
985	19.6	377.0	26.18	0.24

Table 4 - continued

ID#	x (pix)	y (pix)	B	σ_B
986	166.1	377.5	24.90	0.08
987	2.1	377.6	23.99	0.05
988	41.7	378.2	22.44	0.01
989	86.2	378.8	26.16	0.35
990	111.5	379.0	24.53	0.08
991	128.1	379.0	24.88	0.10
992	14.7	379.5	25.51	0.14
993	65.8	379.6	23.56	0.02
994	8.4	379.7	22.95	0.03
995	17.8	380.0	26.08	0.18
996	95.1	380.1	26.24	0.28
997	125.3	380.1	26.16	0.29
998	24.3	380.3	25.85	0.20
999	185.1	380.8	25.26	0.12
1000	187.9	381.3	22.77	0.02
1001	198.1	381.4	26.69	0.31
1002	33.0	381.8	24.66	0.06
1003	48.2	381.9	26.71	0.40
1004	100.3	383.3	25.41	0.13
1005	2.1	383.5	24.91	0.12
1006	69.4	383.7	24.33	0.05
1007	9.2	383.7	25.22	0.12
1008	255.6	384.5	25.19	0.09
1009	62.9	384.6	25.98	0.17
1010	92.6	385.1	24.85	0.08
1011	97.7	385.5	25.85	0.19
1012	135.3	386.1	23.37	0.03
1013	121.3	386.5	25.68	0.16
1014	68.3	386.7	22.47	0.01
1015	12.8	386.9	25.67	0.14
1016	41.4	387.9	23.50	0.03
1017	132.2	388.0	26.68	0.50
1018	96.2	388.1	26.44	0.23
1019	221.7	388.5	21.68	0.00
1020	233.1	388.6	24.31	0.05
1021	10.2	389.1	25.07	0.09
1022	17.8	389.2	26.43	0.35
1023	270.5	389.2	26.71	0.34
1024	157.7	389.3	24.41	0.05
1025	105.7	389.4	25.64	0.15
1026	188.9	390.4	25.49	0.13
1027	27.1	391.2	25.41	0.11
1028	199.5	391.3	23.07	0.02

Table 4 - continued

ID#	x (pix)	y (pix)	B	σ_B
1029	244.8	391.6	24.48	0.04
1030	41.1	391.8	23.60	0.03
1031	75.5	393.1	25.56	0.31
1032	176.6	393.7	26.56	0.28
1033	261.6	393.7	22.68	0.01
1034	121.2	394.1	26.87	0.47
1035	188.2	394.3	25.87	0.17
1036	19.8	394.6	24.79	0.12
1037	3.8	395.0	23.69	0.05
1038	171.0	395.2	25.32	0.09
1039	195.2	395.7	24.17	0.04
1040	159.0	395.9	22.96	0.01
1041	71.1	396.0	24.10	0.18
1042	114.4	396.0	24.72	0.10
1043	69.3	396.2	24.71	0.26
1044	250.3	396.6	24.51	0.05
1045	209.2	397.6	26.28	0.22
1046	144.8	397.6	23.38	0.02
1047	110.6	397.7	23.66	0.04
1048	236.0	398.5	24.00	0.05
1049	192.3	398.8	24.17	0.04
1050	67.8	399.0	26.45	0.34
1051	38.3	400.1	25.48	0.16
1052	143.8	401.1	25.58	0.12
1053	17.0	401.6	26.16	0.25
1054	118.1	403.2	24.83	0.07
1055	90.9	403.2	26.50	0.23
1056	237.2	405.1	23.00	0.02
1057	160.0	405.4	24.87	0.06
1058	240.3	406.2	21.20	0.01
1059	271.8	406.3	25.74	0.15
1060	15.4	406.8	25.53	0.16
1061	266.8	407.1	25.99	0.17
1062	90.5	407.4	26.64	0.36
1063	23.8	407.8	22.94	0.03
1064	240.9	407.8	24.69	0.32
1065	122.4	408.3	26.62	0.33
1066	212.4	409.1	25.07	0.10
1067	99.2	409.6	26.17	0.25
1068	130.3	410.1	24.62	0.05
1069	3.3	410.9	25.38	0.12
1070	39.0	411.8	22.93	0.02
1071	42.8	412.0	24.28	0.05

Table 4 - continued

ID#	x (pix)	y (pix)	B	σ_B
1072	180.6	412.5	25.83	0.12
1073	214.3	413.7	25.94	0.29
1074	241.9	413.8	26.03	0.28
1075	216.6	414.4	23.90	0.04
1076	68.6	416.4	25.96	0.18
1077	109.0	416.9	24.26	0.05
1078	4.5	417.0	26.00	0.19
1079	167.0	417.2	26.22	0.19
1080	22.2	417.5	25.55	0.10
1081	197.0	418.5	21.68	0.01
1082	128.6	419.6	23.69	0.03
1083	68.2	420.3	24.96	0.09
1084	150.8	420.5	23.02	0.02
1085	113.1	420.5	23.12	0.01
1086	117.3	420.6	21.64	0.00
1087	178.0	421.1	24.80	0.07
1088	74.5	421.2	26.09	0.22
1089	212.9	422.0	25.49	0.11
1090	99.4	422.4	24.69	0.09
1091	128.5	423.7	23.48	0.03
1092	109.0	424.6	25.12	0.07
1093	13.5	425.5	24.72	0.08
1094	82.7	426.0	24.97	0.10
1095	39.7	426.4	23.33	0.04
1096	53.1	427.5	21.95	0.01
1097	217.2	427.6	23.11	0.04
1098	104.2	428.5	21.73	0.01
1099	215.8	429.1	24.71	0.14
1100	267.7	431.9	24.42	0.14
1101	256.1	432.1	25.48	0.12
1102	111.2	432.2	26.48	0.30
1103	260.8	432.3	25.09	0.12
1104	251.8	432.3	25.27	0.10
1105	239.9	432.5	22.15	0.01
1106	152.2	433.0	24.98	0.09
1107	61.6	434.1	22.12	0.02
1108	96.6	434.2	24.71	0.14
1109	264.0	434.3	23.37	0.02
1110	244.6	434.4	26.14	0.18
1111	76.1	434.4	24.26	0.08
1113	25.6	434.5	24.11	0.08
1114	150.0	434.6	24.86	0.08
1115	37.5	434.8	22.85	0.09

Table 4 - continued

ID#	x (pix)	y (pix)	B	σ_B
1116	172.9	435.3	26.43	0.40
1117	147.4	435.5	25.00	0.12
1118	13.5	436.2	22.78	0.03
1119	193.8	436.6	23.04	0.01
1122	131.6	438.2	23.53	0.02
1123	162.8	439.8	25.74	0.14
1124	225.8	439.8	20.93	0.01
1125	262.5	440.2	22.73	0.01
1126	190.5	441.1	24.58	0.06
1127	258.9	441.3	25.88	0.19
1128	139.4	441.6	25.57	0.13
1129	115.6	443.5	24.23	0.04
1130	250.7	444.0	26.57	0.28
1131	136.4	444.6	24.99	0.08
1132	66.3	445.7	22.15	0.01
1133	32.3	445.8	24.82	0.13
1134	74.8	446.2	22.38	0.01
1135	187.4	446.8	26.13	0.19
1136	264.7	447.0	25.79	0.13
1137	231.9	447.4	25.83	0.14
1138	161.2	447.5	25.11	0.06
1139	2.5	447.6	23.87	0.03
1140	226.1	448.4	25.56	0.14
1141	96.2	448.9	25.71	0.22
1142	135.9	450.7	23.54	0.02
1143	261.5	450.7	25.74	0.11
1144	75.8	450.9	23.42	0.04
1145	256.6	451.0	25.80	0.18
1146	49.0	451.5	25.64	0.17
1147	248.9	452.5	24.40	0.05
1148	271.2	453.3	23.86	0.04
1149	220.2	453.7	25.53	0.10
1150	242.0	453.7	26.08	0.24
1151	114.4	453.9	21.30	0.01
1152	139.2	454.5	25.48	0.10
1153	135.5	455.1	24.58	0.05
1154	98.9	455.3	25.65	0.13
1155	238.5	455.5	26.06	0.16
1156	131.3	455.8	22.89	0.01
1157	62.3	456.7	26.27	0.26
1158	105.1	456.7	25.64	0.14
1159	242.3	457.1	25.79	0.13
1160	135.6	458.1	25.51	0.14

Table 4 - continued

ID#	x (pix)	y (pix)	B	σ_B
1161	199.1	458.1	26.03	0.18
1162	6.7	458.1	24.88	0.08
1163	186.7	459.7	25.37	0.13
1164	250.5	460.0	25.38	0.15
1165	114.4	460.1	25.29	0.09
1166	245.0	461.1	25.45	0.13
1167	39.2	462.7	25.96	0.23
1168	209.4	462.9	25.76	0.10
1169	195.6	462.9	23.18	0.05
1170	95.2	463.2	25.05	0.07
1171	130.7	463.2	25.30	0.19
1172	190.0	463.4	25.85	0.14

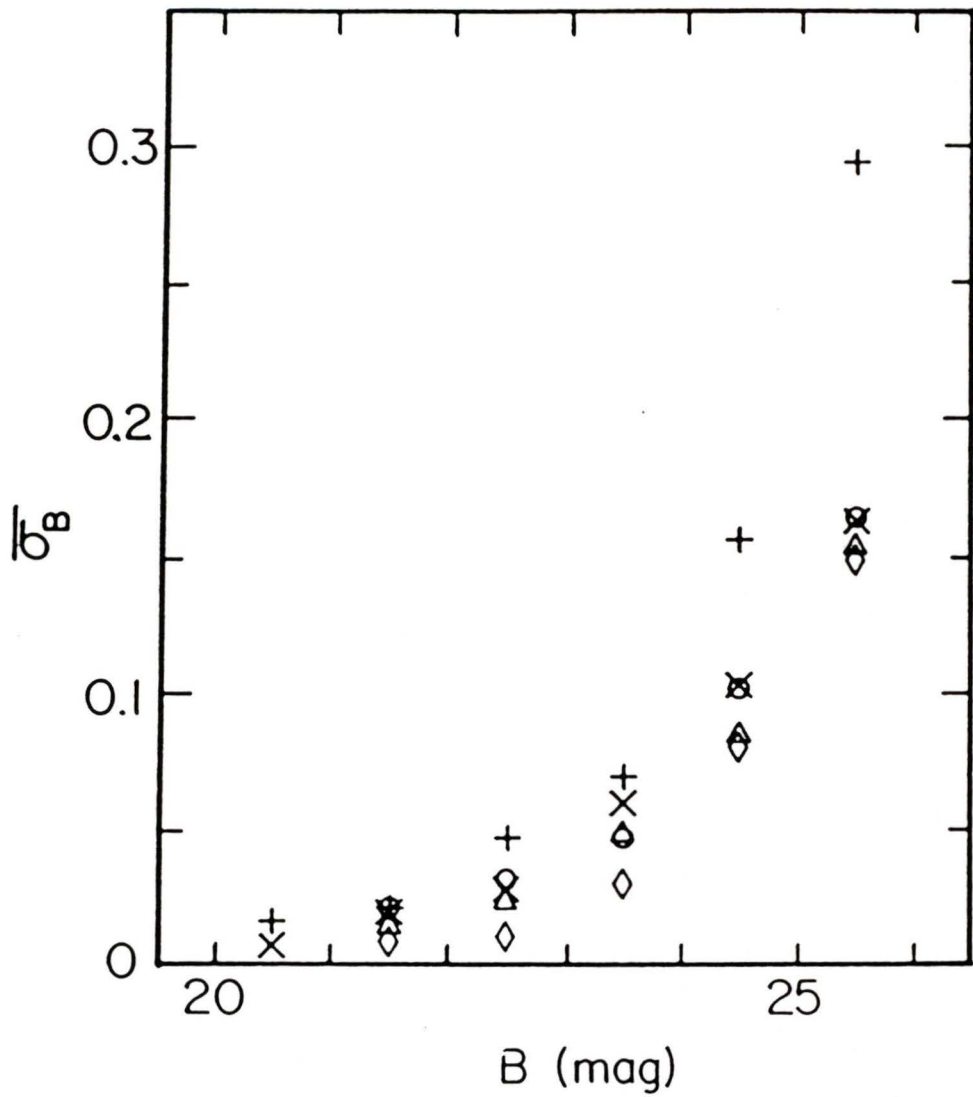


Figure 2. Mean computed magnitude errors as a function of magnitude and projected galactocentric radius. The points represent radial zones defined as follows; '+'s - 20 + 55 arcseconds, 'x's - 56 + 75 arcseconds, circles - 76 + 93 arcseconds, triangles - 94 + 109 arcseconds, diamonds - 110 + 159 arcseconds.

Table 5

Objects Common to Present Sample and that of Strom et al. (1981)

ID# (Strom et al.)	ID# (Table 4)	B (Strom et al.)	B (Table 4)
25	816	22.31	22.97
42	750	21.40	21.29
64	714	21.43	21.41
69	645	20.77	20.78
79	698	23.81	23.40
98	747	23.62	23.73
102	585	23.04	23.01
132	695	21.74	21.80
144	591	22.26	22.22
169	640	22.14	22.08
194	577	23.03	23.33
211	590	22.67	22.56
212	641	23.14	22.97
220	697	21.42	21.28
257	676	22.62	22.27
264	593	22.74	22.83
267	648	23.68	23.39
306	688	22.79	22.56
317	666	22.84	22.68
331	637	22.73	22.98
339	583	23.07	23.35
353	649	20.89	21.18
366	622	21.98	22.19
384	717	22.59	22.85
409	621	23.12	23.09
451	643	21.88	22.33
464	627	22.57	22.20
492	616	23.52	23.47
500	633	22.84	22.47
532	612	21.26	21.27
553	662	22.79	22.47
559	691	23.31	22.87
618	646	22.36	22.52
650	693	23.18	23.42

Table 5 - continued

ID# (Strom et al.)	ID# (Table 4)	B (Strom et al.)	B (Table 4)
675	654	21.17	21.16
693	634	22.60	22.25
707	604	23.72	23.68
718	707	22.56	22.64
732	623	23.45	23.43
738	652	22.47	22.36
739	595	22.86	22.61
766	746	20.72	20.57
770	683	21.99	22.00
776	610	21.76	21.66
778	630	22.69	23.09
809	661	22.09	22.00
829	772	20.41	20.36
835	605	23.68	23.28
843	857	22.17	22.06
844	635	21.45	21.35
863	680	21.86	21.74
885	827	22.09	22.30
904	813	23.01	23.62
911	876	22.15	22.02
915	742	21.94	21.82
917	705	22.78	22.90
924	615	23.62	23.12
953	791	23.25	22.82
954	734	23.11	22.88
961	770	21.78	21.61
962	696	23.70	23.24
988	858	22.93	22.44
994	888	23.32	22.95
1000	710	23.36	22.77
1014	836	22.59	22.47
1019	667	21.77	21.68
1033	624	23.11	22.68
1040	744	23.13	22.96
1058	647	21.04	21.20
1063	877	23.27	22.94
1070	864	22.89	22.93
1081	703	21.80	21.68

Table 5 - continued

ID# (Strom et al.)	ID# (Table 4)	B (Strom et al.)	B (Table 4)
1084	759	23.43	23.02
1086	789	21.54	21.64
1091	774	23.08	23.48
1096	853	21.98	21.95
1097	677	22.80	23.11
1098	807	21.80	21.73
1105	650	22.24	22.15
1107	851	22.45	22.12
1109	625	23.12	23.37
1115	869	19.57	22.85
1118	890	23.18	22.78
1119	713	23.30	23.04
1124	670	20.91	20.93
1125	629	23.00	22.73
1134	837	22.29	22.38
1151	800	21.44	21.30
1169	711	22.90	23.18

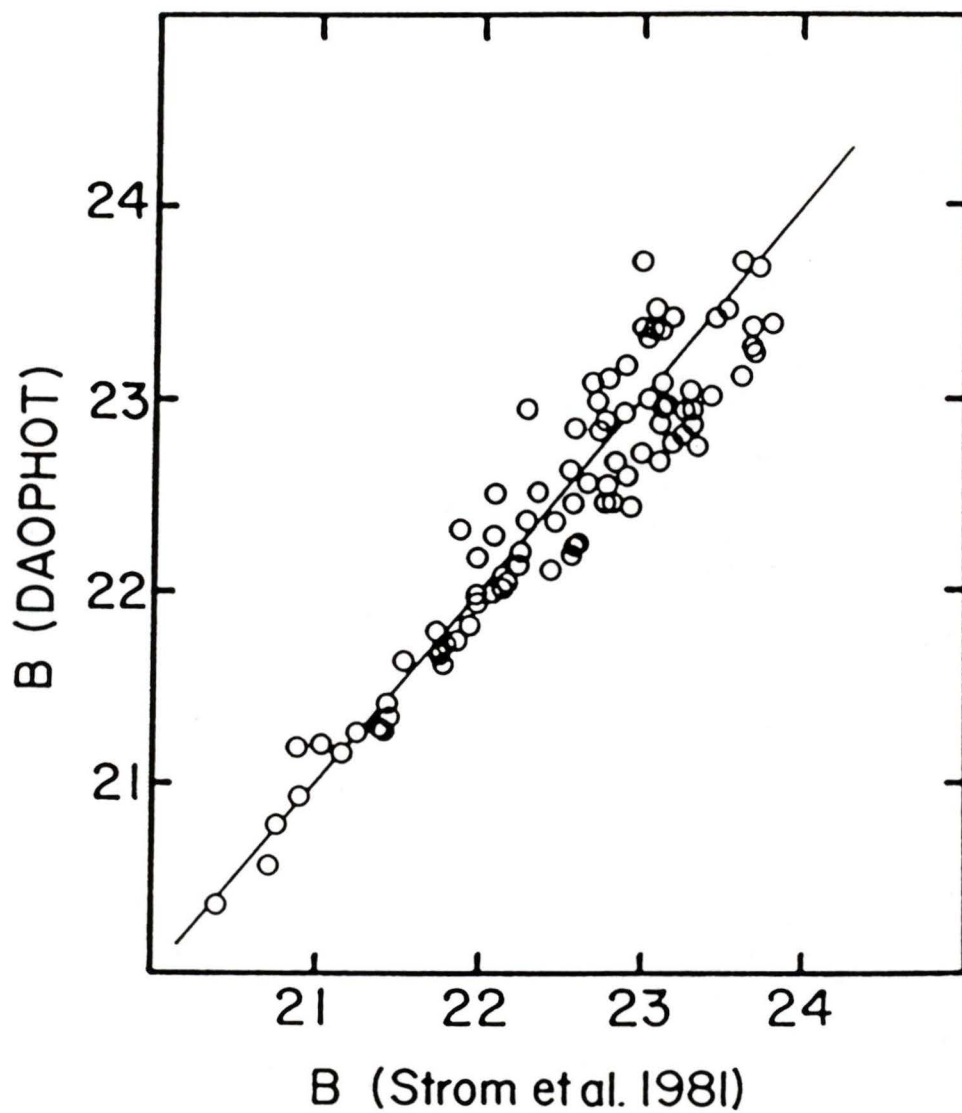


Figure 3. Comparison of transformed B magnitudes computed using DAOPHOT with those determined by Strom et al. (1981). The 93 objects common to both samples are listed in Table 5.

CHAPTER 3

THE GLOBULAR CLUSTER LUMINOSITY FUNCTION

The object list given in Table 4 was not suitable for determining a globular cluster luminosity function because: a) some unknown fraction of these objects actually corresponded to foreground stars or background galaxies rather than globular clusters associated with the halo of M87; and b) no attempt had yet been made in the reductions to quantify the finding (and retaining) efficiency of the DAOPHOT photometry procedures at various magnitude levels.

3.1 Completeness Corrections

With reference to b) above, the problem was dealt with stochastically by rerunning the entire photometry sequence many times on image frames containing, in addition to the original data, a known number of artificially generated objects of specified magnitudes. Use was made of the DAOPHOT ADD* routine, which would generate PSF's, scaled as required by a user-specified range of magnitudes, and distribute these randomly about an input data frame. Rerunning of the

photometry procedure outlined in the previous chapter then resulted in an object list which could be compared with a list of the positions and magnitudes of the generated images to determine how many of the added images had been missed.

In addition to being time-consuming, however, this procedure was only an approximate method for determining the completeness of the object list since: a) the generated images were scaled PSF's as opposed to real data, so that their cores would be less noisy and more easily fitted by NSTAR; and b) in order to get the best possible completeness fraction in this manner, a large number of frames would have to be generated and subsequently reduced. Regarding point a), the problem was not serious since most the images were faint enough that the noise was completely dominated by the subtracted halo and sky background. With reference to point b), the completeness fractions eventually arrived at were found to be consistent enough from run to run so that the probable errors introduced into the results by this scatter were well within the Poisson counting statistics.

A typical completeness-test run was initiated by adding one hundred "stars" to each of three frames containing the original background-subtracted data. It was decided that one hundred added objects per frame represented a reasonable compromise between allowing the tests to proceed at an efficient rate and not significantly affecting the finding and fitting routines by overly crowding the field. The magnitude range of these objects was set to be fairly narrow for a given set of three frames (for example, $24.0 < B < 24.1$,

24.5 < B < 24.6, etc) in order not to complicate unnecessarily the process of matching added objects to the final output object lists. The photometry procedure was then run on each frame individually with exactly the same finding and fitting parameters as were described in Chapter 2. In order to speed up reductions considerably, the natural group files produced for each frame were examined to weed out those groups which did not overlap the coordinates of any objects which had been added. In addition, any groups which did not extend beyond fifty arcseconds from the apparent center of M87 were also dropped from further consideration. Due to the rapid rise in the photon noise contributed by M87's stellar component and, to a lesser extent, the increased crowding of images, the completenesses determined within this radius were less than 50% for the faintest magnitudes presently considered. Finally, as in Chapter 2, each remaining group was subjected to no less than two runs of NSTAR.

When an object list for a given artificial frame was in hand, a simple FORTRAN code was used to compare the coordinates and magnitudes given in the list of added objects with similar values in the new NSTAR output list. A positional tolerance of one pixel (0.41 arcseconds) was specified for all runs, and if the magnitude of an object within the required region was found to be more than one magnitude away from the input magnitude of the added objects, the object was considered to have been "lost". In all instances, the reduced object list was also compared with the object list determined in Chapter 2 to ensure that there were indeed more objects in the

search region than there had been originally.

The fact that on many occasions the final number of objects was found to be equal to (or less than) the original number, however, did not always preclude the possible recovery of the added object. For example, if a 23rd magnitude object had been placed on top of what was originally a 25th magnitude object, then the intensity of the combined image would still be within tolerance range of the input magnitude. Hence the object would have been "found". The loss of the 25th magnitude object would not be considered at this point, as this tendency to lose the fainter objects more readily would presumably be reflected in the completenesses calculated at fainter magnitude levels.

A total of 300 objects were added at each 0.5 magnitude interval from $B = 22$ through $B = 26$. The completenesses were calculated by simply dividing the number of objects "found" by the number which had been originally added to the region $r > 50''$. The results of these calculations, which took some one hundred cpu hours on the University of Victoria Department of Physics' VAX 11/750 and an additional fifty cpu hours on the Dominion Astrophysical Observatory's VAX 11/780, are shown graphically in Figure 4. The hand-drawn curve was used to interpolate for values at 0.2 magnitude intervals and the results are contained in Table 6.

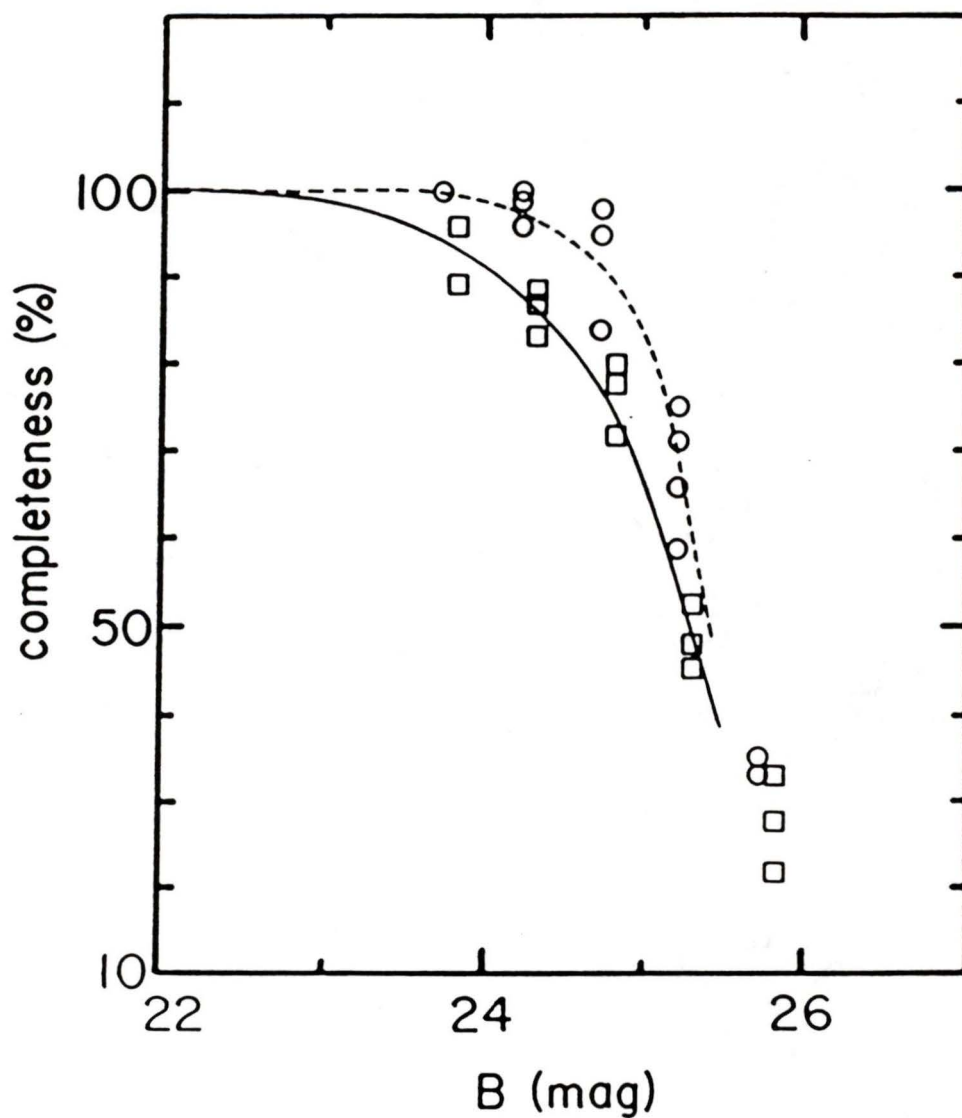


Figure 4. Calculated completeness as a function of magnitude. The squares correspond to completenesses calculated for the M87 object list, and the hand-drawn solid curve has been used to interpolate for the values given in Table 6. The circles and the dashed line correspond to completenesses determined for the background sample.

3.2 Background Corrections

The determination of the background (and foreground) correction for M87 has been discussed at length by Harris and Smith (1981), Harris (1985), and in Paper I. As in Paper I, use was made of five different observations totalling four hours of integration time on what is listed in Table 1 as a "Virgo Field", a region approximately half way between M87 and M49. These data frames were trimmed, bias and dark corrected, flat-fielded, aligned and coadded in exactly the same manner as described in Chapter 2 for the M87 data frame. Using the R2D2 command PHOTPROF, the FWHM of the stellar images was found to be about 4.0 ± 0.5 pixels (1.6 arcseconds), which was deemed sufficiently similar to the value (~ 1.4 arcseconds) determined for the M87 frame to allow valid corrections to the M87 data to be made. DAOPHOT itself was modified again to remove the background re-addition statements necessary for reducing the M87 frame, but was otherwise unchanged. No background subtraction was applied to this frame since the sky level was reasonably uniform and presumably well within the capacity of DAOPHOT to correct for.

The object-finding routine was once again used with a detection threshold of 2.5 sigma above the background. A PSF appropriate to this frame was determined as well, where starlike PSF candidates were iteratively rejected when their actual galactic natures (i.e. over-subtracted cores after fitting and "removal") became evident. Although the field was not at all crowded, the single-profile fitting

routine PEAK was used nonetheless, and the resulting fits were subtracted from the original data to look for possible hidden objects. As with the M87 frame, NSTAR was run twice over the list of detected objects to ensure good fitting convergence and accurate magnitudes. The zero point correction to the instrumental magnitudes was determined by C. Pritchett using the same equatorial and M67 standards used for M87. Finally, completeness tests were carried out in exactly the same manner as described above. The resulting completenesses are plotted in Figure 4, and values interpolated from the hand-drawn curve are contained along with those of M87 in Table 6.

The apparent luminosity function determined for the field frame is plotted in Figure 5, where the objects in the NSTAR output list have been grouped into bins 0.2 magnitudes wide to optimize the sampling while keeping the size of the error bars due to counting statistics relatively small. In keeping with a least-squares fit to the data by C. Pritchett, the functional dependence of the surface density of objects (per arcminute squared) on the magnitude was taken to be linear in log space so that:

$$\log \sigma_b = -12.812 + 0.543 B \quad (5)$$

where the value of B is central to the range of each bin.

At the magnitude levels considered here, the apparent luminosity function shown in Figure 5 would be expected to represent the growth primarily in the number of background galaxies with increasing

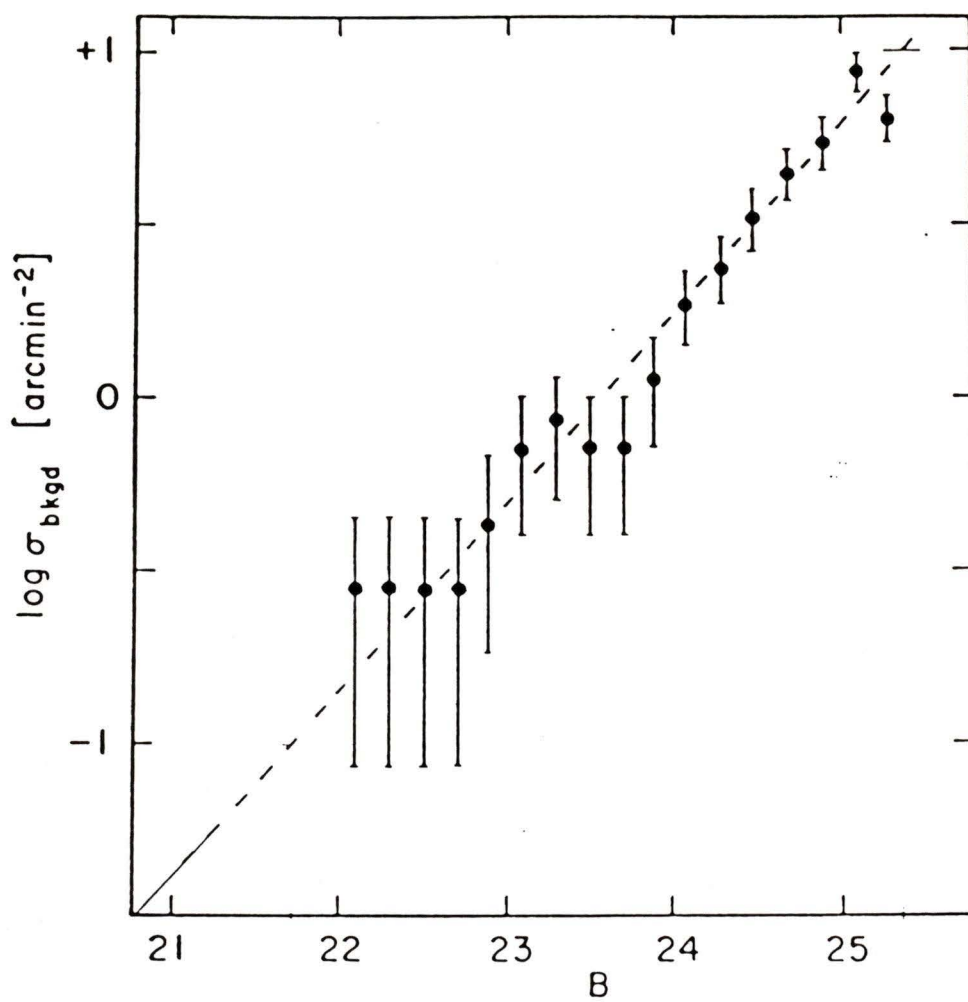


Figure 5. Apparent luminosity function of objects found in the background field. The dashed line is a least-squares fit to the data and has a slope of 0.543.

magnitude. However, the slope given in equation (5) is somewhat steeper than the values of between 0.4 and 0.48 normally determined from galaxy counts (Tyson and Jarvis 1979; King and Ellis 1985, Figure 7). Furthermore, although the area of their plate which they selected for reduction was chosen at the outset to be free of any apparent clusters of galaxies, Harris and Smith (1981) have done a photometric analysis of a region only 20 arcminutes away from the field studied here and find, to about $B = 24.0$, the slope of the apparent luminosity function (0.41) to be consistent with that expected from galaxy counts. The integrated surface density of objects which they determined ($5.3 \pm 1 \text{ arcmin}^{-2}$), however, is in reasonable agreement with a value of 6.6 arcmin^{-2} arrived at by straightforward summation to $B = 24.0$ using equation (5) above. A revised figure of 5.8 arcmin^{-2} (Harris 1985) is in somewhat better agreement with the value determined here, though this depends on what limiting magnitude one assumes for the data of Harris and Smith (1976).

Non-statistical variations in the background counts have been discussed in Paper I, where it has been suggested, based on the work of Infante et al. (1986), that fluctuations of about 30% in the number counts could be expected from one area to the next for fields 2 by 3 arcminutes in size. This implies that the constant in equation (5) is rather uncertain, and could easily account for the difference in background surface densities determined here and by Harris (1985). It should be noted that the background correction is not nearly as

critical to the results of the present study as it was to the counts of Harris and Smith since globular cluster surface densities are much higher in the central regions which are considered here. At $B = 25$, globular clusters account for about 70% of the number of detected objects in the present data.

The larger slope determined here may have been the result of magnitude-dependent object rejection criteria in DAOPHOT, which is by design primarily a crowded-field photometry program wherein image-analysis plays a secondary role. Some simple tests were carried out with artificial images whose magnitudes and FWHM were sequentially varied and it was found that, while the DAOPHOT finding algorithm was generally able to distinguish and reject objects more extended than the FWHM specified for the search, this function indeed became less and less reliable at fainter magnitudes. The result would have been to depopulate the brighter end of the luminosity function of galaxies while leaving the fainter end to contain practically all intensity enhancements found, thereby steepening the slope from its expected value.

The important thing to remember, however, is that whatever the manner in which these rejection criteria varied with magnitude, they should have had a similar dependence in both the background and the M87 data frames, all other operations having been carried out identically. Consequently, equation (5) was used throughout subsequent reductions to determine the background level appropriate to each magnitude bin.

3.3 The Luminosity Function

As for the background field, the objects listed in Table 4 were grouped into bins 0.2 magnitudes wide. The number of objects in each bin was then divided by the appropriate completeness fraction from Table 6, and a background/foreground surface density calculated using equation (5) was subtracted from the result. The globular cluster luminosity function so determined is tabulated in Table 6 and plotted in Figure 6, where surface densities have been computed by dividing the entries in Table 6 by the analysed field area of 4.85 arcmin^2 . The error bars shown in this plot reflect the area-and-completeness scaled counting errors, which, assuming Poisson statistics, go as the square root of the number of objects found in each bin.

Since the assumed completeness limit of 50% is reached around $B = 25.5$, the leveling off of the luminosity function at $B \approx 25$ appears to be real and constitutes the first time this peak has been detected in galaxies outside the local group. It has been shown that for Local Group galaxies, the globular cluster luminosity functions may be approximately represented by a Gaussian with $\langle M_V \rangle = -7.3$ and $\sigma = 1.2$ magnitudes (Harris and Racine 1979), though van den Bergh (1985) has determined that a value of $\langle M_V \rangle = -7.1$ is in better agreement with more recent compilations of globular cluster data (Webbink 1985; Crampton et al. 1985). In paper I, we have made the (possibly unjustified) assumption that this form of the globular cluster luminosity function might be common to galaxies not of the Local Group

Table 6

Counts of Images in M87 and Background Fields

B	Background Field			M87			
	N_{obs}^a	f^b	N_{corr}^c	N_{obs}^a	f^b	N_{bkgd}^d	N_{corr}^e
20.0 → 20.2	-	1.00	-	1	1.00	0.06	0.9
20.2 → 20.4	-	1.00	-	1	1.00	0.08	0.9
20.4 → 20.6	-	1.00	-	1	1.00	0.10	0.9
20.6 → 20.8	1	1.00	1	1	1.00	0.13	0.9
20.8 → 21.0	-	1.00	-	1	1.00	0.17	0.8
21.0 → 21.2	-	1.00	-	3	1.00	0.22	2.8
21.2 → 21.4	-	1.00	-	7	1.00	0.28	6.7
21.4 → 21.6	1	1.00	1	2	1.00	0.36	1.6
21.6 → 21.8	-	1.00	-	8	1.00	0.46	7.5
21.8 → 22.0	-	1.00	-	4	1.00	0.59	3.4
22.0 → 22.2	2	1.00	2	17	1.00	0.76	16.2
22.2 → 22.4	2	1.00	2	15	1.00	0.98	14.0
22.4 → 22.6	2	1.00	2	19	1.00	1.3	17.7
22.6 → 22.8	2	1.00	2	19	1.00	1.6	17.4
22.8 → 23.0	3	1.00	3	22	1.00	2.1	19.9
23.0 → 23.2	5	1.00	5	24	1.00	2.7	21.3
23.2 → 23.4	6	1.00	6	26	1.00	3.4	22.6
23.4 → 23.6	5	1.00	5	33	0.99	4.4	28.8
23.6 → 23.8	5	1.00	5	41	0.98	5.6	36.0
23.8 → 24.0	8	0.99	8.1	43	0.97	7.3	37.1
24.0 → 24.2	13	0.98	13.2	45	0.94	9.3	38.5
24.2 → 24.4	16	0.97	16.5	50	0.91	12.0	42.8
24.4 → 24.6	22	0.95	23.1	66	0.88	15.4	59.5
24.6 → 24.8	29	0.93	31.1	62	0.85	19.7	53.3
24.8 → 25.0	31	0.84	36.9	68	0.78	25.3	61.6
25.0 → 25.2	44	0.74	59.5	60	0.66	32.5	58.1
25.2 → 25.4	27	0.63	43.2	44	0.54	41.8	39.4

^a Areas are 4.85 and 7.0 arcmin² for M87 and background, respectively.

^b Completeness fraction from Figure 4.

^c Corrected for incompleteness.

^d Background computed from equation (5), normalized to 4.85 arcmin².

^e Corrected for incompleteness and background contamination.

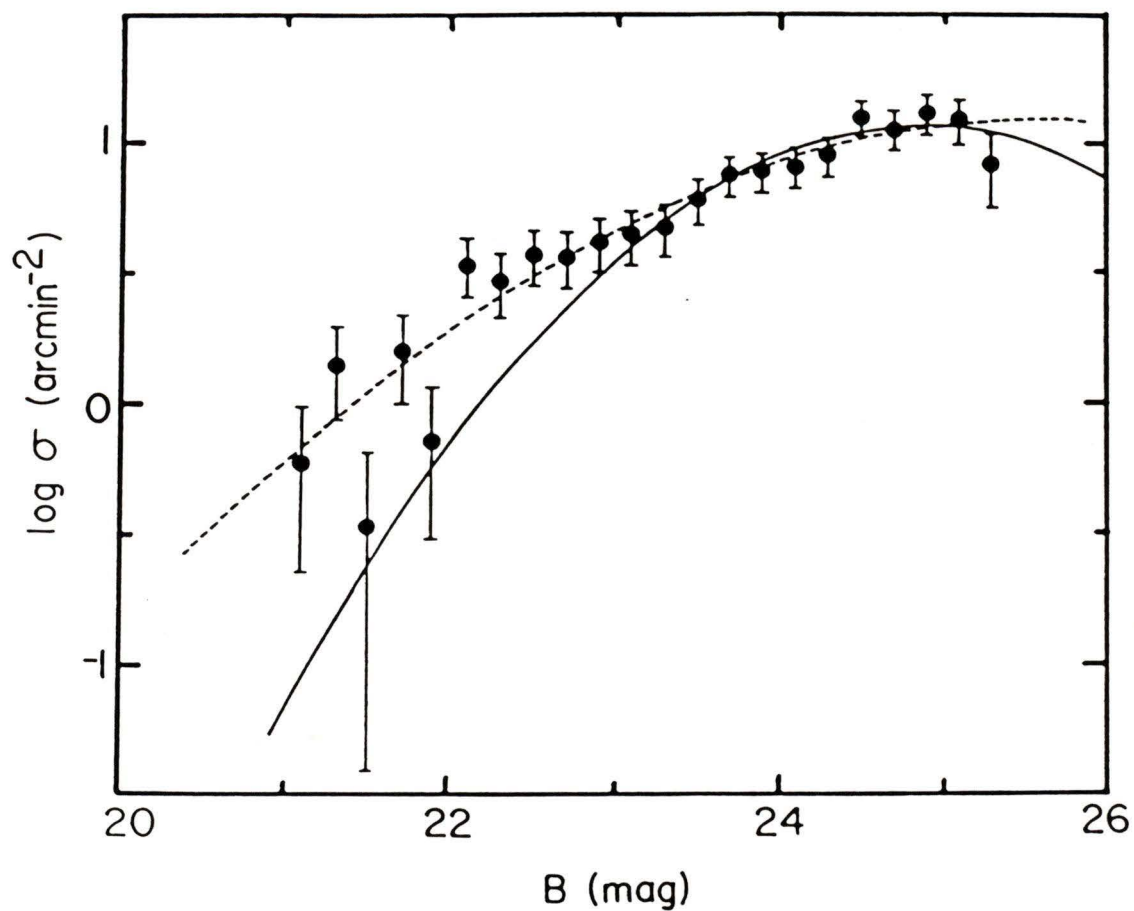


Figure 6. The globular cluster luminosity function for the region $50'' < r < 159''$. The solid curve has $B_0 = 24.86$ and is a best-fit to the data in the magnitude range $23 < B < 25.5$ assuming $\sigma = 1.2$. The dashed curve corresponds to a best-fit to the data in the range $21 < B < 25.5$ and has $B_0 = 25.64$ and $\sigma = 1.89$. The error bars correspond to \sqrt{N} statistics.

as well, in order that one could use the presently determined luminosity function as a standard candle for determining the distance to M87. Notwithstanding the validity of this assumption, the fact that we have been able to extend the luminosity function past its peak should make such a distance determination considerably more reliable than similar attempts (Racine 1968; Sandage 1968; Hanes 1977b) carried out by fitting only the bright tail of the assumed Gaussian.

On the other hand, there is reason to suspect that the luminosity function of M87's globular clusters may be different from that of Local Group galaxies. In particular, M87 is not a spiral or irregular galaxy such as those in the Local Group which have been found to contain globular clusters. In addition, aside from the fact that M87 has been shown to have a highly abnormal number of globulars for any galaxy, the observed radial distribution of these clusters may also differ from those found in the Local Group. Consequently, a distance to the Virgo cluster derived from the present data cannot be considered as being very reliable until a better grasp has been obtained of the way in which various environmental influences combine to produce and alter globular cluster populations (Sandage and Tammann 1985).

The fitting probability of a Gaussian has been maximized numerically with respect to the height h , mean magnitude B_0 , and width σ using the probability function (Bevington 1969):

$$\ln\{P(h, B_0, \sigma)\} = \sum_i \{N_i \ln\{y(B_i)\}\} - \sum_i y(B_i) + \text{const} \quad (6)$$

for the data in Table 6, where B_i , N_i , and y are the magnitude, counted number, and fitted number appropriate to the i th bin, and P denotes the fitting probability. $y(B_i)$ is calculated using incremental values of h , B_0 , and σ and the result is added to the background and multiplied by the completeness fraction to determine the run of $\ln P$. Setting $\sigma = 1.2$, an optimal value of $B_0 = 24.86 \pm 0.3$ is determined from a fit to the data lying in the range $23 < B < 25.5$. The error has been estimated by fitting a similar Gaussian to surface densities calculated using a logarithmic slope for the background luminosity function of 0.4, varying the zero point of this luminosity function by 30% in either direction, and using different subsets of the data in the range $22 < B < 25.5$. The value of B_0 found here is slightly different from the value of $B_0 = 25.0 \pm 0.3$ determined in Paper I due to the somewhat different weighting applied to the data points using the present fitting procedure. The two values agree to well within their estimated uncertainties, however.

Using a globular cluster color of $(B-V)_0 = 0.80$ and assuming $A_V = .07$ (Paper I, Burstein and Heiles 1984), the present fit to the data predicts a distance modulus for M87 of $(m-M)_0 = 31.09 \pm 0.3$, corresponding to a revised distance of 16.5 ± 2.3 Mpc. Again, the reader is advised that although this distance is in reasonable agreement with values determined using other methods (Aaronson and

Mould 1983), it is certainly no more accurate, given the primary uncertainty regarding the universality of globular cluster luminosity functions. Adopting an undecelerated Hubble flow velocity of $1305 \pm 60 \text{ km sec}^{-1}$ as in Paper I, then the revised distance to M87 determined above gives a global Hubble constant $H_0 = 79 \pm 12 \text{ km sec}^{-1} \text{ Mpc}^{-1}$.

It will be noted from Figure 6 that the fit of the Gaussian (a parabola in log-space) corresponding to $\sigma = 1.2$ is not a good one for clusters brighter than about $B = 23$. Indeed, using a Kolmogoroff-Smirnoff test, it has been determined that a fit to the data in the interval $21 < B < 25.5$ of a Gaussian with $\sigma = 1.2$ can be rejected at the 99% confidence level. Allowing σ to vary while maximizing the probability function in equation (6), a formal best fit to the data for $21 < B < 25.5$ gives values of $B_0 = 25.64$ and $\sigma = 1.89$. This fit is shown as the dashed curve in Figure 6.

Before one can make the claim that the luminosity function of M87 globular clusters is indeed different from that found in Local Group galaxies, one should first compare the two directly. Again using a Kolmogoroff-Smirnoff test, the present sample was compared to the data of Harris and Racine (1979) for Galactic globular clusters, using M87 distance moduli of 31.5 and 31.09. The tests showed that in both cases, the null hypothesis (that the two luminosity functions were derived from the same parent distribution) could not be rejected at the 10% confidence level. Similarly for M31, where the data have been taken from Racine and Shara (1979) and a mean $(B-V)_0$ of 0.82 is

assumed for M31 clusters, no conclusive difference between luminosity functions was found if the distance moduli of M31 and M87 were taken to be 24.38 (de Vaucouleurs 1978) and 31.09, respectively. If, however, a distance modulus of 31.5 is assumed for M87, then the probability that the differences between the two luminosity functions are due only to random errors decreases to only about 1%. Van den Bergh (1985) has performed a similar comparison using the more recent M31 data of Crampton et al. (1985) and finds that, assuming distance moduli of $(m-M)_V = 24.32$ and 31.30 for M31 and M87, respectively, the luminosity functions of M87 and M31 are different at the 95% significance level.

Consequently, it can not yet be said with certainty that locally observed globular cluster luminosity functions are actually reflected in the cluster population of M87, much less that they might be "universal". It would be very interesting in future observing programs to try to extend the present data (using the Hubble Space Telescope) to light levels two or three magnitudes beyond the peak of the Gaussian, in addition to refining the distance to M87 through other methods, so that more positive comparisons could be made. Even then, however, meaningful comparisons are limited by the relatively small number of globular clusters found in the Local Group. It may now be more profitable to begin looking for consistency among globular cluster luminosity functions in galaxies exclusively outside the local group, and particularly among galaxies of the same morphological type.

CHAPTER 4

THE RADIAL DISTRIBUTION OF M87 GLOBULAR CLUSTERS

Having in hand a reasonably large data set, it was decided to look for radial variations in the luminosity function of M87 globulars within the region extending from about 20 arcseconds to 160 arcseconds from the apparent center of M87. The inner limit was dictated both by the onset of significant numbers of apparently spurious images as well as by the rapid falloff of calculated completeness fractions with decreasing radius in this region.

4.1 Radial Completeness Corrections

In order to compare luminosity functions from different radial regions properly, account had to be taken of the variation in completeness of the data with radius. This variation was approximated readily enough using the same ADD* and NSTAR output object lists generated as described in the last chapter. For the problem at hand, the added objects were divided into individual groups occupying one of

ten concentric zones of equal area. These objects were then once again compared with the original list of objects given in Table 4, and specifying one magnitude and one pixel tolerances, respectively, completenesses were determined as a function of the radial bin for each set of input magnitudes. The results of these calculations are given in Table 7.

Due to the smaller number of objects involved in each calculation, the scatter in the final completenesses was somewhat larger than the 3% scatter found for the data set taken as a whole, particularly for the fainter objects. Consequently, completeness uncertainties appropriate to each radial and magnitude interval were estimated by noting the scatter of individual calculations about their mean value. These estimated uncertainties are listed in Table 7, and were included in all subsequent calculations.

In Figure 7 are shown "curves" representing the completenesses as a function of radius, where the means of each set of calculations have been connected by straight lines. Actual corrections to the data, however, were made using the discrete values of completeness corresponding to each bin. Completeness curves for bins whose magnitudes were not actually tested during the completeness calculations of the last chapter were generated by linear interpolation.

Table 7

Completeness as a Function of Radius and Magnitude

inner radius (pixels)	50	100	133	159	182	204	226	247	267	296
outer radius (pixels)	100	133	159	182	204	226	247	267	296	387
$\langle r \rangle_{\text{area}}$	79	118	147	171	193	215	237	257	279	319
B	Completeness (%) ± estimated error									
20.0 → 20.2	100 1	100 1	100 1	100 1	100 1	100 1	100 1	100 1	100 1	100 1
20.2 → 20.4	100 1	100 1	100 1	100 1	100 1	100 1	100 1	100 1	100 1	100 1
20.4 → 20.6	100 1	100 1	100 1	100 1	100 1	100 1	100 1	100 1	100 1	100 1
20.6 → 20.8	100 1	100 1	100 1	100 1	100 1	100 1	100 1	100 1	100 1	100 1
20.8 → 21.0	100 1	100 1	100 1	100 1	100 1	100 1	100 1	100 1	100 1	100 1

Table 7 - continued

B	Completeness (%) ± estimated error									
21.0 → 21.2	100 1	100 1	100 1	100 1	100 1	100 1	100 1	100 1	100 1	100 1
21.2 → 21.4	100 1	100 1	100 1	100 1	100 1	100 1	100 1	100 1	100 1	100 1
21.4 → 21.6	100 1	100 1	100 1	100 1	100 1	100 1	100 1	100 1	100 1	100 1
21.6 → 21.8	100 1	100 1	100 1	100 1	100 1	100 1	100 1	100 1	100 1	100 1
21.8 → 22.0	99 1	99 1	100 1	100 1	100 1	100 1	100 1	100 1	100 1	100 1
22.0 → 22.2	97 1	98 1	99 1	100 1	100 1	100 1	100 1	100 1	100 1	100 1
22.2 → 22.4	96 1	97 1	98 1	99 1	100 1	100 1	100 1	100 1	100 1	100 1
22.4 → 22.6	93 1	96 1	98 1	99 1	100 1	100 1	100 1	100 1	100 1	100 1
22.6 → 22.8	89 1	95 1	97 1	98 1	99 1	100 1	100 1	100 1	100 1	100 1
22.8 → 23.0	85 1	93 1	97 1	98 1	99 1	100 1	100 1	100 1	100 1	100 1

Table 7 - continued

B	Completeness (%)									
	± estimated error									
23.0 → 23.2	81 1	91 1	96 1	98 1	99 1	100 1	100 1	100 1	100 1	100 1
23.2 → 23.4	77 2	89 2	95 1	98 1	99 1	100 1	100 1	100 1	100 1	100 1
23.4 → 23.6	73 4	87 4	94 3	98 3	99 2	100 2	100 1	100 1	100 1	100 1
23.6 → 23.8	68 6	84 5	93 4	96 4	98 3	99 3	100 2	100 1	100 1	100 1
23.8 → 24.0	63 8	80 7	90 6	93 6	95 5	96 4	97 3	97 2	98 1	98 1
24.0 → 24.2	58 10	76 9	86 8	90 7	92 6	93 5	94 4	95 3	96 2	97 1
24.2 → 24.4	51 13	70 13	82 12	87 12	89 12	90 11	92 10	94 9	96 8	97 7
24.4 → 24.6	41 16	62 16	77 14	83 14	85 13	87 12	89 10	91 6	94 6	96 6
24.6 → 24.8	27 20	55 20	72 15	79 15	82 15	83 15	85 15	88 10	91 10	95 10

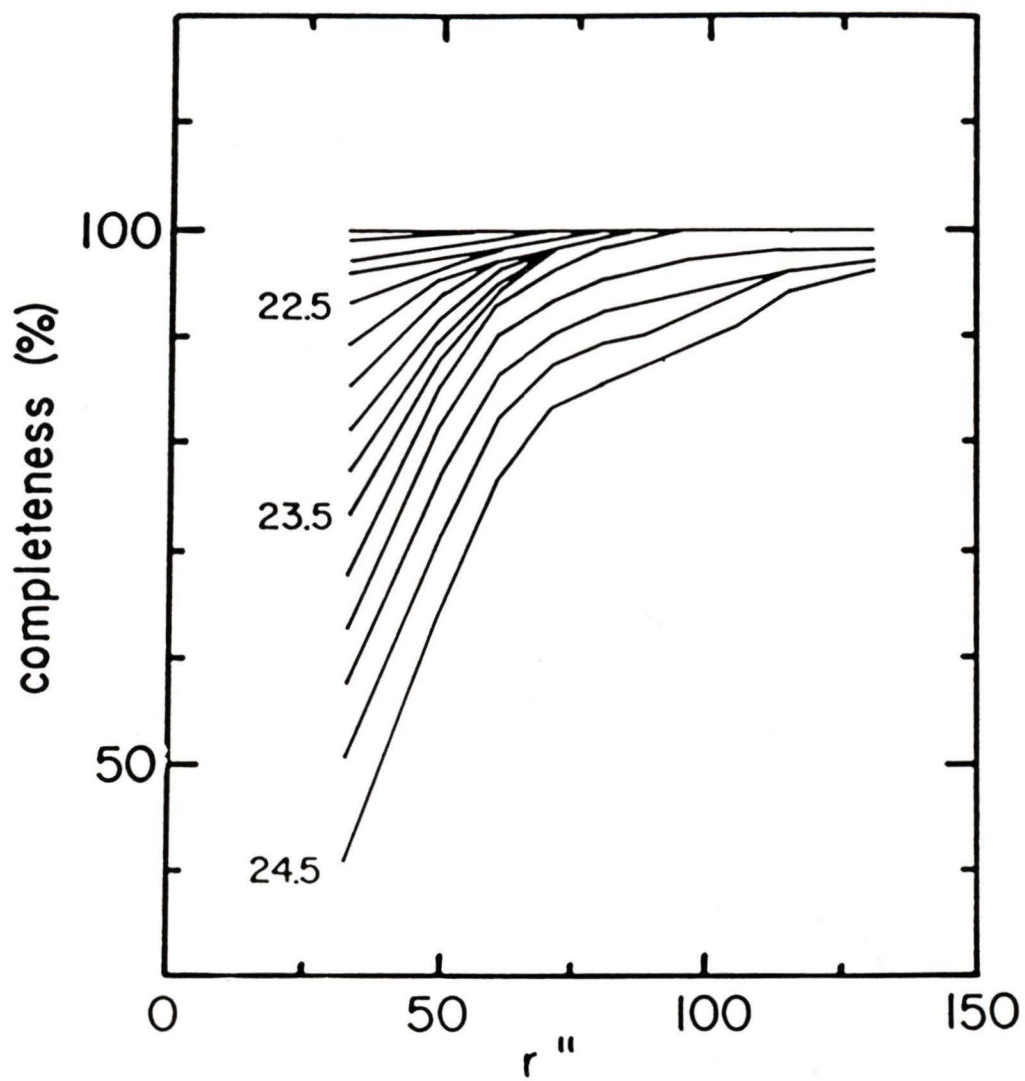


Figure 7. Completeness calculated as a function of magnitude and radius.

4.2 Spurious Images

The limiting magnitude for this study was determined both by the assumed 50% completeness limit in the innermost zone as well as by the onset of spurious images within this region. The 50% completeness limit for the innermost zones was found to occur at $B \approx 24.4$ by simply reading off the completeness curves shown in Figure 7. The point at which the number of spurious images became significant, however, was somewhat harder to define.

In order to test approximately the tendency of DAOPHOT to ascribe positions and magnitudes to purely noise-induced intensity enhancements, several artificial frames were created which mimicked the noise distribution found in the original data. Using R2D2, the background-subtracted M87 data frame was "cleaned" of images using the RMVSTAR command, which generated a new frame wherein 15 by 15 pixel blocks were assigned the modal intensities found in the corresponding areas of the original frame. Though the background intensity was fairly flat to begin with, the DAOPHOT finding routine was applied to the cleaned frame as a test to ensure that slight differences in intensity between neighboring blocks did not generate spurious images on their own. The inability of FIND to detect any local maxima confirmed that this frame was indeed sufficiently smooth for the present purposes.

A Gaussian noise distribution was added across the smooth frame, where the appropriate sigma was calculated for each pixel by adding

back the originally subtracted sky and de Vaucouleurs law as well as a 2.5 ADU readout noise contribution. The standard deviation of the mean intensity as a function of coordinate for both the cleaned frames and the original was found to be practically identical. DAOPHOT was then used to detect and measure all possible images in the same manner and using the same seeing and fitting parameters as described in Chapter 2.

Rather alarmingly, each of the four generated noise frames was found to contain more than 900 local maxima at the 2.5 sigma level or higher. Running NSTAR twice, however, reduced this amount to about 400 objects per frame. In addition, comparatively few objects were found to have magnitudes which fell within the region of interest to the present study. The mean luminosity functions for the four artificial frames are plotted along with the uncorrected data of Table 6 in Figure 8, where it can be seen that purely noise-induced images have a mean magnitude of $B \approx 26.3$.

Figure 8 is intended only to indicate the typical magnitude and dispersion of noise-generated intensity enhancements, and it should be borne in mind that the actual number and distribution of objects found in the artificial frames cannot realistically be applied to the object list in Table 4 since: a) the DAOPHOT finding efficiency for these objects is enhanced by the lack of real, brighter objects which would otherwise hide them (compare the completenesses determined for the background and those computed for the M87 frame, for example); and b) contributions to the number of spurious images by "cosmic rays", hot

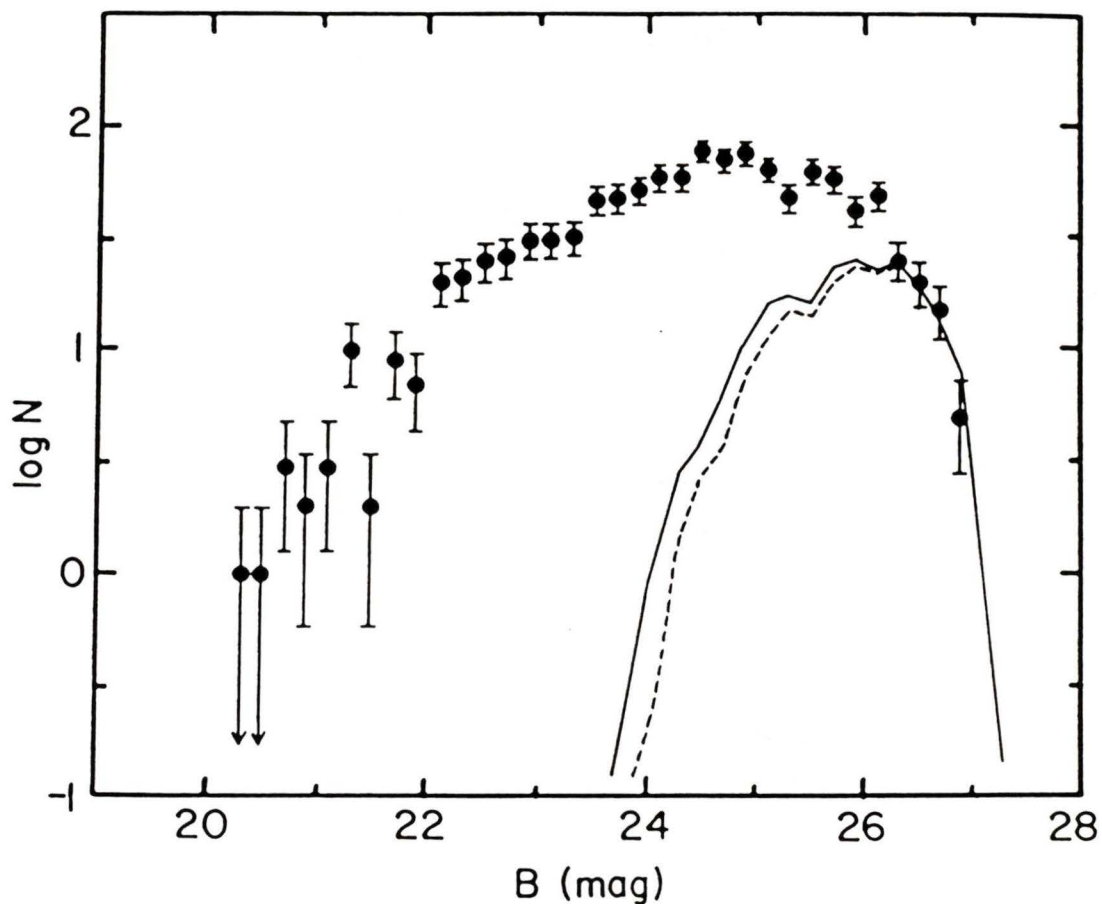


Figure 8. The luminosity function of noise-generated intensity enhancements. The solid line corresponds to "spurious" images found at $r > 20$ arcseconds, while the dashed line indicates the distribution for $r > 50$ arcseconds. Note that these distributions do not represent the expected number of spurious images contained in the M87 object list (see text). The filled circles represent the uncorrected luminosity function of the objects listed in Table 4.

pixels, etc. have not been taken into account. Normalizing the number of noise-generated objects so that their number is everywhere less than or equal to the number of objects found in the original frame, a very approximate upper limit to the contribution of spurious, noise-induced objects at $B = 25.5$ is found to be about 20%. This is slightly larger than the uncertainty in the number of clusters due to counting statistics.

As an additional check, it was decided to assess the legitimacy of each of the 885 objects brighter than $B = 25.5$ by examining them visually on the monitor. This was done in an effort merely to estimate the extent of contamination of the sample by spurious images, and no corrections were applied to the data in order that the inherent objectivity of the photometry routine not be compromised. It was found that only about 50 objects could be labelled as possibly suspect, having profiles which looked rather ragged or asymmetric. In the innermost zone this amounted to some 20 objects, of which only 6 were brighter than $B = 24.4$. Consequently, it was concluded that spurious images did not constitute a significant portion of the sample down to the limiting magnitudes established by the 50% completeness criterion.

4.3 Radial Variations in the Luminosity Function

Using the completenesses given in Table 7 and subtracting the background appropriate to each magnitude bin, luminosity functions were determined for five concentric zones of equal area and are given in Table 8. The logarithmic surface densities are plotted in Figures 9 and 10. In Figure 10, the integrated surface density of objects in zones 2 through 5 have been normalized to the integrated surface density in the innermost zone, and the curve shown is a parabola corresponding to the best-fit Gaussian for the overall luminosity function discussed in Chapter 3.

The Kolmogoroff-Smirnoff test has been applied to each possible pair of the five luminosity functions shown to determine whether an overall trend exists in the data. In all but three cases, the hypothesis that the observed differences are due to random errors cannot be rejected at the 90% significance level or less. For two cases (zones 1 and 2, and zones 3 and 5), the distributions are different at the 95% significance level, and comparing the luminosity function of zone 2 with that of zone 5, a 99.9% significance level is indicated. Though this last figure would suggest a high probability that the parent distributions of zones 2 and 5 are different, the outermost zone contains considerably fewer globular clusters (~50) and is likely to be more noise-dominated than the rest. In addition, the fact that there seem to be no statistically significant differences in the distributions of the first and fourth, first and fifth, and second

Table 8

Differential Luminosity Functions for Five Radial Zones

B	zone 1 (0.34 → 0.91)		zone 2 (0.91 → 1.24)		zone 3 (1.24 → 1.54)		zone 4 (1.54 → 1.82)		zone 5 (1.82 → 2.64)	
	N ^a	σ ^b	N	σ	N	σ	N	σ	N	σ
20.4 → 21.2	3	2.6 ± 1.5 ^c	2	1.7 ± 1.2	2	1.7 ± 1.2	1	0.9 ± 0.9	1	1.1 ± 1.1
21.2 → 22.0	10	8.6 ± 2.7	0	0.0 ± 0.0	7	5.9 ± 2.2	5	4.2 ± 1.9	6	5.5 ± 2.2
22.0 → 22.8	31	27.6 ± 5.0	24	20.1 ± 4.1	16	13.3 ± 3.3	13	10.8 ± 3.0	8	6.8 ± 2.4
22.8 → 23.6	41	40.2 ± 6.3	26	20.8 ± 4.1	26	20.3 ± 4.0	27	21.0 ± 4.0	21	17.9 ± 3.9
23.6 → 24.4	50	55.4 ± 7.8	68	60.0 ± 7.3	51	40.5 ± 5.7	33	23.0 ± 4.0	16	9.0 ± 2.2

^aCounted number in each bin - zonal areas are 1.12 arcmin².

^bSurface density (units of arcmin⁻²) corrected for completeness and background contamination.

^cIncludes uncertainty due to completeness corrections.

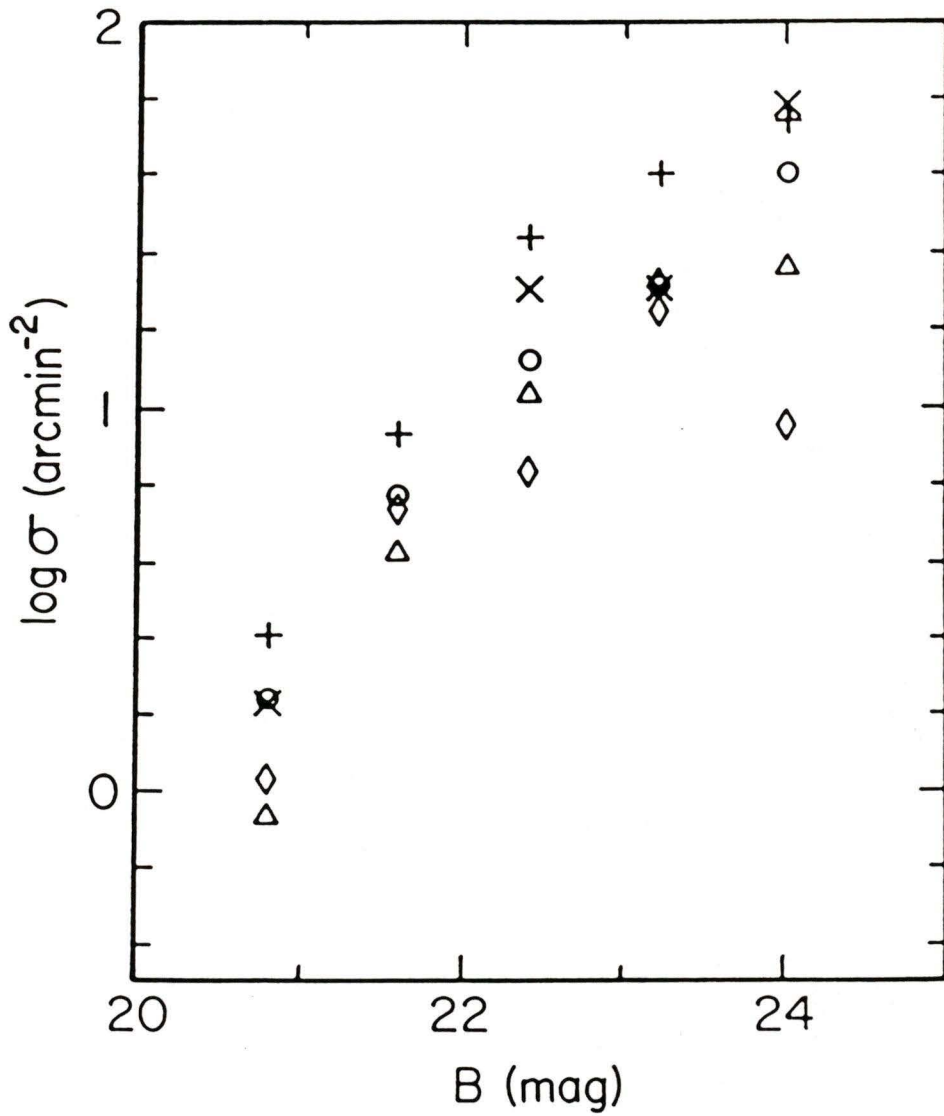


Figure 9. Differential luminosity functions in five radial zones. The correspondence of symbols to respective zones is the same as in Figure 2.

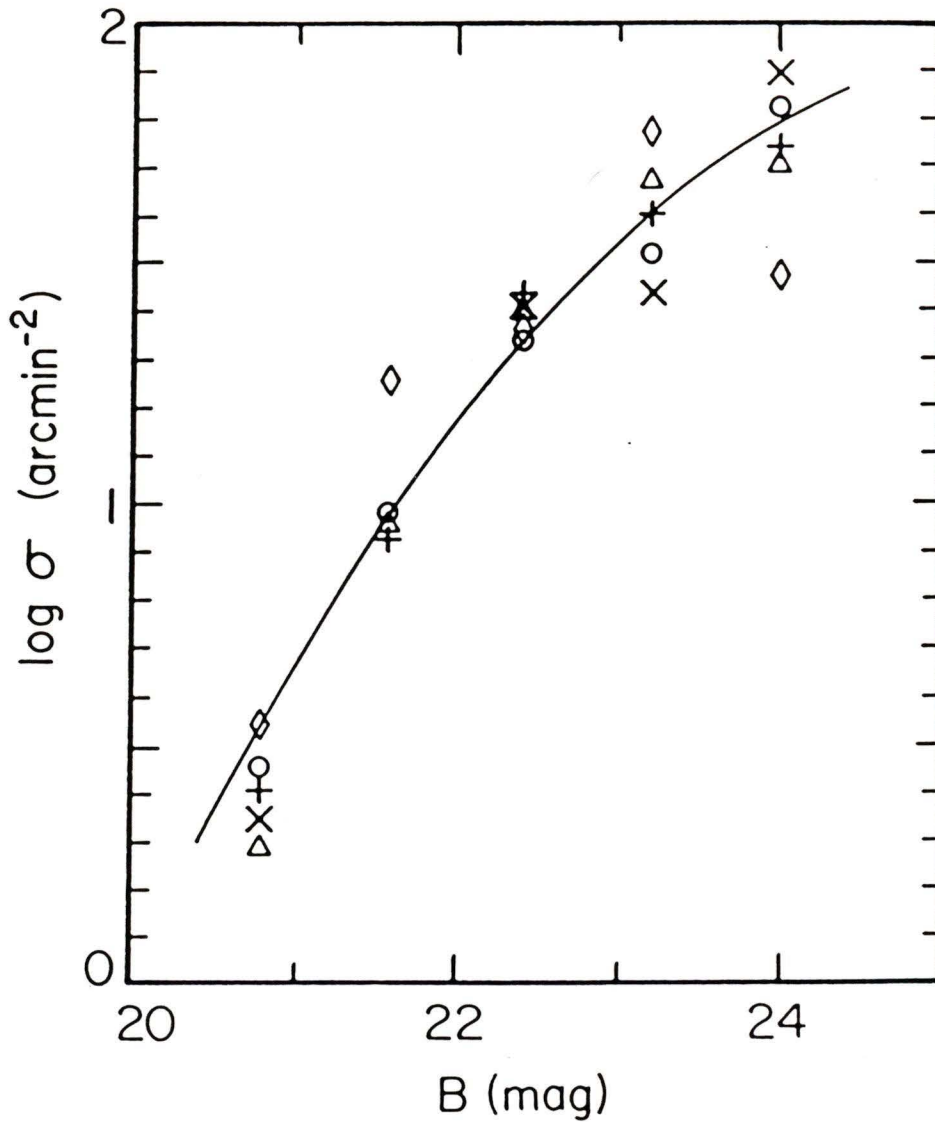


Figure 10. Normalized differential luminosity functions in five radial zones. The total number of objects in each radial zone has been normalized to the total number in zone 1. The correspondence of symbols to respective zones is the same as in figure 2, and the curve corresponds to a Gaussian with $B_0 = 25.64$ and $\sigma = 1.89$ as in Figure 6.

and fourth zones would argue against the likelihood of a significant radial trend having been detected. If a logarithmic slope of 0.4 is assumed for the background/foreground surface density, then the luminosity functions become even more similar, with all but one test indicating differences at the 90% significance level or less.

The frame was also divided into two concentric regions of 2.8 arcmin^2 each, and application of the Kolmogoroff-Smirnoff test to the two respective luminosity functions indicated that the differences could be attributed to random errors more than 10% of the time. Lastly, all luminosity functions were compared with the best fit Gaussian of parameters $B_0 = 25.64$ and $\sigma = 1.89$. The observed distributions were found to differ from this fit at less than the 90% significance level with the exception of the luminosity function extracted from zone number 2, which was found to differ from the fit at the 96% significance level. The conclusion to be made, therefore, is that there is no evidence within the present data for a statistically significant trend of the luminosity function with radius.

This result is not entirely unexpected when one considers that: a) the radial region examined here is rather small compared with the overall extent of M87's globular cluster system; b) at such small radii, one would expect that through projection effects, the large extent of the cluster system would tend to dilute differences in a radially varying luminosity function; and c) the luminosity function considered here does not possess a characteristic feature (a peak,

for example) which would make comparisons more meaningful. Certain evolutionary processes which might be expected to alter the luminosity distribution somewhat in this region will be considered in Chapter 5.

Strom et al. (1981) have found that for a region extending from 1.4 to 9.8 arcminutes from M87, no significant radial variation in the observed luminosity function is evident. Figure 11 shows their luminosity functions determined for annuli of mean radii 2, 3.4, 4.9, 6.25, and 7.9 arcminutes, as well as a luminosity function determined from Table 4 for $r > 20$ arcseconds and having a corresponding mean areal radius of 1.4 arcminutes. The solid curve in this figure corresponds to a fit to the data by Strom et al. assuming a value of $B_0 = 23.41$ (Hanes 1977a), and has $\sigma = 1.26$. The dashed curve represents the best-fit Gaussian determined in Chapter 3. The present data has been normalized to agree with the total number of objects found by Strom et al. in their innermost radial bin.

A Kolmogoroff-Smirnoff comparison was made with each of Strom et al.'s luminosity functions and, perhaps surprisingly, the only disagreement at more than the 95% significance level was found with Strom et al.'s distribution determined at a mean radius of two arcminutes, which ideally should have agreed with the present sample most closely. From Figure 11, it would appear that this result is most likely due to the diminishing completeness at faint magnitudes of Strom et al.'s sample with decreasing radius. The agreement between the present data and Strom et al.'s observations for radii greater than three arcminutes is an indication that no large scale variation of the

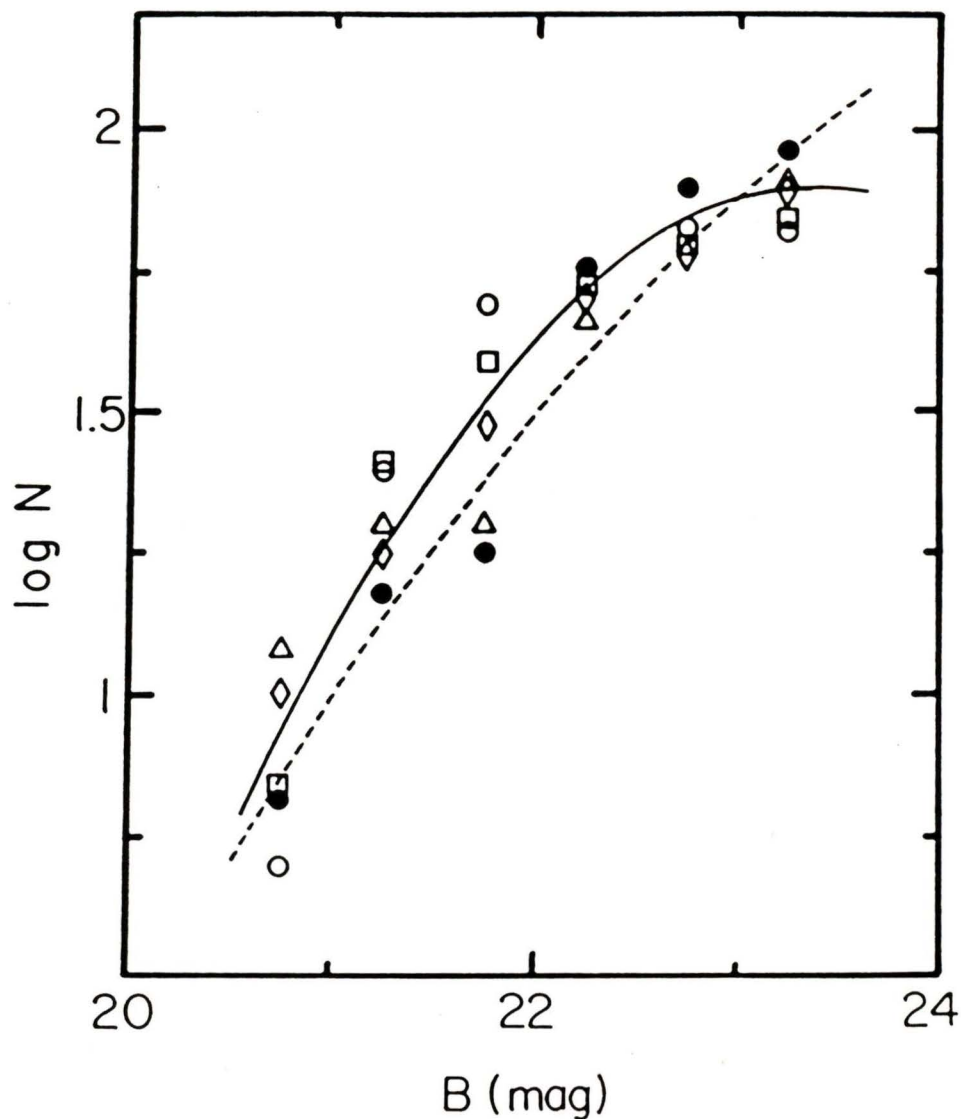


Figure 11. The differential luminosity function of the present sample as a whole compared with those of Strom et al. (1981) for larger radii. The objects in the present sample have been normalized to the total number found by Strom et al. in their innermost zone. Symbols correspond to zones as follows; filled circles - 0.33 + 2.65 arcminutes (present sample), hollow circles - 1.39 + 2.78 arcminutes, squares - 2.78 + 4.17 arcminutes, triangles - 4.17 + 5.56 arcminutes, diamonds - 5.56 + 6.95 arcminutes. The solid curve corresponds to a fit to the data by Strom et al. and has $B_0 = 23.41$ and $\sigma = 1.26$. The dashed curve has $B_0 = 25.64$ and $\sigma = 1.89$ as in Figure 6.

M87 globular cluster luminosity function has yet been detected. It would be helpful in this respect to obtain deep CCD observations of the outer regions of M87 's globular cluster system, so that the comparison might be extended to fainter magnitudes.

4.4 Radial Surface Density Profile

The projected spatial distribution of globulars in M87 has been discussed briefly in Paper I and in somewhat greater detail by Harris and Smith (1976) and Harris (1985). The position of these investigators is that the falloff in the number of globular clusters with increasing projected radius is less steep than a similar falloff seen in the background halo light.

In an effort to determine whether or not such a situation pertains within the region under study, the objects listed in Table 4 were corrected for completeness and background/foreground contamination, binned into the five concentric zones described in Table 8, and integrated to various limiting magnitudes. The resulting surface densities are tabulated in Table 9, and are plotted in Figure 12 together with the CCD halo profile of Davis et al. (1985). This halo profile agrees closely with the earlier measurements made by Kormendy (1977) and de Vaucouleurs and Nieto (1978), and suggests a power-law falloff having a slope of -1.6 in the region under

Table 9

Integrated Surface Densities (arcmin^{-2}) for Various Limiting Magnitudes

proj. radius ^a (arcmin)	B_{lim}				
	23.2	23.6	23.8	24.0	24.4
0.68	55.4 ± 7.0^b	79.0 ± 8.6	90.5 ± 9.2	106.3 ± 10.1	134.4 ± 11.6
1.08	31.5 ± 5.1	43.4 ± 6.0	53.4 ± 6.6	65.2 ± 7.3	103.4 ± 9.4
1.40	27.8 ± 4.8	41.1 ± 5.8	52.5 ± 6.5	60.2 ± 6.9	81.6 ± 8.1
1.68	27.1 ± 4.7	36.9 ± 5.4	41.8 ± 5.7	48.4 ± 6.1	59.8 ± 6.7
2.02	22.5 ± 4.5	31.3 ± 5.2	34.2 ± 5.4	37.7 ± 5.6	40.2 ± 5.6

^aMean areal radius for each zone.

^bIncludes uncertainty due to completeness corrections.

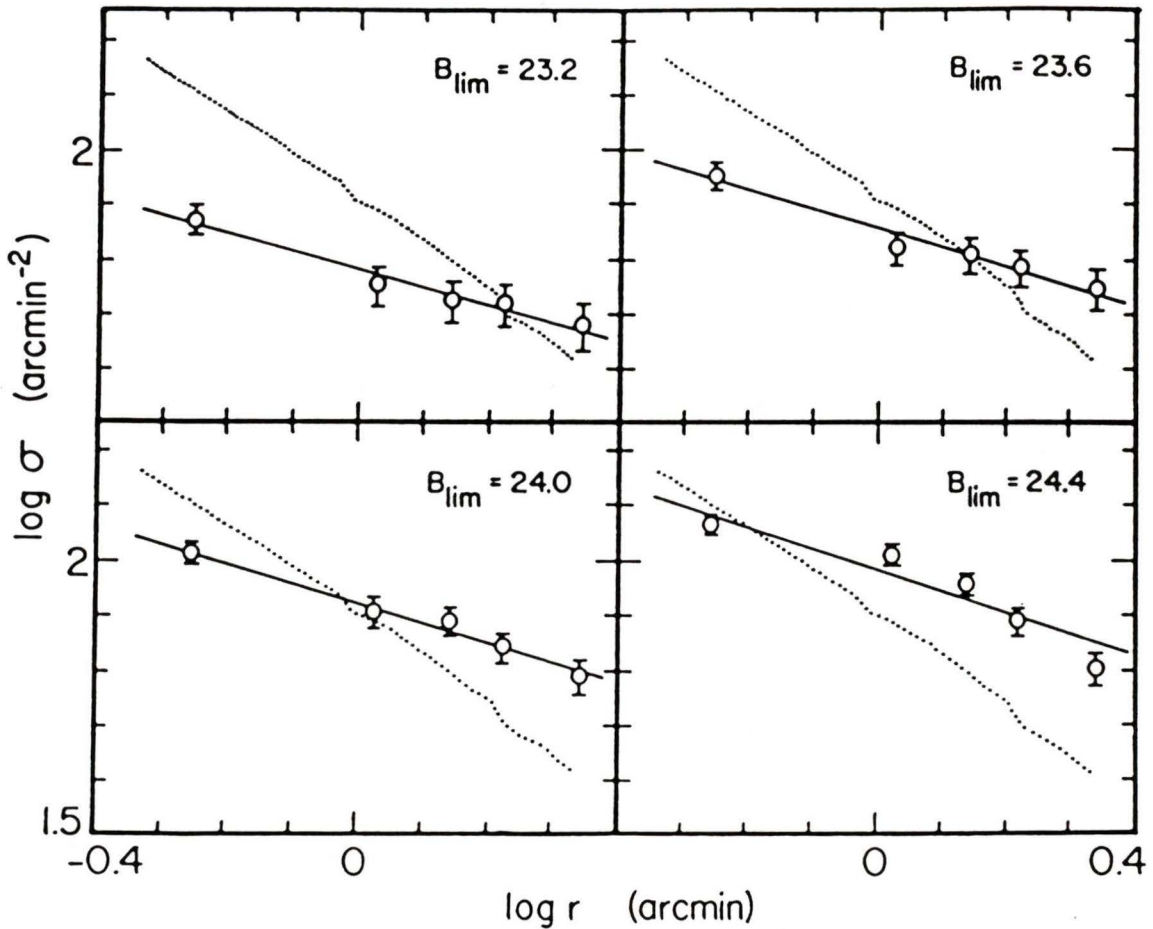


Figure 12. Integrated surface density profiles for various limiting magnitudes. The solid lines represent best-fit linear relations for each limiting magnitude, and have slopes -0.67 , -0.69 , -0.71 , and -0.77 for limiting magnitudes $B = 23.2$, 23.6 , 24.0 , and 24.4 , respectively. The dotted line corresponds to the M87 luminosity profile measured by Davis et al. (1985), and has a slope of ~ -1.6 in the panels above. Error bars include both \sqrt{N} statistics and the uncertainty due to completeness corrections.

consideration. The errors indicated in Table 9 and Figure 12 were calculated by combining in quadrature the uncertainty estimated from \sqrt{N} statistics and the mean errors of the completeness correction in each zone as given in Table 7. The halo light has been arbitrarily normalized to the globular cluster surface density so that the surface brightness at a projected radius of one arcminute corresponds to $\log \sigma = 1.8$.

It is evident from Figure 12 that there is indeed a discrepancy between the slopes of the globular cluster surface density profiles and the halo light. Over the radial range $20'' < r < 160''$, a least-squares power-law fit to the cluster data gives radial dependences which go as $r^{-(0.77 \pm 0.1)}$, $r^{-(0.72 \pm 0.1)}$, $r^{-(0.69 \pm 0.12)}$, and $r^{-(0.67 \pm 0.14)}$ for limiting magnitudes of $B = 24.4$, 24.0 , 23.6 , and 23.2 , respectively. These power laws agree with one another to within their formal uncertainties and thereby reaffirm the previous conclusion that there appears to be no conclusive evidence for a systematic variation of the globular cluster luminosity function with radius. For a limiting magnitude of $B = 22.8$, a logarithmic slope of 0.77 ± 0.16 is determined and suggests that the possible trend in the power-laws above is probably not real.

The surface density profile shown in Figure 12 for $B_{lim} = 24.4$ seems to indicate an apparently significant central depression of the inner two data points, analogous to the central "hole" in the globular cluster surface density found by Harris et al. (1984) in NGC 4594. On the other hand, the fact that this depression does not appear so

pronounced for brighter limiting magnitudes, combined with the lack of a statistically significant trend in the luminosity function with radius, indicates that this feature is probably not significant.

In Figure 13, the radial distribution found in the present study has been compared with the surface densities of Harris and Smith (1976), as revised by Harris (1985). For the sake of comparison, the effective radius of each zone has been approximated by $(r_1 r_2)^{1/2}$ (Harris 1985), where r_1 and r_2 are the inner and outer radial limits to the zone concerned (see Table 8).

A realistic comparison, however, requires that the surface densities of the two samples be integrated over the same range of brightness. There is some question as to the limiting magnitude of the 1976 survey, which was originally assigned a value of $B_{lim} = 23.8 \pm 0.5$. Harris and van den Bergh (1981) have more recently determined a value of $B_{lim} = 24.5$ from a comparison of a model-calculated background/foreground object density with the surface density actually found by Harris and Smith. Harris (1985) has adopted a value of $B_{lim} = 24.0 \pm 0.3$ as a reasonable compromise between these two.

An additional problem concerns the possible variation of limiting magnitude with decreasing radius due to a combination of "preflashing" of the photographic emulsion by the strong halo background and the difficulty of distinguishing the fainter objects against this background. Given that Harris (1985) finds a mean surface density of $47.11 \text{ arcmin}^{-2}$ in the region from one to two arcminutes from the

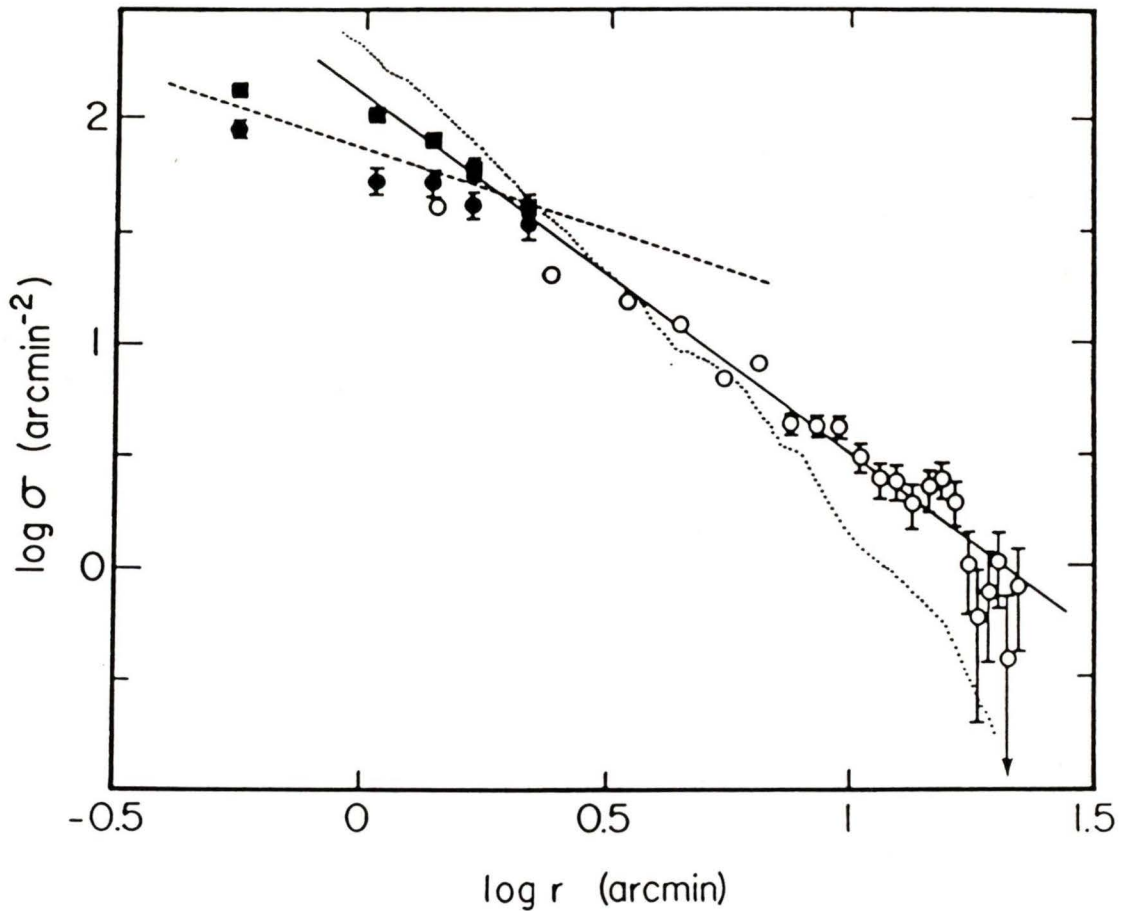


Figure 13. Surface density profile of M87 globular clusters to $r \sim 22$ arcminutes. The hollow circles represent surface densities taken from Harris (1985). The filled circles correspond to the present sample of globular clusters integrated to $B = 23.8$, while the squares correspond to an integration to $B = 24.4$. The solid line is a fit determined by Harris (1985) for data at $r > 4$ arcminutes and has a slope of -1.61 . The dashed line has a slope of -0.72 and represents a mean fit to the present data. The dotted line corresponds to the M87 luminosity profile determined by de Vaucouleurs and Nieto (1978).

nucleus of M87, a straight forward integration of the present data to various limiting magnitudes in a similar annulus yields a most likely value of $B_{lim} = 23.8$, for which is found $\sigma = 47.14 \text{ arcmin}^{-2}$. If, however, the innermost two points of the data of Harris and Smith (1976) are low due to incompleteness as Harris (1985) suspects, then a meaningful comparison of the present observations with the data at greater radii would require the adoption of a somewhat fainter limiting magnitude.

In Figure 13, the present data is shown for assumed limiting magnitudes of $B = 23.8$ and $B = 24.4$, which are taken to represent the likely limits of uncertainty. Also shown is the least squares relation:

$$\log \sigma = (2.12 \pm 0.06) - (1.61 \pm 0.08) \log r \quad (7)$$

(in units of arcmin and arcmin^{-2}) determined by Harris (1985) for the data at $r > 4$ arcminutes. The dashed line corresponds to the power-law relation:

$$\log \sigma = 1.88 - (0.73 \pm 0.16) \log r \quad (8)$$

where the slope is a mean of the slopes calculated for limiting magnitudes 23.8 and 24.4, and the normalization is arbitrary. The dotted line in Figure 12 corresponds to the M87 luminosity profile

measured by de Vaucouleurs and Nieto (1978), arbitrarily normalized so that the surface brightness at $\log r = 0.5$ corresponds to $\log \sigma = 1.3$.

It is evident both from Figure 13 and the relations given above that the surface density profile suggested by the present data is significantly shallower than the optimal fit found by Harris (1985) for the data at larger radii. Indeed, even allowing for the uncertainty in limiting magnitude, the surface density of clusters found in zone 1 of the present study is at least a factor of two lower than that suggested by equation (7). Rather tantalizingly, for an assumed limiting magnitude of $B = 24.4$, the outer three points of the present sample fall right along the relation (7) of Harris (1985), so that the inner two data points once again seem to imply a central "hole" in the distribution. This tendency does not appear obvious for $B_{lim} = 23.8$, however, and the fit of the outer three points is likely fortuitous. Regardless of the exact curvature, however, the present data indicate that the surface density profile is somewhat flatter for $r < 2$ arcminutes, and possible causes and implications of this leveling off will be discussed in Chapter 5.

The data shown in Figure 13 (minus the two innermost points of Harris (1985)) were fitted in a least-squares sense to give the de Vaucouleurs laws:

$$\log \sigma = (3.75 \pm 0.051) - (1.81 \pm 0.035)r^{1/4} \quad (9)$$

and

$$\log \sigma = (3.34 \pm 0.059) - (1.56 \pm 0.039)r^{1/4} \quad (10)$$

for assumed limiting magnitudes of $B = 24.4$ and $B = 23.8$, respectively. r is taken here to be in arcminutes, and the corresponding effective radii (i.e. the radii within which are contained half the total number of clusters in projection) are (20.6 ± 2.1) and (11.5 ± 0.9) arcminutes, respectively. The formal errors are rather meaningless in this instance, and the uncertainty in the actual shape of the globular cluster distribution is completely dominated by the uncertainty in the limiting magnitude of the sample of Harris and Smith (1976). A comparison of the present data with the radial distribution of M87 globulars determined to $B = 22.5$ by Strom et al. (1981) is shown in Figure 14. Since only 90 objects were found in the frame with magnitudes brighter than this limit, the error bars for the surface densities in the five bins are correspondingly large. A realistic comparison is more easily made by dividing the present sample into two radial bins as shown by the filled-in circles in Figure 14. Though the slope of the present data does appear to be somewhat shallower than that seen in the observations of Strom et al., the large error bars combined with the small number of points do not rule out overall consistency with a power-law of the form $\sigma \propto r^{-1.1}$ fitted to the Strom data exclusively. This is to be compared with a best-fit power-law of the form $\mu \propto r^{-2.2}$ for the halo profile of de Vaucouleurs and Nieto (1978).

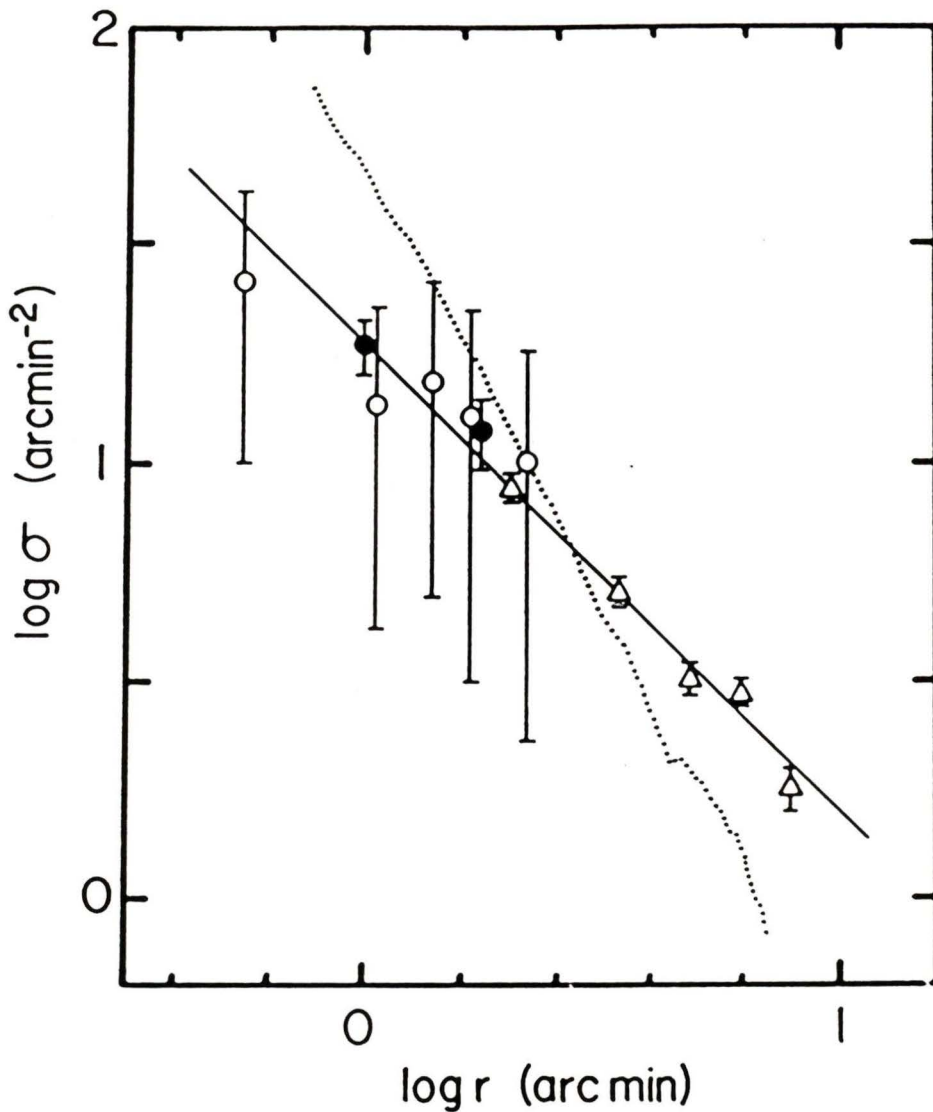


Figure 14. Surface density profile determined from the present sample compared with that of Strom et al. (1981). The solid line has a slope of -1.1 and is a fit to the data of Strom et al. (triangles). The hollow circles represent mean surface densities determined from the present data for five concentric zones, while the filled circles result from binning the data into only two radial regions. The dotted line corresponds to the M87 luminosity profile of de Vaucouleurs and Nieto (1978) and has a slope of -2.2 in this figure.

4.5 The Total Number of Globular Clusters in M87

Integrating the relations given in (9) and (10) above from 0 to 20 arcminutes gives total numbers of globular clusters of 5120 and 4840, respectively. The number of globulars predicted by these relations to reside within the 20 arcsecond inner limit of the present sample is approximately 100 ± 30 . There is as yet considerable uncertainty as to the total radial extent of M87's cluster system (Harris and Smith 1976, 1981; Harris 1985), and though there is no a priori reason to believe that the de Vaucouleurs laws (9) and (10) should hold for larger radii, integrating these relations to a projected radius of one degree (Arp and Bertola 1969) predicts an additional 1900 and 2900 clusters, respectively.

In order to calculate the total number N_t of globular clusters around M87, one must assume some form for the luminosity function of clusters at inaccessible magnitude levels. A more or less symmetrical Gaussian-like form has been found empirically to prevail in Local Group galaxies (Harris and Racine 1979), but as pointed out in Chapter 3: a) M87 is not a spiral galaxy; and b) its observed cluster distribution apparently does not follow a Gaussian with $\sigma = 1.2$. Consequently, there is no compelling reason to believe that the M87 globular cluster luminosity function is Gaussian or even symmetrical. Nonetheless, in the interests of making an "educated guess" at N_t , a Gaussian form of the luminosity function is assumed for which $B_0 = 25.64$ and $\sigma = 1.89$ as determined in Chapter 3. Over the ranges $20 < B$

< 30 and $0 < r < 20'$, this gives $N_t = 29000$ and 20000 for $B_{lim} = 23.8$ and 24.4 , respectively. If B_0 and σ are assumed to have values of 25.0 ± 0.3 and 1.5 as suggested in Paper I, N_t is found to lie between 15000 and 23000 . If the uncertainty in B_0 is included along with the uncertainties in the radial extent of the cluster system and the limiting magnitude of Harris and Smith's sample, then N_t may be constrained only to within the region $12000 < N_t < 48000$. And this does not consider the uncertainties in the shape of the luminosity function! Nonetheless, even the lower bound is indicative of an enormous number of globular clusters when compared with the typical quantities found in other galaxies (Harris and Racine 1979). Assuming that the number of globular clusters associated with a given galaxy is correlated with the galaxy's total luminosity (which in turn is assumed to depend on the galaxy's mass), Harris and van den Bergh (1981) have defined a quantity called the specific frequency S of globular clusters, so that:

$$S = N_t 10^{0.4(15 + M_V)} \quad (11)$$

If we take the luminosity of M87 to correspond to $M_V = -22.47$ at an assumed distance of 16.5 Mpc (de Vaucouleurs et al. 1976), then the allowed range in N_t above gives $12.3 < S < 49$. For the two "best" values of N_t corresponding to $B_{lim} = 23.8$ and 24.4 , S is found to be 21 and 30 , respectively. Assuming a limiting magnitude for Harris and

Smith's (1976) sample of 24.0 and a distance to M87 of 16 Mpc, Harris (1985) determines a value of $N_t = 12000$ and finds the specific frequency to lie in the range $10 < S < 17$. The larger values found here are a direct result of the shallowness of the globular cluster surface density profile at small radii as determined from the present data. This has the effect of increasing the effective radii (the radii within which are contained half the total number of clusters in projection) in (9) and (10), so that the number of observed globular clusters represents a smaller fraction of the total.

4.6 Non-radial Distribution of Surface Density

Having found that the radial surface density profile of globular clusters differs in shape from the stellar luminosity profile, a check was made of the angular distribution of clusters within the frame to determine whether or not the ellipticity of the isophotes was reflected in their surface densities. To this end, the frame was divided into four sectors of equal area as shown in Figure 15. Completeness tests as a function of position angle were made using the object list in Table 4, where the positional and magnitude tolerances were specified as before. Applying these completeness corrections, subtracting the appropriate background, and integrating the magnitude distribution of globulars to $B = 24.4$, a crude angular surface density

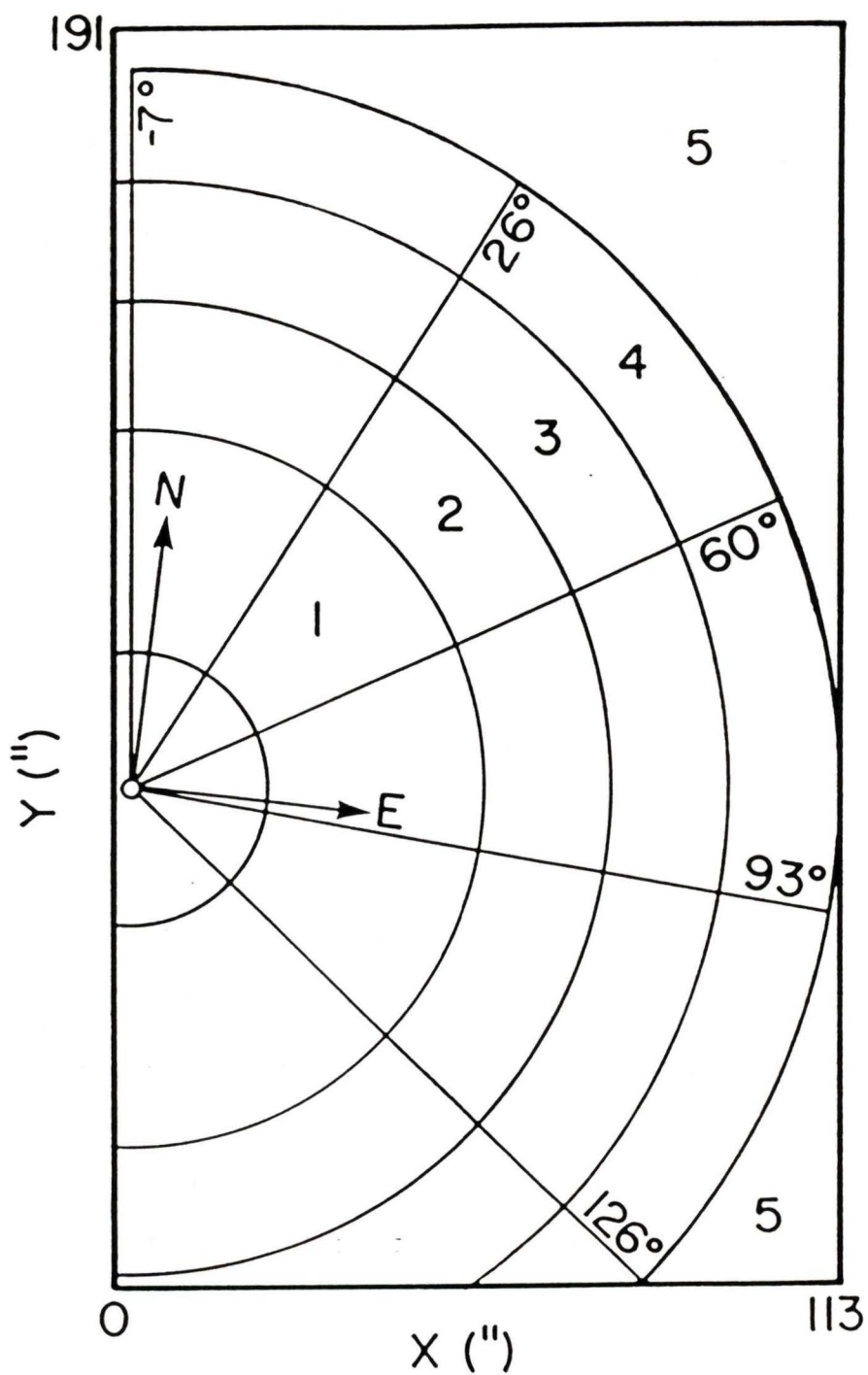


Figure 15. A scaled representation of the M87 field under study. Shown are the areas corresponding to each zone, as well as the four sectors used to look for non-radial surface density variations.

profile was constructed as shown in Figure 16. This figure also shows the variation in the mean background intensity (adding in the previously subtracted de Vaucouleurs law but not the "sky") determined for the four angular areas from the "cleaned" frame used previously in the investigation of spurious images.

The variation of counted clusters with position angle is not large in relation to the size of the errors, consistent with the fairly circular isophotes in the inner regions of M87 (Carter and Dixon 1978; de Vaucouleurs and Nieto 1979; Boroson et al. 1983). This suggests that the numbers of globular clusters found in the last section are probably not skewed significantly due to coverage of only a limited arc around the nucleus. From the angular intensity profile, the minor axis of the background light would appear to lie somewhere between 40° and 60° , in agreement with the luminosity profiles of Arp and Bertola (1969), Carter and Dixon (1978), and Davis et al. (1985). Both the present data and the cluster distribution of Harris and Smith (1976) show a similar orientation, with the much larger variation in the observations of Harris and Smith being consistent with the increasing ellipticity seen in M87 isophotes with increasing radius. It would be interesting to have CCD coverage for the remaining arc around M87, so that by identifying a similar surface density minimum at a position angle of around 240° , one might substantiate the reality of the minimum found here. One would then be led to conclude that, at least in this respect, the distribution of globular clusters around M87 mirrors that of the halo stars, and the dynamical histories of the

two components will perhaps have had at least some things in common.

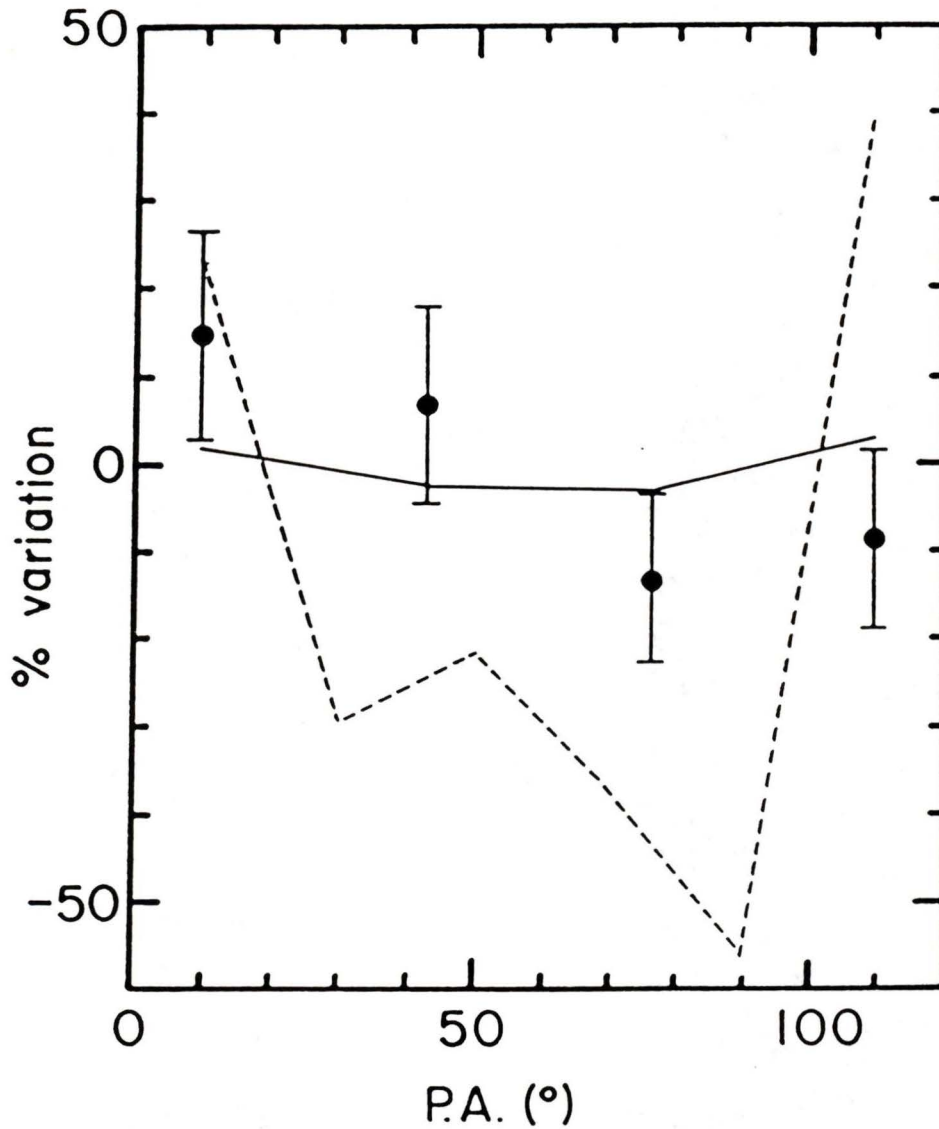


Figure 16. The variation of surface density with position angle. The filled circles correspond to the present data integrated to $B = 24.4$, and the error bars include both \sqrt{N} statistics and the uncertainty due to completeness corrections. The solid line represents the variation in intensity of the "background" light in the M87 frame, and the dashed line corresponds to the globular cluster data of Harris and Smith (1976).

CHAPTER 5

DISCUSSION

Having established the apparent distention of M87's globular cluster envelope relative to its luminosity profile as well as the possible levelling off of cluster surface densities at small radii, it is of interest to calculate models which might shed some light on the current dynamical state of the cluster system.

5.1 A Simple Analytic Density Profile

If we consider M87's globular clusters to be a system of test particles, then using the simple analogies described by Zwicky (1957), we may regard the cluster system as an ideal gas with partial pressure P so that:

$$P = NkT$$

where N is the number density and k is Boltzmann's constant. In this

case, the temperature is more appropriately replaced by the average translational energy of the clusters:

$$\frac{1}{2}m\sigma_3^2 = \frac{3}{2}kT \quad (13)$$

where σ_3 is the assumed-isotropic, three-dimensional velocity dispersion, so that (12) becomes:

$$P = \frac{1}{3}\rho\sigma_3^2 \quad (14)$$

If we consider the system to be in hydrostatic equilibrium with respect to its partial pressure, then:

$$\frac{dP}{dr} = - \frac{\rho GM(r)}{r^2} \quad (15)$$

where G is the gravitational constant and $M(r)$ is the total mass interior to some radius r . If, in the first instance, we consider the case of an isothermal sphere and consequently neglect radial changes in the velocity dispersion, then from (14):

$$\frac{dP}{dr} = \frac{1}{3}\sigma_3^2 \left(\frac{d\rho}{dr} \right) \quad (16)$$

so that integrating (15):

$$\rho_0 \int_{\rho}^{\rho_0} \frac{d\rho'}{\rho'} = \frac{-3G}{\sigma_3^2} r_0 \int_{r_0}^r \frac{M(r')}{r'^2} dr' \quad (17)$$

one arrives at:

$$\rho(r) = \rho_0 \exp\left[\frac{-3G}{\sigma_3^2} r_0 \int_{r_0}^r \frac{M(r')}{r'^2} dr'\right] \quad (18)$$

where r_0 is some arbitrary reference radius and ρ refers to the density of the test particles under consideration. While this "derivation" is intended to be merely illustrative, equation (18) expresses exactly the density profile predicted by a more rigorous treatment using the Vlasov equation.

5.2 Distribution of Mass in M87

The calculation of the run of globular cluster densities with radius requires the evaluation of the integral in the exponential of equation (18) and consequently some idea of the total mass distribution in M87. For the inner regions of M87, the distribution

of surface density has been approximated using the $r^{1/4}$ law determined by de Vaucouleurs and Nieto (1978) for the luminosity profile:

$$\mu = 14.615 + 2.658r^{1/4} \quad (19)$$

where μ is in B mag arcsec⁻², r is in arcseconds, and the corresponding effective radius r_e is 96 arcseconds. This profile has been deprojected using the expansion of Young (1976):

$$\tilde{\rho}(s) \approx 0.0461 \exp[-bs^{1/4}] (2s)^{-3/4} \left(\frac{\pi}{8bs^{1/4}} \right)^{1/2} \left[1 - \frac{7}{8bs^{1/4}} + \frac{0.6}{(bs^{1/4})^2} \right] \quad (20)$$

where $b = 7.66924944$ and $s = r/r_e$. Although this is an asymptotic expansion for $s \rightarrow \infty$, it is accurate to better than 3% down to $s = 0.001$, which is well below the region $0.2 < s < 12$ of interest here. The density in units of $M_\odot \text{pc}^{-3}$ may be computed by multiplying the dimensionless reduced density by the appropriate scale factors:

$$\rho(r) = \frac{\tilde{\rho}(s)M_t}{r_e^3} \quad (21)$$

where the effective radius is now in parsecs, and the total mass M_t of the stellar component has been determined by simply integrating equation (19) and assuming a constant mass-to-light ratio. A distance

to M87 of 15 Mpc has been assumed for these calculations, giving $1'' = 72.6$ pc.

For the outer regions of M87's halo, an estimate of the mass distribution is provided by the X-ray observations of Fabricant and Gorenstein (1983). Assuming that the X-ray emitting gas is isothermal and in hydrostatic equilibrium, these investigators have modelled the density distribution of the binding mass as:

$$\rho(r) = \rho_0 \left[1 + \left(\frac{r}{r_a} \right)^2 \right]^{-p} \quad (22)$$

where ρ_0 is the extrapolated central density and r_a is the core radius. The best-fit values of r_a and p using the X-ray surface brightness profile were found to be 1.6 ± 0.28 arcminutes and 0.654 ± 0.012 , respectively.

This run of volume density, along with that calculated from the de Vaucouleurs law, was integrated numerically from 0.01 to 200 kpc to approximate the mass of M87 as a function of radius. The mass-to-light ratio for the luminosity profile of de Vaucouleurs and Nieto (1978) was varied in order to achieve correspondence with the masses determined by Sargent et al. (1978) using the observed variation of velocity dispersion with radius in the inner 72 arcseconds of M87. The data of Sargent et al., along with the mass determined from integrating the deprojected de Vaucouleurs law, are shown plotted in Figure 17, where a constant mass-to-light ratio of $8 M_\odot/L_\odot$ has been

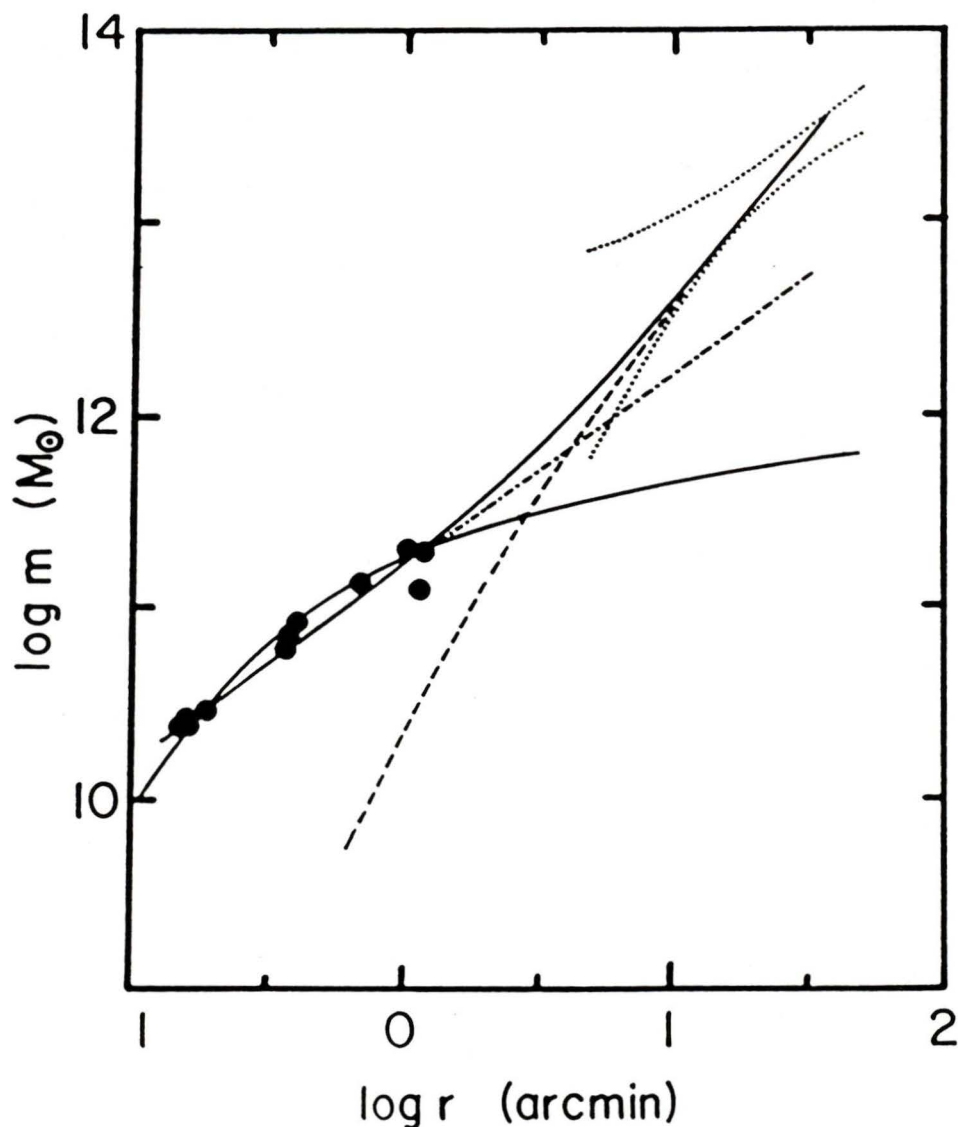


Figure 17. The mass profile of M87. The dashed curve corresponds to the mass determined by the X-ray observations of Fabricant et al. (1980), which is added to the mass determined by deprojecting the de Vaucouleurs law to give the total mass profile shown by the upper solid curve. The dotted lines correspond to the mass limits set by Fabricant and Gorenstein (1983). The lower solid curve corresponds the density model of Binney and Cowie (1981), and the dash-dot line represents an isothermal sphere. The filled circles correspond to the results of observations by Sargent et al. (1978).

assumed to achieve the fit shown. In the outer halo of M87, the central density in equation (22) was allowed to vary in order that the calculated mass fell within the limits determined by Fabricant and Gorenstein, shown as dotted lines in Figure 17. These mass limits correspond to the results of calculations by Fabricant and Gorenstein using models in which the X-ray temperature profile (not well defined by their data) was assumed to have a power-law form wherein the exponent was varied from -0.4 through $+0.9$.

There has been considerable debate as to whether the X-ray emitting gas in the outer halo of M87 may in fact be considered to be in hydrostatic equilibrium. Binney and Cowie (1981) have postulated that, rather than being gravitationally restrained, the X-ray emitting gas may be confined by external pressure from a hot (10^8 K) tenuous atmosphere associated with the Virgo cluster as a whole. In addition, since the cooling time of the X-ray emitting gas within about 10 arcminutes from M87 is shorter than a Hubble time, a steady-state cooling flow would be expected to have been established in this region.¹ They find that the X-ray surface-brightness observations of Fabricant et al. (1980) can be well-fitted for all radii out to 100 kpc by a model in which radiative cooling generates inward mass flow

¹ This latter possibility should not affect the present considerations significantly since the mass at radii < 10 arcminutes is determined predominantly from the stellar luminosity profile.

rates of around $10 M_{\odot} \text{ yr}^{-1}$. For the relatively steep temperature gradient which they assumed, they determined the core radius of the binding mass distribution to be of order 250 kpc, suggesting a likely association with the intergalactic medium of the Virgo cluster rather than with M87 itself. The importance of this alternative view resides in the fact that this model predicts a total mass of M87 out to 100 kpc of only $5 \times 10^{11} M_{\odot}$, which is almost two orders of magnitude less than the mass predicted assuming gravitational association of the gas with M87.

Stewart et al. (1984) have been able to improve constraints on the temperature gradient of the gas surrounding M87 with more recent Einstein observations, and models used to reproduce the observed line strengths indicate a likely core radius closer to 25 kpc. This is in much better agreement with the results of Fabricant and Gorenstein, and the cooling flow required in the inner regions has been reduced to a more reasonable $1 M_{\odot} \text{ yr}^{-1}$. In a recent survey, Forman, Jones, and Tucker (1985) have found hot, X-ray emitting, gaseous coronae to be a common occurrence among early-type galaxies, even those far removed from the atmosphere thought to pervade the central regions of the Virgo cluster. These coronae are interpreted as being the long-sought accumulation of matter generated during normal stellar evolution (Faber and Gallagher 1979), prevented from becoming a galactic wind by the gravitation of the parent galaxy (Norman and Silk 1979), and

heated by energy liberated in supernovae. These galaxies are removed from the centers of rich clusters where pressure confinement could significantly affect the density and temperature profiles of the X-ray emitting gas, and yet masses of up to $5 \times 10^{12} M_{\odot}$ are determined. Consequently, there is reason to suppose that M87 should be surrounded by a fairly massive halo of its own.

For the sake of comparison, mass profiles were generated using both the density function of Binney and Cowie and the mass limits determined by Fabricant and Gorenstein. Binney and Cowie assume for M87 a run of density as given by equation (22), with values for r_a of 700 pc, $\rho_0 = 0.26 M_{\odot} \text{pc}^{-3}$, and $p = 3/2$, as determined from the photometry of Sargent et al. (1978) and the line-of-sight velocity dispersion measured by Young et al. (1978). This function has been integrated numerically and is shown plotted in Figure 17. Step sizes of 1 pc were used for all integrations represented in this figure, and a table of density, mass, and potential as a function of radius was generated once and for all for use in subsequent calculations.

5.3 Isotropic, Single-Component Model

In order to compare the expected numbers of globular clusters with the surface densities determined in the last chapter, equation (18) must be projected along the z-axis (line-of-sight) onto the plane of the sky. Assuming a spherical distribution, the appropriate integral may be expressed as:

$$\rho(x,y) = 2 \int_0^{\infty} \rho([r^2 + z^2]^{1/2}) dz \quad (23)$$

where the actual integration was performed numerically using step sizes of 50 pc to an assumed outer limit of 200 kpc. As a check for consistency, surface densities were calculated using both the Fabricant and Gorenstein mass model as well as that of Binney and Cowie for an input line-of-sight velocity dispersion of 280 km sec^{-1} as measured by Young et al. (1978). Over the radial range examined by Young et al., the falloff in the calculated surface density in both cases did not differ significantly from the slope of the luminosity profile in this region determined by de Vaucouleurs and Nieto (1978).

In Figure 18 are shown once again the surface densities determined by Harris (1985) and those calculated here, where only the data for $B_{1im} = 23.8$ has been plotted so as not to clutter the diagram excessively. Superposed are curves which represent the expected run of surface density with projected radius assuming an

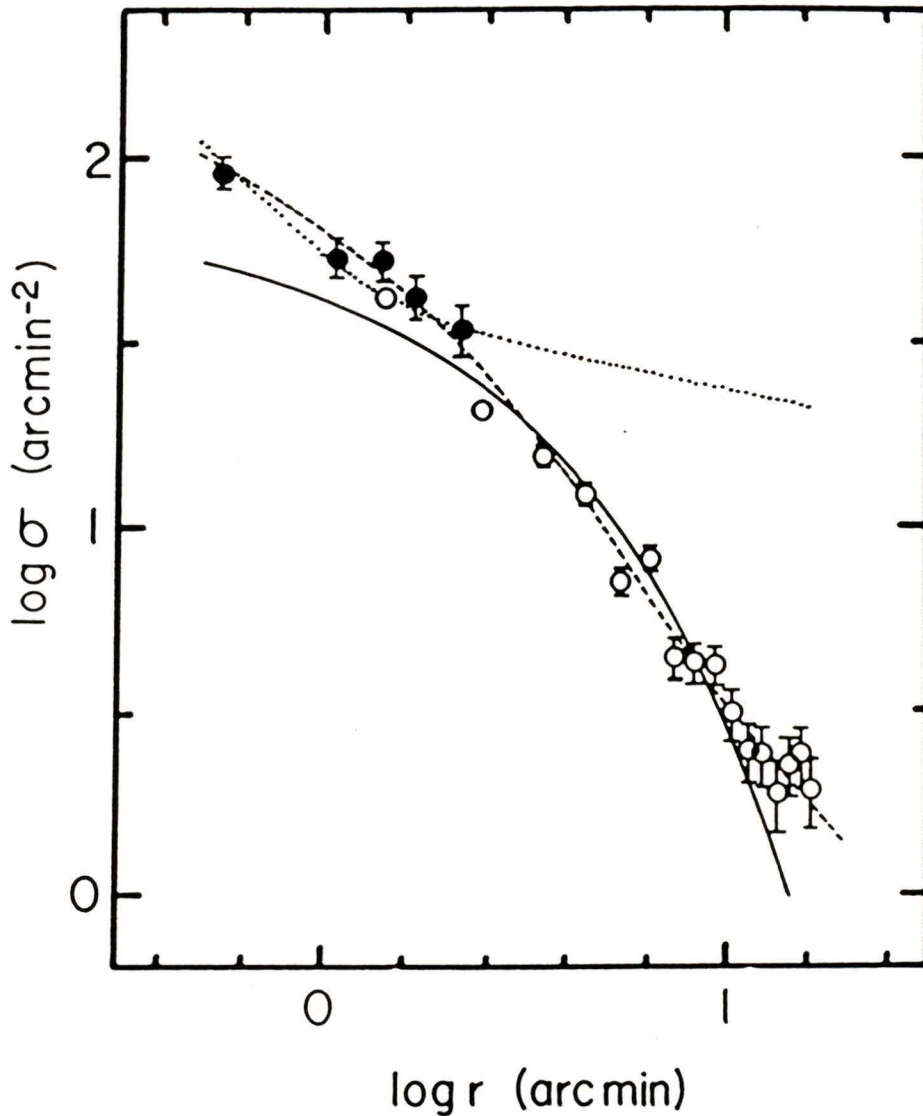


Figure 18. Surface densities predicted by models assuming isotropic velocity dispersions. The hollow circles represent the data taken from Harris (1985) and the filled circles correspond to the present sample, integrated to $B = 23.8$. The solid curve assumes a homogeneous cluster population using the mass model of Fabricant and Gorenstein (1980), while the dotted curve represents a similar calculation assuming the lower-mass model of Binney and Cowie. The dashed curve results for a cluster population which is assumed to consist of two kinematically distinct subcomponents.

isotropic velocity distribution with a radially constant dispersion.

Using Fabricant and Gorenstein's model for the mass distribution, a fit to the data was generated by minimizing χ^2 for assumed limiting magnitudes of 23.8 and 24.4, respectively. The data used for the fits included all points in the present study, but not the data of Harris (1985) for radii greater than 16 arcminutes due to the large uncertainties in this region. In addition, the two innermost points of Harris's sample were dropped from consideration owing to Harris's suspicion that they might suffer significantly from incompleteness. The fit to the remaining 19 points is shown as the solid curve in Figure 18, for which $\sigma_3 = 734 \pm 21 \text{ km sec}^{-1}$. A similar fit for an assumed limiting magnitude of $B = 24.4$ requires a value for σ_3 of $670 \pm 21 \text{ km sec}^{-1}$. The errors have been estimated by treating the normalizing surface density as the "uninteresting" parameter (Avni 1976) and defining a range of acceptable velocity dispersions as those for which $\chi^2 < \chi^2_{\text{min}} + 2.71$, corresponding to the 90% confidence interval (Lampton et al. 1976).

It is evident from the figure that the fitted curve does not represent the data particularly well. The suggestion seems to be that: a) rather than remaining constant, the velocity dispersion of the clusters might increase with radius; b) the orbits become progressively more radial at larger galactocentric distances; or c) M87's mass profile is not as steep as the X-ray observations would suggest. These conclusions rely on the premise that, since clusters

on eccentric orbits spend more of their time at larger radii, the run of volume density reflects in turn the distribution of orbital apocenters. A velocity dispersion which either increases or becomes more radial with increasing radius would therefore produce the surface densities required by the data at large projected radii without depleting the cluster population in the inner regions. Intuitively, one could regard radial orbits as exerting a strong outward "pressure" which would produce a distribution somewhat more extended than one resulting from purely circular orbits. The reader is referred to Binney (1981, p. 62) for a discussion and graphical depiction of the effects of a radial gradient in the velocity dispersion on the density profile.

The difference in the best-fit velocity dispersions for the cases corresponding to the two assumed limiting magnitudes requires that an overall uncertainty in the likely velocity dispersion be somewhat greater than the formal fitting error. Consequently, if the anisotropy of the velocity field is not too severe, and if the dispersion does not vary significantly with radius, then the likely line-of-sight velocity dispersion for the globulars considered here lies in the range 320 to 430 km sec⁻¹ for an assumed homogeneous population.

The dotted curve in Figure 18 represents the expected run of surface density with projected radius for a gravitational potential calculated assuming the density model of Binney and Cowie (1981). It is evident that by fitting this curve to the data of Table 9 ($\sigma_3 = 450$

km sec⁻¹), the surface densities predicted at larger radii are much greater than the probable errors in the observations of Harris and Smith (1976) allow. Moreover, the logarithmic slope in the inner regions is here predicted to be steeper than the falloff at larger radii, in contrast to the reversed situation apparent in the data. This is due to the more rapid falloff with radius of the calculated gravitational potential, and has an effect on the expected surface density similar to that produced by substantially increasing the velocity dispersion at larger radii using the mass distribution of Fabricant and Gorenstein. Consequently, the velocity dispersion of the globular clusters must decrease significantly with increasing radius if a reasonable fit to the data is to be achieved with the Binney and Cowie model under the current assumption of isotropy.

5.4 Isotropic, Two-Component Model

It is tempting to speculate on the existence of a cluster system containing two or more distinct components with different velocity dispersions. One component might be associated with, say, a population of clusters indigenous to M87, while another component might consist of globulars which were stripped from the halos of smaller, passing galaxies sometime in the past (Forte et al. 1982; Muzzio et al. 1984). The dashed curve in Figure 18 shows the expected

run of surface density for such a two component model, in which three-dimensional velocity dispersions for the inner and outer components of 600 ± 25 and $1284 (1045 \rightarrow 2000)$ km sec^{-1} have been determined by searching for χ^2_{min} in a four-dimensional parameter space. The surface densities are approximately equal at a projected radius of 9.3 arcminutes, where $\sigma = 1.7 \text{ arcmin}^{-2}$ for each component. The reduced χ^2 value for this fit is 1.4 for 15 degrees of freedom, as opposed to corresponding values of 6.9 and 13.6 for the single-component models above. The errors have again been estimated by varying each "interesting" parameter individually to determine appropriate limits corresponding to the 90% ($\Delta\chi^2 = 4.61$) confidence interval.

For the case where the limiting magnitude of the sample is assumed to be 24.4, best-fit three-dimensional velocity dispersions of 554 ± 16 and 1220 ± 300 km sec^{-1} are found for the inner and outer components, respectively. The reduced χ^2 value for this fit is 2.6, indicating considerably less agreement with the two-component model than for $B_{\text{lim}} = 23.8$, and relies heavily on the deletion of Harris's inner two data points. In any event, it must be emphasized that postulating a system of two kinematically distinct subcomponents is a rather ad hoc way to improve the goodness-of-fit, and many other four-parameter models could as easily be made to agree with the observations.

5.5 The Effect of a Velocity Anisotropy

Due to the low spatial density of globular clusters, cluster-cluster encounters are sufficiently rare that the corresponding two-body relaxation time considerably exceeds the age of the universe. Numerical investigations have shown that for a variety of assumed initial conditions, the collapse phase of spherical systems such as M87 must involve significant numbers of objects with binding energies near zero (highly radial orbits) if M/L is assumed constant and agreement is to be achieved with the observed $r^{1/4}$ luminosity profiles (Binney 1982b). N-body simulations by van Albada (1982) suggest that this strong radial bias in the velocity dispersion of objects in the galactic halo is largely preserved during the violent relaxation phase (Lynden-Bell 1967), so that the presently observed configuration of ellipticals is probably indicative of conditions at the time of their collapse (Binney 1982a). When one considers that: a) M/L for globular clusters is not likely to vary significantly with radius; b) cluster surface densities can be reasonably fitted by an $r^{1/4}$ profile; and c) the timescale for violent relaxation is independent of mass, one is led to conclude that the distribution of M87 globular clusters in velocity space should exhibit a significant anisotropy.

Since M87 appears to be fairly circular in projection, exhibits relatively little rotation (Sargent et al. 1978), and its cluster system seems to reflect this symmetry as well (see Chapter 4), there is some justification for assuming a spatially spherical cluster

distribution. If we assume that the major axis of the velocity ellipsoid is everywhere directed towards the galactic center and the other two axes are orthogonal and of equal length, then the first moment of the collision-less Boltzmann equation may be written (Binney 1981):

$$\frac{1}{\rho} \frac{d}{dr}(\rho \sigma_r^2) + \frac{2\beta \sigma_r^2}{r} = -G \frac{M(r)}{r^2} \quad (24)$$

where the anisotropy parameter is defined as:

$$\beta = 1 - \frac{\sigma_t^2}{\sigma_r^2} \quad (25)$$

and σ_r and σ_t are the radial and tangential components of the velocity dispersion, respectively. If we allow the anisotropy to vary with radius and assume the mathematically convenient form:

$$\sigma_t^2 = \frac{\sigma_r^2}{1 + \left(\frac{r}{r_\beta}\right)^2} \quad (26)$$

then:

$$\beta(r) = \frac{1}{\left(\frac{r_\beta}{r}\right)^2 + 1} \quad (27)$$

where we will call r_β an anisotropy radius. Equation (24) may be integrated to yield:

$$\rho(r) = \rho_0 \left[\left(\frac{\sigma_r}{\sigma_0}\right)^2 \left(\frac{r_0^2 + r_\beta^2}{r^2 + r_\beta^2}\right) \right] \exp\left[-G \int_{r_0}^r \frac{M(r')}{r'^2 \sigma_r^2} dr'\right] \quad (28)$$

where $M(r)$ is taken from the tables generated for the mass models of Fabricant and Gorenstein and Binney and Cowie, respectively.

If we examine first the simple case in which σ_r is assumed to remain constant with radius, then the integral becomes simply the gravitational potential contained in the tables. This function was projected onto the plane of the sky, and σ_r , r_β , and ρ_0 were constrained using the least-squares technique discussed previously. For an assumed limiting magnitude of $B = 23.8$, a minimum χ^2 value was found for the combination of "interesting" parameter values $\sigma_r = 1132$ km sec⁻¹ and $r_\beta = 2.9$ kpc, where the allowed ranges corresponding to the 90% confidence interval extend from 1010 to 1320 km sec⁻¹ and 2.0 to 4.0 kpc, respectively. The reduced χ^2 value for this fit is 1.6, which is about as good as the fit found in the isotropic case under the assumption of two kinematically distinct cluster populations. For an assumed limiting magnitude of $B = 24.4$, the parameters

corresponding to a reduced $\chi^2_{\min} = 3.6$ were found to be $\sigma_r = 942$ (870 \rightarrow 1045) km sec^{-1} and $r_\beta = 1.9$ (1.1 \rightarrow 2.6) kpc, respectively.

The similarities in the goodness-of-fit determined for the two-component and the anisotropic models suggest that the former can mimic the surface density distribution of the latter, and the available data does not allow firm constraints to be placed on the reality of either. Nonetheless, the anisotropic model probably corresponds more closely to the actual distribution for the following reasons. a) The model achieves a fairly good fit to the data with only three assumed parameters. b) Models for protogalactic collapse generally favour highly radial orbits which persist through the violent relaxation phase. c) Binney and Mamon (1982) have calculated self-consistent models for the run of luminosity and velocity dispersion in M87 which require $\beta = 0.4$ or higher for the stellar population, which might be expected to be somewhat more relaxed than the cluster system.

It is interesting, however, that under the assumption that σ_r is constant, the relatively small derived anisotropy radii require the possibly unphysical situation wherein $\beta > 0.9$ for $r > 13$ kpc. If the distribution of the cluster system indeed reflects the spatial configuration at around the time of M87's formation, then the initial collapse would have had to have been very highly radial indeed. It may be pointed out, however, that Duncan and Wheeler (1982) have found even higher anisotropies to be appropriate to the observations by Sargent et al. (1978) of the stellar component, albeit using models of

the same order of simplicity as those considered here.

If we examine now a purely isothermal case in which:

$$\sigma_3^2 = \sigma_r^2 + 2\sigma_t^2 \quad (29)$$

and σ_3 is constant with radius, then (28) may be rearranged in terms of σ_3^2 to yield:

$$\rho(r) = \rho_0 \left[\left(\frac{3r_\beta^2 + r^2}{3r_\beta^2 + r_0^2} \right) \left(\frac{r_0^2 + r_\beta^2}{r^2 + r_\beta^2} \right)^2 \right] \exp \left[- \frac{G}{\sigma_3^2} \int_0^r \frac{M(r') [3r_\beta^2 + r'^2]}{r'^2 [r_\beta^2 + r'^2]} dr' \right] \quad (30)$$

Searching once again for χ^2_{\min} for an assumed limiting magnitude of $B = 23.8$, best-fit values for the three-dimensional velocity dispersion and the anisotropy radius were found to be 1312 (1165 \rightarrow 1560) km sec⁻¹ and 6.7 (5.0 \rightarrow 8.7) kpc, respectively. For the case where $B_{\lim} = 24.4$, similar values of 1034 (950 \rightarrow 1140) km sec⁻¹ and 5.3 (4.1 \rightarrow 6.6) kpc were determined, respectively. In accordance with the large calculated anisotropy, the values for σ_3 and r_β determined here are fairly similar to those computed assuming a constant σ_r , and the goodness-of-fit is, of course, practically identical.

If the globular cluster system of M87 were formed in part by galaxy mergers or stripping of globulars during close encounters with other cluster galaxies, then one might expect to see a radially-

dependent anisotropy such that the orbits become increasingly circular at larger radii (Tonry 1983). Such a tendency was rather arbitrarily given the functional form:

$$\sigma_r^2 = \frac{\sigma_t^2}{1 + \left(\frac{r}{r_\beta}\right)^2} \quad (31)$$

in analogy to equation (26). If we assume that the globular clusters native to M87 have a uniform radial velocity dispersion and are gradually outnumbered with increasing radius by clusters acquired through stripping and possessing essentially tangential orbits, then the density function becomes:

$$\rho(r) = \rho_0 \exp\left[-\frac{G}{\sigma_r^2} \int_{r_0}^r \frac{M(r')}{r'^2} dr' + \frac{(r^2 + r_0^2)}{r_\beta^2}\right] \quad (32)$$

For an assumed limiting magnitude of 23.8, appropriate numerical integrations reveal a best fit to the data for a radial velocity dispersion of $335 \pm 3 \text{ km sec}^{-1}$ and an anisotropy radius of 50.7 ± 0.5 kpc. This fit, for which the reduced χ^2 value was found to be 1.6, is shown plotted in Figure 19. It is evident from this figure, however, that an upturn in the surface density is predicted at large radii, as opposed to the possible downturn apparent in Harris's data for $r > 16$ arcminutes (see Figure 13). A similar fit to the data for a limiting

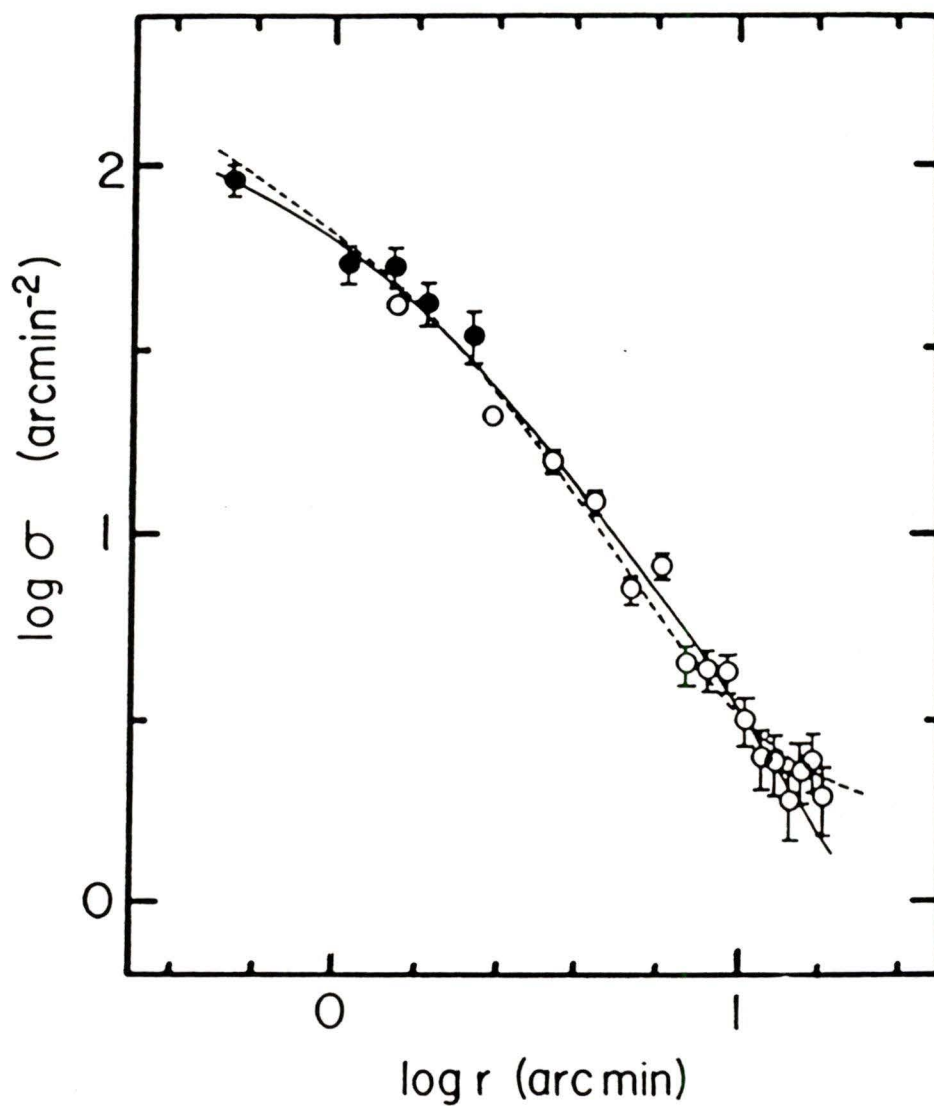


Figure 19. Surface densities predicted by models assuming a radially-variable anisotropy in the velocity dispersion. The solid curve corresponds to a radially decreasing tangential component of velocity dispersion, while the dashed curve is a fit assuming a radially increasing tangential component.

magnitude of 24.4 gives $\sigma_r = 329 \pm 3 \text{ km sec}^{-1}$ and $r_\beta = 50.2 \pm 0.5 \text{ kpc}$, for which $\chi^2_{\min} = 2.9$. The magnitudes of the uncertainties suggest a relatively deep minimum in χ^2 space, and indicate that a model with an increasing tangential velocity dispersion requires rather severe restrictions to be placed on the configuration of the globular clusters in velocity space. This in itself argues (albeit weakly) against the reality of such a model.

It is perhaps significant that for all integrations, the best-fit values of reduced χ^2_{\min} for $B_{\text{lim}} = 24.4$ were consistently found to be about twice as great as those calculated for $B_{\text{lim}} = 23.8$. It would be highly desirable, even if it required the gathering of additional observational data, to determine whether or not $B_{\text{lim}} = 23.8$ is in fact more appropriate to the sample of Harris and Smith (1976), and thus place better constraints on possible model parameters. Of course, deep CCD coverage of the radial region 2 to 20 arcminutes (and beyond) would be even more useful.

Assuming a variable anisotropy as in equation (26), the data can be fitted to the same order of agreement as above using the lower mass model suggested by Binney and Cowie. For an assumed constant σ_r and decreasing σ_t , the best-fit value of σ_r was found to occupy the region 335 to 376 km sec^{-1} and r_β was found to lie in the range 5.7 to 9.9 kpc, where these ranges were determined using values found for both $B_{\text{lim}} = 23.8$ and $B_{\text{lim}} = 24.4$. Similarly for σ_3 assumed constant, best fit values were found to be $\sigma_3 = 530$ to 630 km sec^{-1} and $r_\beta = 8$ to 14

kpc. For an assumed constant σ_r and increasing σ_t , however, no satisfactory representation of the data could be found for reasonable values of σ_3 . Consequently, if the low mass model of M87 is correct, then a radially increasing tangential component of the velocity dispersion is not indicated.

To attempt to establish the validity of either the mass model of Fabricant and Gorenstein or Binney and Cowie based on the simple models presented here would constitute at best an over-interpretation of the available data. Given the similarities in the goodness-of-fit allowed by the number of parameters for the various models and limits, very little can be said even of the dynamical state of the globular cluster system. It is reasonable to conclude, however, that rather than being the result of the depletion mechanisms discussed presently, the apparent flattening of the globular cluster surface density profile with decreasing projected radius may be a consequence of the natural core flattening of any realistic, non-singular, spherical distribution. Certainly it would be interesting to have in hand observed velocity dispersions for these globulars, since their large number and extended distribution, combined with the X-ray observations, should make possible a considerably more accurate depiction of the distribution of matter in and around M87 than we have now.

5.6 Depletion Through Dynamical Friction

An apparent levelling off of the radial distribution of globular clusters at small radii is not unique to M87, but has been found to occur in M31 (Sargent et al. 1977; Crampton et al. 1985) and NGC 4594 (Harris et al. 1984). While the results for M31 are possibly due to incompleteness (Harris and Racine 1979; Crampton et al. 1985), Harris et al. (1984) find their innermost cluster surface densities ($r \approx 3$ kpc) determined from both B and U plates to be significantly lower than any reasonable allowance for incompleteness would dictate. These authors have cited dynamical friction, tidal stripping, and disk shocking as being among the possible evolutionary depletion mechanisms responsible. Though disk shocking is likely to be inappropriate to a study of M87, dynamical friction and tidal stripping have been examined in some detail in the present analysis to see whether they might not also offer possible explanations for the distribution of M87 globulars.

The integral form of the standard equation used to describe the slow orbital deceleration due to dynamical friction has been derived by Chandrasekhar (1943):

$$\frac{dv_c}{dt} = - \frac{4\pi G^2 \rho_f m_c \ln \Lambda}{v_c^2} \left[\frac{4j^3}{\sqrt{\pi}} \int_0^{v_c} v e^{-j^2 v^2} dv \right] \quad (33)$$

where:

$$j^2 = \frac{3\sigma^2}{2\sigma_3^2} \quad (34)$$

and:

$$\Lambda = \frac{D_0 \sigma_3^2}{Gm_c} \quad (35)$$

v_c and m_c refer to the velocity and mass of the cluster under consideration while ρ_f and v refer to the space density and velocity of the field stars, respectively. m_c is assumed to be much larger than the mass of the typical field star, and the velocity distribution of the field stars has been taken to be Maxwellian. D_0 is the average distance between the field stars, though Tremaine et al. (1975) have found that the value of Λ may be approximated by r_{\max}/r_{\min} , where r_{\max} and r_{\min} are the maximum and minimum impact parameters of the system. Softened N-body calculations by Lin and Tremaine (1981) have shown that equation (33) does indeed describe the orbital decay of massive satellites with reasonable accuracy.

For the problem at hand, it was desired to calculate the length of time required for a standard-mass globular cluster's orbit of arbitrary eccentricity to decay to the point where the globular's apocentric distance dropped below 1.5 kpc, which, assuming a distance to M87 of 15 Mpc, corresponds to the 20 arcsecond inner limit of the

present observations. The values for r_{\min} and r_{\max} were taken to be 1 pc (corresponding to the core radius of a "typical" Galactic globular cluster) and the distance of the cluster from the center of M87 at any point in the orbit, respectively. In accordance with the logarithmic dependence, the results are relatively insensitive to these parameters.

Assuming that dynamical friction causes only minor changes in the energy and angular momentum of a cluster over one orbital period, one may make the simplifying assumption that these quantities are approximate integrals of the motion for each given orbit. Specifically, equation (33) was integrated around the orbit from apogalacticon to apogalacticon, at which point the energy and angular momentum were appropriately corrected and a new orbit was constructed (Tremaine et al. 1975; Surdin and Charikov 1977). The orbital paths themselves were determined using only the mass distribution of Fabricant and Gorenstein, since over the radial range considered for these calculations, the mass distribution required by the Binney and Cowie model is essentially similar. Time steps of typically 10000 years were used near apogalacticon, and were scaled through the orbit in inverse proportion to the local gravitational acceleration. The evolution of cluster orbits was calculated for a variety of initial eccentricities, defined as for closed, elliptical orbits by:

$$\epsilon = \frac{(r_{\text{ap}} - r_{\text{pe}})}{(r_{\text{ap}} + r_{\text{pe}})} \quad (36)$$

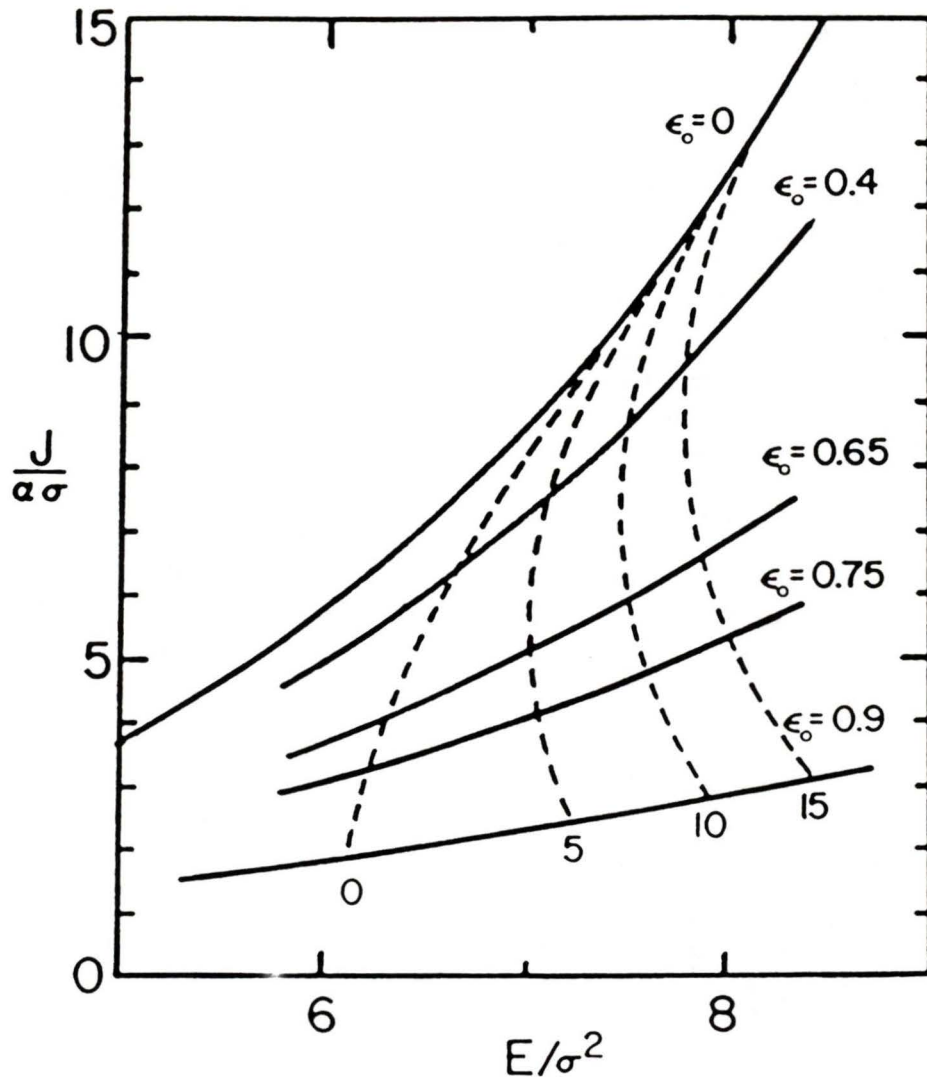


Figure 20. Lindblad diagram for the orbital evolution of a $10^6 M_{\odot}$ globular cluster for various initial orbital eccentricities. The energy and angular momentum are in units of $\sigma = 250 \text{ km sec}^{-1}$ and $\alpha = 3.2 \text{ arcseconds}$. The dashed lines indicate the time intervals (in units of 10^9 years) required for the orbits to decay to the point where the apocentric distance is 1.5 kpc.

and the results are plotted on a Lindblad diagram in Figure 20.

The solid curves in Figure 20 define the energy-angular momentum vectors calculated for a cluster of mass $10^6 M_{\odot}$, where the topmost curve corresponds to a circular orbit. The dashed curve nearest the origin defines for each orbit the point at which the apocentric distance (R_a) is 1.5 kpc, or 20 arcseconds in projection. The other dashed curves represent "isochrones", indicating for each orbit the amount of time (in units of 10^9 years) required for the energy and angular momentum to decay to the point where $R_a = 1.5$ kpc. The spacing of these curves confirms that highly eccentric cluster orbits, due to their passage through regions of higher density, decay somewhat faster than more circular orbits. It is also evident that initially noncircular orbits evolve in the direction of decreasing eccentricity, though this circularization is not as rapid for the extended orbits considered here as it is for the practically nuclear orbits examined by Tremaine et al. (1975). The times indicated for the isochrones refer to a $10^6 M_{\odot}$ cluster, though they scale in inverse proportion for any other input mass.

In Figure 21 are shown the calculated decreases in apocentric radius over the age of the universe. It is evident that only for orbits initially more eccentric than $\epsilon = 0.9$ are the populations of globular clusters likely to be significantly diminished out as far as 4 kpc from the center. This corresponds to about one arcminute in

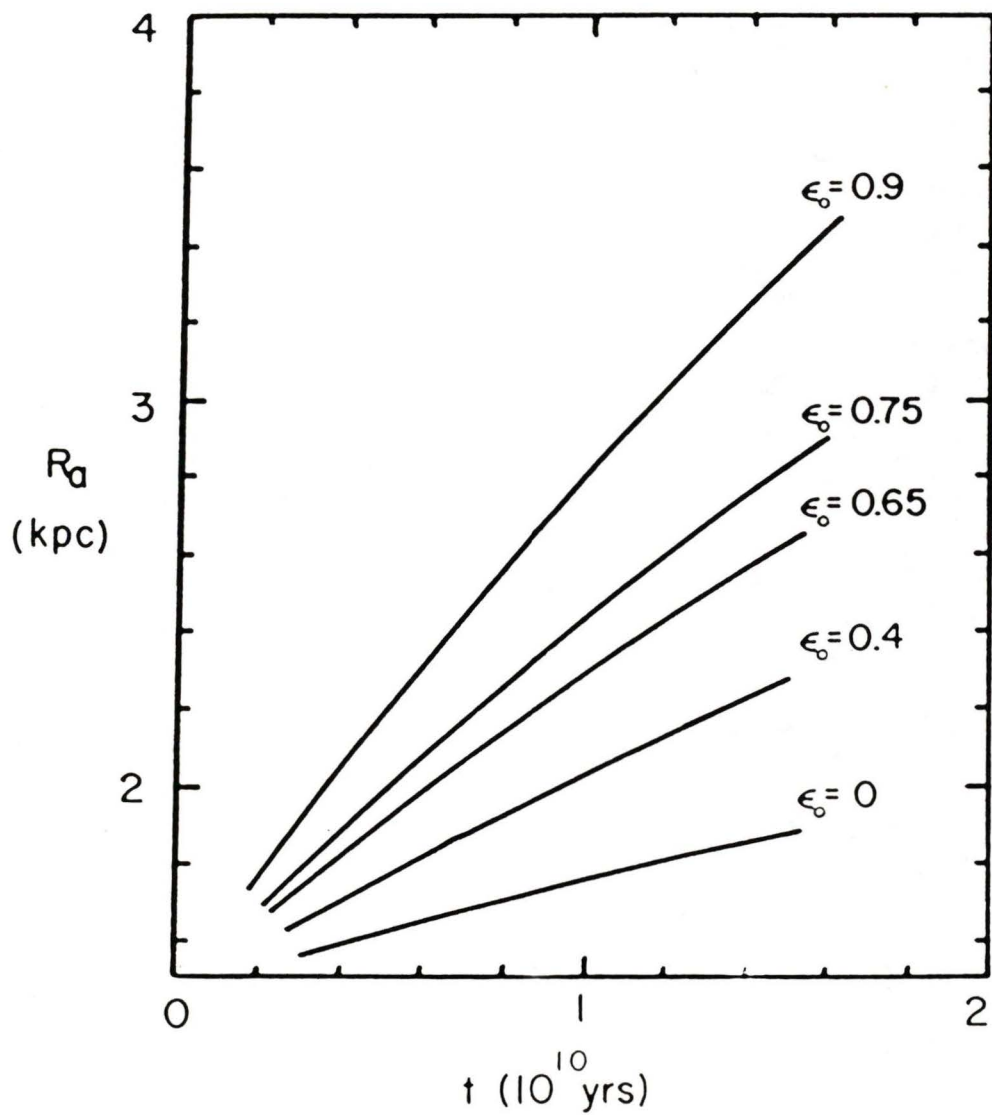


Figure 21. The evolution of apocentric distance R_a for a globular cluster of $10^6 M_\odot$. The present epoch corresponds to $t = 0$.

projection for an assumed distance of 15 Mpc and would affect only the inner two points of the present observations. Though there appears to be such a falloff in surface density for an assumed limiting magnitude of $B = 24.4$, no such effect is observed for brighter limiting magnitudes. This is contrary to expectation since the decay times for orbits of clusters of $M_V = -7.7$, which would have masses of order $10^5 M_\odot$ assuming a mean mass-luminosity ratio of 2, would be about ten times longer than those shown in Figure 21. Moreover, it has already been demonstrated that there appears to be no significant trend in luminosity functions sampled in different radial regions. Consequently, dynamical friction is unlikely to have depleted cluster populations sufficiently to produce the levelling off in the surface density profile found in this analysis.

5.7 Depletion Through Tidal Stripping

The tidal radius of a globular cluster has been given by King (1962):

$$r_t^3 = \frac{Gm}{[\omega^2 - \frac{d^2V}{dr^2}]} \quad (37)$$

where V denotes the galactic potential, m is the cluster mass, and ω is the angular velocity of the cluster at perigalacticon. If we take a radius of 2 arcminutes (8.7 kpc) corresponding to zone 5 of the present data and consider first of all circular orbits, then $\delta^2V/\delta r^2$ may be determined from the table for $M(r)$ using the density function of Fabricant and Gorenstein, since:

$$\frac{d^2V}{dr^2} = G \left[\frac{2M(r)}{r^3} - \frac{1}{r^2} \frac{dM(r)}{dr} \right] \quad (38)$$

In the region of interest, $M(r)$ is found to obey (see Figure 17):

$$M(r) = (1.6 \times 10^6) r^{1.38} \quad (39)$$

From energy considerations and the model galactic potential included in the table, the circular velocity in this region is determined to be $\sim 4.7 \times 10^{-4} \text{ pc yr}^{-1}$. For a $10^6 M_\odot$ globular cluster, equation (37) yields a corresponding tidal radius of 159 pc. This value is larger than the tidal radii found for any Galactic globulars (Harris and Racine 1979), though reducing the mass of the cluster to $10^5 M_\odot$ reduces in turn the tidal radius to 74 pc. A similar calculation carried out for the 20 arcsecond inner limit of the present data gives an expected tidal radius of about 75 pc for a $10^6 M_\odot$ cluster, and about 35 pc for a $10^5 M_\odot$ cluster. These values are generally

comparable to tidal radii determined for Galactic globulars of similar masses, and the suggestion is that as long as the orbits are assumed to be circular, cluster stripping will not be a significant depletion mechanism for the region under study.

If we consider the more extreme case of an orbit with an eccentricity of 0.9 and assume that 2 arcminutes corresponds approximately to the apocentric distance, then the cluster in question will pass within 500 pc of the galactic center. At this distance, a $10^6 M_{\odot}$ cluster would have a tidal radius of 10 pc and stripping would be correspondingly severe. Clusters of mass $10^5 M_{\odot}$ will have tidal radii of about half this value, but since such clusters often have lower central densities, they would probably be disrupted entirely. Such a mass-dependent disruption mechanism, in addition to explaining a flattening of the cluster surface density at small radii, could also be held to account for the observed shape of the luminosity function if one interprets the apparent width of the distribution as being due to a deficiency of faint globular clusters rather than an excess of bright ones.

Consequently, just as in the case of dynamical friction, highly eccentric orbits would lead to a depletion in the apparent numbers of clusters at smaller projected radii. Though models have not been calculated, it should be pointed out that if dynamical friction and cluster stripping are considered simultaneously, then orbital decay will result in an increased rate of stripping (depending on the rate

of relaxation and envelope expansion in the cluster), though the resulting loss of mass will in turn tend to slow the decay rate somewhat.

Given this dependence of the stripping and decay rate on the orbital eccentricity, it is interesting to consider the results of Chapter 4. Neither within the present data nor in a comparison with the data of Strom et al. is there conclusive evidence for a significant variation of globular cluster luminosity function with radius. One is therefore left to consider three possibilities: a) that dynamical friction and low-density cluster disruption have conspired in this region to remove roughly equal proportions of clusters from both the bright and faint ends of the luminosity function so that the overall distribution remains fairly constant with radius; b) that the lack of a characteristic feature in the luminosity function is rendering undetectable a real, radial variation in the cluster population; and c) that cluster orbits in M87 are generally not highly eccentric. Firmer constraints will probably have to await the acquisition of suitable velocity data.

5.8 Tidal Accretion and Removal of Globular Clusters

Another mechanism which could significantly affect the distribution of cluster surface densities is to be found in the

cluster-swapping scenarios described by Forte et al. (1982) and Muzzio et al. (1984). Since M87 is thought to be situated at the center of the Virgo Cluster potential well (van den Bergh 1977), a substantial number of encounters with other members of the cluster would be expected to have taken place over the age of the universe. These encounters would tend to impart energy to the less tightly bound outer globular cluster orbits and cause either transfer or outright loss of the clusters concerned.

In their original model, Muzzio et al. determined that the outer halo of a massive cD galaxy such as M87 would be enriched during galactic encounters at the expense of the intruders, giving rise to the apparent distention of the globular cluster distribution. A more recent consideration of the problem by Muzzio (1985a), however, has revealed that massive central galaxies would in fact tend to suffer overall depletion of their cluster populations. Muzzio has calculated that the central galaxy would lose some 70% of its own clusters, but gain sufficient numbers in the exchange to reduce the overall loss to some 20%. Interestingly, an additional effect of such encounters is to cause an expansion of the orbits of the indigenous globulars so that the overall density distribution would once again appear relatively extended. Furthermore, Muzzio (1985b) has calculated that a significant number of clusters would be lost in these exchanges, but would continue to orbit in the potential field of the Virgo cluster. If this field spatially coincides somewhat with that of M87, it is possible that some of the clusters observed by Harris and Smith (1976)

are not in fact bound to it.

This latter possibility is supported to some extent by the much smaller number of globular clusters apparent around M49, which is a comparably luminous elliptical situated well away from the core of the Virgo cluster. It should be pointed out, however, that observations of Harris and Petrie (1978) and Harris and van den Bergh (1981), as reanalyzed by Harris (1985), suggest that M49 suffers an almost identical distension of its cluster envelope relative to its halo profile. More convincing evidence for this collecting of "tramp" globular clusters in the potential field of a cluster of galaxies is provided by the findings of Harris et al. (1983), which suggest that NGC 3311, the central elliptical galaxy of the Hydra I cluster, has both a very flat globular cluster density profile and a specific frequency of globulars of the same order as that of M87. Dawe and Dickens (1976) have determined similar results for NGC 1399, the central galaxy of the Fornax cluster. On the other hand, Harris and Hanes (1985) have found that NGC 524, the central galaxy of the relatively poor cluster CfA 13, does not possess an overabundance of globular clusters, and van den Bergh (1984) has suggested that this apparent collection of globulars in the cluster potential is probably confined to rich clusters.

It seems evident, however, that such a mechanism would effectively dilute any radial metallicity gradient which might have been in place or developed in the globular cluster population during the formation epoch of M87. This is apparently contrary to the

findings of Strom et al. (1981), who have determined that there exists in M87 globulars a radial colour gradient which matches that of the stellar population, though it is bluer by about $U - R = 0.5$ at all radii. It is difficult to conceive of a single mechanism which would alter the spatial distribution of one population of test particles (the globular clusters) with respect to another (the halo stars) in the manner described above while generating very similar metallicity gradients².

It should be pointed out, however, that Strom et al's observations extend to only 18 arcminutes from M87, whereas the majority of accreted or lost clusters would reside at larger radii. The extension of bound orbits discussed by Muzzio (1985a) will affect the color gradients of halo stars and globular clusters equally, if differences in anisotropy are neglected. Consequently, tidal stripping and accretion may yet be held to account for some of the apparent distention of M87's cluster envelope.

²Indeed, tidal stripping and accretion should affect halo stars and globular clusters identically, though the luminosity profile will not match the density profile of the clusters if M/L is not constant.

5.9 Initial Conditions

None of the mechanisms discussed thus far can explain by themselves all the chemical and spatial characteristics apparent in the M87 globular cluster envelope and still be consistent with observations of other systems (Harris 1985). One is therefore left with the largely untestable hypothesis that the differences in distribution of halo stars and the globular clusters were established at some time during the period of formation and have remained, at least for large ellipticals like M87, relatively unaltered since that time. In particular, Harris (1985) has described a general picture in which the globular clusters formed during a relatively early stage of protogalactic collapse. The remaining gaseous material continued to collapse dissipationally through cloud-cloud collisions until the advent of general halo star formation. The observed depletion of globular clusters in the central regions might have been caused by tidal heating and collisions of the proto-globulars themselves during this stage. The resulting difference in shape and central concentration between the globular cluster system and the stellar halo population has presumably been essentially maintained until the present epoch.

This is at odds with models which suggest that the formation of globular clusters should have considerably predated the collapse of protogalaxies (Peebles and Dicke 1968; Fall and Rees 1977). This latter argument, however, encounters the problem of having to explain

both the radial metallicity gradient of globulars in galaxies and their generally observed spatial distributions. These observations, along with theoretical arguments which suggest that the characteristic mass at decoupling may have been considerably larger than the Jeans mass, have led Gunn (1980) to conclude that globular cluster formation more likely took place through dissipative processes during the early chaotic stages of protogalactic collapse. In addition, De Young et al. (1983) have determined that the early-protogalactic-collapse formation of globular clusters could have had the effect of "seeding" the still gaseous protogalactic halo with heavy elements, giving rise to the difference in color of the cluster system and halo stars observed by Strom et al. (1981). This does not explain, however, the apparent radial gradient in the metallicity of either the cluster system or the halo population. De Young et al. have suggested this might arise if the metal-rich clusters were to form later than metal-poor ones, after the protocluster gas had been substantially enriched. A suitable model for this process has not yet been developed, however.

The suggestion that globular clusters simply formed earlier than the rest of the halo is not without other problems. In particular, this does not explain observations of spiral galaxies (ie. Harris et al. 1984; van den Bergh and Harris 1982), which indicate that, while differential colour gradients still exist, the spatial distribution of globular clusters is essentially similar to that of the halo. Harris (1985) has suggested that, since only 10^6 to 10^7 years are required to

generate sufficient metals to enrich the surrounding gas if one assumes that star formation in globulars took place in an initial burst (De Young et al. 1983), the formation of globular clusters may have been delayed in spirals relative to ellipticals by on the order of the freefall time ($\sim 10^8$ years) to generate surface densities which reflect the shape of the luminosity profile. This has the advantage that it might also explain the generally greater specific frequencies found in elliptical galaxies, if one assumes that in addition to starting earlier, the formation of globulars continued for a longer period of time than in spirals. Unfortunately, one is again left with having to come up with a physically plausible mechanism which would allow for globular cluster formation which depends on time and morphology while at the same time restricting the number of free parameters. It is clear that, in addition to acquiring a larger body of observations, theoretical advances will need to be made if a greater understanding of the physical processes which led to the formation of globular clusters and galaxies is to be achieved.

CHAPTER 6

SUMMARY AND CONCLUSION

Deep CCD observations of the inner regions of M87 have been used to study the spatial and magnitude distributions of the globular cluster population. Considerable use has been made of the image-processing command language R2D2 and the automated detection and photometry package DAOPHOT. The latter was used to detect and measure objects to $B \sim 26$, though the limiting magnitude of the sample has been established by a 50% completeness criterion to occur at $B \approx 25.5$. The completeness of the sample was determined by rereducing the CCD image with a selected set of artificial "stars" randomly distributed about the frame. Background and foreground corrections were determined statistically by reducing, in an identical manner, a CCD image of a field somewhat removed from M87.

After correcting the number of detected objects for completeness and background/foreground contamination, a luminosity distribution for M87 globular clusters was produced. This distribution was compared with the luminosity functions of globular clusters in M31 and the Galaxy but, due to the small number of clusters in the local group, the results are somewhat inconclusive. This is in agreement with the

results of van den Bergh (1985), who has used more recent data compilations for local group globular clusters. On the other hand, it can be said with reasonable certainty that the luminosity function of M87 globular clusters does not follow the Gaussian form with $\sigma = 1.2$ suggested by Harris and Racine (1979) as representative of the local group. The luminosity function determined here appears to show an excess in the number of brighter globular clusters, so that a formal best fit to the data for an assumed Gaussian form gives a value of σ closer to 1.9.

If the Gaussian σ is assumed to have a value of 1.2, then a best fit to the data gives a mean magnitude of $B_0 = 24.9 \pm 0.3$. This predicts a distance to M87 of 16.5 ± 2.3 Mpc if the mean magnitude of local group luminosity functions has a value of $M_V = -7.1$ (van den Bergh 1985) and is taken to be universal. The fact that the luminosity function of globulars in M87 may be different from that in local group galaxies suggests that, at best, these distances are probably not very reliable, though they agree roughly with distances determined using more established methods.

The luminosity distribution of M87 globulars has also been considered as a function of radius. Within the region considered here, no conclusive evidence of a trend in the luminosity function with increasing radius has been found. A similar result was obtained when the luminosity function of the present sample was compared with the data of Strom et al. (1981) for larger radii. While this may be due to the lack of a characteristic feature which would lend itself to

meaningful comparison, this result, if true, suggests that evolutionary processes which would alter the cluster orbits (or the globular clusters themselves) have probably not been very effective over the radial region 1.5 to 40 kpc.

The distribution of surface density of globular clusters has also been determined from the present sample. The radial profile has been found to be significantly shallower than the profile determined by Harris and Smith (1976) or Harris (1985) at larger radii, regardless of what limiting magnitude one assumes for their sample. Whereas a power-law of the form $r^{-1.61}$ (r in arcminutes) has been fitted to the revised profile of Harris (1985), and photometry by de Vaucouleurs and Nieto (1978) gives a luminosity profile which follows the form $r^{-2.2}$, the present data suggests a profile which goes roughly as $r^{-(0.7 \pm 0.1)}$. The results of both the present study and that of Harris (1985) can be fitted by a de Vaucouleurs law with an effective radius in the range 11 to 21 arcminutes, depending on the assumed limiting magnitude of the sample of Harris and Smith (1976). Integrating the $r^{1/4}$ law out to a radial distance of one degree and assuming a Gaussian form for the luminosity function, the total number of globular clusters is found to lie in the range $12000 < N_t < 48000$. The large range given here is determined by the uncertainty in B_0 , the radial extent of the globular cluster system, and the limiting magnitude of the observations of Harris and Smith (1976). The corresponding specific frequency S determined from the best-fit values of N_t lies in the range 21 to 30.

Though the image considered here covered only a limited arc around the nucleus of M87, a study of the non-radial distribution of globular clusters revealed that the variation of surface density with position angle has an amplitude of 15% or less. This variation is considerably smaller than the variation found by Harris and Smith (1976), and is consistent with the smaller ellipticity of the halo isophotes in this region.

Some simple models have been considered in an effort to reproduce the surface density profile determined by the observations. A model in which the velocity dispersion is everywhere constant and isotropic and where the cluster population is assumed to be kinematically homogeneous was found to give a relatively poor fit to the data. Similar models in which two kinematically distinct cluster populations were postulated could be well-fitted to the data, though the number of parameters so introduced make such models highly non-unique. Similar fits to the data could be achieved by introducing a radially-variable anisotropy in the velocity dispersion, though the use of the M87 density profile suggested by Binney and Cowie (1981) does not allow, for reasonable values of the three-dimensional velocity dispersion, orbits which become more tangential with increasing radius. The data examined here did not permit useful constraints to be placed on the dynamical state of the globular cluster system. The reasonably good fits to the observations, however, are an indication that the levelling off of the surface density at small radii is likely to be real and represents the core

region of the cluster distribution.

The effects of dynamical friction and globular cluster stripping have been briefly examined, and in both cases, their influence on the cluster population considered here is significant only for orbits of relatively high eccentricities. The fact that there appears to be no strong trend of the luminosity function with radius may indicate that globular cluster orbits in the inner regions of M87 are generally not highly eccentric.

The apparent distendedness of the globular cluster distribution relative to the luminosity profile has been discussed in terms of the conditions at the time of M87's initial collapse. Though the cluster-exchange models of Muzzio (1985) can give rise to the flat surface density profile and the initial enrichment scheme of De Young et al. (1983) can produce the observed difference in colour between the halo and the cluster population, no convincing model exists which can simultaneously explain the radial colour gradient. Though M87's privileged position at the center of the Virgo cluster may account for both the enormous number of globular clusters as well as the shallow cluster surface density profile, there are known examples of cD galaxies whose globular cluster systems do not share these characteristics. It is not unreasonable, however, to suggest that an apparent excess in the number of globular clusters surrounding the central galaxy might be found only in relatively rich clusters of galaxies.

Further observational efforts should be directed at three areas

in particular. 1) It is important to determine the luminosity function of globular clusters to the faintest possible magnitudes for a much larger sample of projected radii. The extension of observations to magnitudes fainter than $B \sim 26$ and the corresponding large number of objects which would be detected should make possible much more positive comparisons of luminosity functions sampled at various radii. By itself, such a sample would allow better constraints to be placed on the effectiveness of such processes as dynamical friction and tidal stripping, while in the outer regions, a luminosity function reminiscent of the outer halos of spiral galaxies might give support to models involving tidal stripping and accretion. In view of the faintness of the objects concerned, the linearity of a CCD would be highly desirable, though the small fields currently available with such devices would make necessary the dedication of a considerable amount of large-telescope observing time.

2) It would be highly desirable to determine the radial extent of the colour gradient found by Strom et al. (1981). Though broadband photometry would make possible a much larger sample, spectrophotometry in the manner of Racine et al. (1978) would give a better indication of the spectral energy distributions and thus the actual metallicities of M87 globulars. This would require, however, the prior identification of candidates using colours and proper motions, and would be limited to fairly bright magnitudes. At the very least, broadband colours should be extended to radii of greater than twenty arcminutes to search for evidence of flattening in the colour gradient

at a level which would support a model of tidal exchange (Muzzio 1985a, b). Due to the low density of clusters at large radii, however, identification by other means might again be necessary if useful results are to be obtained.

3) It would be extremely interesting to have in hand data for the line-of-sight velocity dispersion for M87 globulars as a function of radius. Taking spectra of objects fainter than $B = 21$ at a resolution sufficient to extract usable radial velocity data is approaching the limits of what is possible with current ground-based telescopes. One would require an ideal combination of a large telescope, an efficient detector, a dark sky, good seeing, and a certain amount of good luck. Such information, however, combined with the observations suggested above, would place severe constraints on the possible dynamical state of the cluster system, and whether or not this information supports the notion that the cluster system is a dynamically separate component of the halo, an important step will have been taken in tracing the early formation stages of M87. If globular clusters are indeed primordial or nearly so, this in turn could lead to a greater understanding of the probable physical state of the universe after the decoupling of matter and radiation but before the condensation of galaxies. The not too distant commissioning of the Hubble Space Telescope should make such observations considerably less difficult and the answers to these important questions somewhat less remote.

REFERENCES

- Aaronson, M., and Mould, J. (1983). *Astrophys. J.*, **265**, 1.
- Arp, H. C., and Bertola, F. (1969). *Astrophys. Lett.*, **4**, 23.
- Arp, H. C., and Bertola, F. (1971). *Astrophys. J.*, **163**, 195.
- Avni, Y. (1976). *Astrophys. J.*, **210**, 642.
- Baum, W. A. (1955). *Publ. Astron. Soc. Pac.*, **67**, 328.
- Bevington, P. R. (1969). *Data Reduction and Error Analysis for the Physical Sciences*, (New York: McGraw-Hill), p. 111.
- Binney, J. (1981). in *The Structure and Evolution of Normal Galaxies*, ed. S. M. Fall and D. Lynden-Bell (Cambridge: Cambridge University Press), p. 55.
- Binney, J. (1982a). *Mon. Not. R. Astron. Soc.*, **200**, 951.
- Binney, J. (1982b). *Ann. Rev. Astron. Astrophys.*, **20**, 399.
- Binney, J., and Cowie, L. L. (1981). *Astrophys. J.*, **247**, 464.
- Binney, J. and Mamon, G. A. (1982). *Mon. Not. R. Astron. Soc.*, **199**, 1.
- Boroson, T. A., Thompson, I. B., and Sackett, S. A. (1983). *Astron. J.*, **88**, 1707.
- Burstein, D., and Heiles, C. (1984). *Astrophys. J. Suppl.*, **54**, 33.
- Carter, D., and Dixon, K. L. (1978). *Astron. J.*, **83**, 574.
- Chandrasekhar, S. (1943). *Astrophys. J.*, **97**, 255.
- Crampton, D., Cowley, A. P., Schade, D., and Chayer, P. (1985). *Astrophys. J.*, **288**, 494.

- Davis, L. E., Cawson, M., Davies, R. L., and Illingworth, G. (1985).
Astron. J., **90**, 169.
- Dawe, J. A., and Dickens, R. J. (1976). *Nature*, **263**, 395.
- de Vaucouleurs, G. (1978). *Astrophys. J.*, **223**, 730.
- de Vaucouleurs, G., de Vaucouleurs, A., and Corwin, H. G. (1976).
Second Reference Catalogue of Bright Galaxies,
(Austin: University of Texas Press), p. 169.
- de Vaucouleurs, G., and Nieto, J. -L. (1978). *Astrophys. J.*,
220, 449.
- de Vaucouleurs, G., and Nieto, J. -L. (1979). *Astrophys. J.*,
230, 697.
- De Young, D. S., Lind, K., and Strom, S. E. (1983). *Publ. Astron.
Soc. Pac.*, **95**, 401.
- Duncan, M. J., and Wheeler, J. C. (1980). *Astrophys. J. Lett.*,
237, L27.
- Faber, S. M., and Gallagher, J. S. (1979). *Ann. Rev. Astron.
Astrophys.*, **17**, 135.
- Fabricant, D., and Gorenstein, P. (1983). *Astrophys. J.*, **267**, 535.
- Fabricant, D., Lecar, M., and Gorenstein, P. (1980). *Astrophys. J.*,
241, 552.
- Fall, S. M., and Rees, M. J. (1977). *Mon. Not. R. Astron. Soc.*,
181, 37p.
- Forman, W., Jones, C., and Tucker, W. (1985). *Astrophys. J.*,
293, 102.
- Forte, J. C., Martinez, R. E., and Muzzio, J. C. (1982). *Astron. J.*,
87, 1465.

- Forte, J. C., Strom, S. E., and Strom, K. M. (1981). *Astrophys. J. Lett.*, **245**, L9.
- Gunn, J. E. (1980). in *Globular Clusters*, ed. D. Hanes and B. Madore (Cambridge: Cambridge University Press), p. 301.
- Hanes, D. A. (1977a). *Mon. Not. R. Astron. Soc.*, **180**, 309.
- Hanes, D. A. (1977b). *Mem. R. Astron. Soc.*, **84**, 45.
- Harris, W. E. (1985). preprint.
- Harris, W. E., and Hanes, D. A. (1985). *Astrophys. J.*, **291**, 147.
- Harris, W. E., Harris, H. C., and Harris, G. L. H. (1984). *Astron. J.*, **89**, 216.
- Harris, W. E., and Petrie, P. L. (1978). *Astrophys. J.*, **223**, 88.
- Harris, W. E., and Racine, R. (1979). *Ann. Rev. Astron. Astrophys.*, **17**, 241.
- Harris, W. E., and Smith, M. G. (1976). *Astrophys. J.*, **207**, 1036.
- Harris, W. E., and Smith, M. G. (1981). *Astron. J.*, **86**, 90.
- Harris, W. E., Smith, M. G., and Myra, E. S. (1983). *Astrophys. J.*, **272**, 456.
- Harris, W. E., and van den Bergh, S. (1981). *Astron. J.*, **86**, 1627.
- Infante, L., Pritchett, C. J., and Quintana, H. (1986). submitted to *Astron. J.*
- King, C. R., and Ellis, R. S. (1985). *Astrophys. J.*, **288**, 456.
- King, I. (1962). *Astron. J.*, **67**, 471.
- Lampton, M., Margon, B., and Bowyer, S. (1976). *Astrophys. J.*, **208**, 177.

- Landolt, A. U. (1973). *Astron. J.*, **78**, 959.
- Landolt, A. U. (1983). *Astron. J.*, **88**, 439.
- Lin, D. N. C., and Tremaine, S. (1983). *Astrophys. J.*, **264**, 364.
- Lynden-Bell, D. (1967). *Mon. Not. R. Astron. Soc.*, **136**, 101.
- Muzzio, J. C. (1985). preprint.
- Muzzio, J. C. (1985b). preprint.
- Muzzio, J. C., Martinez, R. E., and Rabolli, M. (1984). *Astrophys. J.*, **285**, 7.
- Norman, C., and Silk, J. (1979). *Astrophys. J. Lett.*, **233**, L1.
- Peebles, P. J. E., and Dicke, R. H. (1968). *Astrophys. J.*, **154**, 891.
- Pritchett, C. J., and van den Bergh, S. (1985). *Astrophys. J. Lett.*, **288**, L41.
- Racine, R. (1968). *J. R. Astron. Soc. Canada*, **62**, 367.
- Racine, R., Oke, J. B., and Searle, L. (1978). *Astrophys. J.*, **223**, 82.
- Racine, R., and Shara, M. (1979). *Astron. J.*, **84**, 1694.
- Sandage, A. R. (1961). *The Hubble Atlas of Galaxies*, Carnegie Institution, Washington.
- Sandage, A. R. (1968). *Astrophys. J. Lett.*, **152**, L149.
- Sandage, A. R., and Tammann, G. A. (1985). preprint.
- Sargent, W. L. W., Kowal, C. T., Hartwick, F. D. A., and van den Bergh, S. (1977). *Astron. J.*, **82**, 947.

- Sargent, W. L. W., Young, P. J., Boksenberg, A., Shortridge, K., Lynds, C. R., and Hartwick, F. D. A. (1978). *Astrophys. J.*, **221**, 731.
- Schild, R. E. (1983). *Publ. Astron. Soc. Pac.*, **95**, 1021.
- Stetson, P. (1985). DAOPHOT User's Manual.
- Stewart, G. C., Canizares, C. R., Fabian, A. C., and Nulsen, P. E. J. (1984). *Astrophys. J.*, **278**, 536.
- Strom, S. E., Forte, J. C., Harris, W. E., Strom, K. M., Wells, D. C., and Smith, M. G. (1981). *Astrophys. J.*, **245**, 416.
- Surdin, V. G., and Charikov, A. V. (1977). *Sov. Astron.*, **21**, 12.
- Tonry, J. L. (1983). *Astrophys. J.*, **266**, 58.
- Tremaine, S. D. (1976). *Astrophys. J.*, **203**, 345.
- Tremaine, S. D., Ostriker, J. P., and Spitzer, L. (1975). *Astrophys. J.*, **196**, 407.
- Tyson, J. A., and Jarvis, J. F. (1979). *Astrophys. J. Lett.*, **230**, L153.
- van Albada, T. S. (1982). *Mon. Not. R. Astron. Soc.*, **201**, 939.
- van den Bergh, S. (1977). *Vistas in Astronomy*, **21**, 71.
- van den Bergh, S. (1981). *J. R. Astron. Soc. Canada*, **75**, 169.
- van den Bergh, S. (1983). in *Clusters and Groups of Galaxies*, ed. F. Mardirossian, G. Giuricin, and M. Mezzetti (Dordrecht: Reidel Publishing Company), p. 139.
- van den Bergh, S. (1984). submitted to *Astrophys. and Space Science*.
- van den Bergh, S. (1985). *Astrophys. J.*, in press.
- van den Bergh, S., and Harris, W. E. (1982). *Astron. J.*, **87**, 494.

- van den Bergh, S., Pritchett, C. J., and Grillmair, C. G. (1985).
Astron. J., **90**, 595, (Paper I).
- Young, P.J. (1976). *Astron. J.*, **81**, 807.
- Young, P. J., Westphal, J. A., Kristian, J., Wilson, P., and Landauer,
F. P. (1978). *Astrophys. J.*, **221**, 721.
- Webbink R. F. (1985). *I.A.U. Symp. No. 113, Dynamics of Star
Clusters*, ed. J. Goodman and P. Hut, (Dordrecht: Reidel).
- Zwicky, F. (1957). *Morphological Astronomy*, (Berlin: Springer-
Verlag), p. 138.

VITA

Surname: GRILLMAIR Given Names: CARL JOHANN

Place of Birth: Edmonton, Alta. Date of Birth: Feb. 12, 1959

Educational Institutions Attended, with Dates of Entering and Leaving:

University of Calgary, Calgary, Alta. 1979 to 1983

University of Victoria, Victoria, B.C. 1983 to 1985

Degrees, Diplomas, Etc., Awarded, with Dates and Names of Institutions:

B.Sc. (Honours) 1983 University of Calgary, Calgary

Honours and Awards:

Cecil M. Brownlee Bursary, 1979

University of Calgary Merit Award, 1980

Province of Alberta Award, 1980 and 1981

BP Canada Scholarship, 1981

Top Student in (1st, 2nd, 3rd) Year Physics Award, 1981, 1982, 1983

N.S.E.R.C. Summer Undergraduate Research Award, 1981, 1982, and 1983

Publications:

Pritchett, C. J., and Grillmair, C. J. (1984). *Pub. Astron. Soc. Pac.*,

96, 349.

Van den Bergh, S., Pritchett, C. J., and Grillmair, C. J. (1985).

Astron. J., 90, 595.

PARTIAL COPYRIGHT LICENSE

I hereby grant the right to lend my thesis or dissertation (the title of which is shown below) to users of the University of Victoria Library, and to make single copies only for such users or in response to a request from the Library of any other university, or similar institution, on its behalf or for one of its users. I further agree that permission for extensive copying of this thesis for scholarly purposes may be granted by me or a member of the University designated by me. It is understood that copying or publication of this thesis for financial gain shall not be allowed without my written permission.

Title of Thesis/Dissertation

THE DISTRIBUTION OF GLOBULAR CLUSTERS IN M87

Author



CARL J. GRILLMAIR

Sept 20, 1985